Cellular inorganic carbon fluxes in the coccolithophore *Emiliania huxleyi* and its relevance for marine carbon cycling

Dissertation

zur Erlangung des akademischen Grades eines

Doktors der Naturwissenschaften

– Dr. rer. nat. –

am Fachbereich 2 (Biologie/Chemie)

der Universität Bremen

vorgelegt von

Kai Schulz

Bremen, November 2005

Contents

1 GENERAL INTRODUCTION

1.1 Phytoplankton and the marine carbon cycle

The global carbon cycle is characterised by different reservoirs between which carbon is exchanged. These reservoirs differ in size and residence time for carbon, and in the form in which carbon is present (Siegenthaler and Sarmiento, 1993). Most of the carbon on Earth, about 60 million Pg C (1Pg equals 10^9 tons) is stored in sediments and the lithosphere. The ocean represents the second largest reservoir with about 39000 Pg C of dissolved inorganic carbon (DIC), 700 Pg C of dissolved organic carbon (DOC) and about 3 Pg C of particulate organic carbon (POC) such as marine phytoplankton. In comparison, the terrestrial biomass is more then 200 times larger than that of the marine biosphere. However, approximately 40% of global primary production occurs in the ocean (Falkowski and Raven, 1997). This seeming contradiction rests on comparatively higher turnover rates of biogenic material in the ocean (on the order of days) compared to that on land (on the order of years). The atmosphere presently contains about 750 Pg C of carbon, mainly in the form of the greenhouse gas carbon dioxide (CO_2). This amount translates to a carbon dioxide partial pressure (pCO_2) of about 380 μatm. The amount of CO_2 in the atmosphere is steadily increasing, at a current rate of about 3.3 Pg C per year, due to human activities such as the combustion of fossil fuels (the recoverable reservoir (oil and coal) is estimated at about 4000 Pg C (Sundquist, 1993), more than five times larger than that of the atmosphere), deforestation and changes in land use (IPCC 2001). Actual carbon emissions into the atmosphere, however, are about 8 Pg C per year (IPCC 2001), mainly as CO_2. Rates of CO_2 increase in the atmosphere are smaller than emission rates as some of the CO_2 is taken up by the ocean and the terrestrial biosphere. In that respect, the enormous importance of the ocean is emphasised by the fact that, starting with the industrial revolution, it has taken up about 50% of the CO_2 emitted by mankind's combustion of fossil fuels (Sabine et al., 2004).

Uptake of atmospheric CO_2 into the ocean is mediated by two so-called carbon pumps which lead to a depletion of DIC in the surface relative to the deep ocean, termed the

physical and the biological carbon pumps (Volk and Hoffert, 1985). The physical pump describes the vertical flux of CO_2 into the ocean's interior resulting from differences in CO_2 solubility of warm and cold water. As warm surface waters generally flow from low to high latitudes, subsequent cooling leads to increased solubility for atmospheric CO_2. At high latitudes of the Arctic and Antarctic, the regions of deep-water formation, these cold and hence DIC rich surface waters sink to depth. The biological carbon pump comprises two types, the organic carbon and the carbonate pump (Fig. 1).

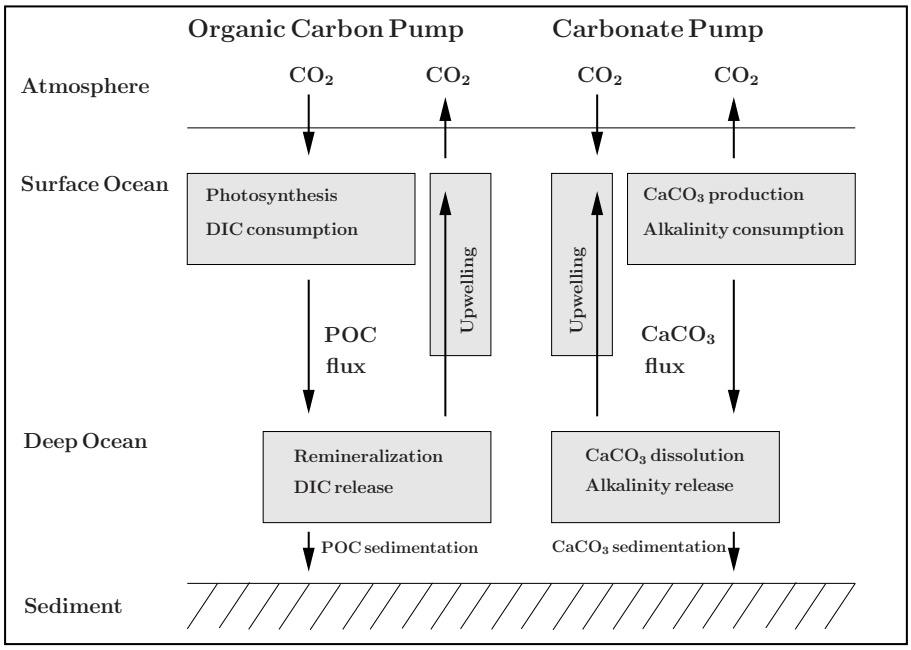

Figure 1: Schematic diagram of the two types of the biological carbon pump, the organic carbon pump and the carbonate pump

The organic carbon pump is driven by photosynthetic fixation of DIC by marine phytoplankton leading to enhanced atmospheric CO_2 uptake in the surface ocean. Subsequent sinking of the produced particulate organic matter (POC) transports carbon to depth where most is remineralised to DIC (only about 0.1% is stored in sediments). The carbonate pump is driven by the transport of biogenic calcium carbonate ($CaCO_3$), mainly produced by calcifying plankton such as coccolithophores, foraminifera and pteropods. During the

formation of $CaCO_3$ the seawater carbonate system shifts towards higher [CO_2] as more alkalinity than DIC is consumed (CO_3^{2-} ions equal one unit of DIC and two units of alkalinity). As $CaCO_3$ formation reduces the ocean's storage capacity for atmospheric CO_2, opposite to photosynthetic carbon fixation, the carbonate pump is often referred to as the carbonate counter pump. In the surface ocean $CaCO_3$ is presently a stable compound, but with depth its solubility increases. Hence, sinking $CaCO_3$ will start to dissolve as deep waters become undersaturated with respect to $CaCO_3$. The depth horizon below which $CaCO_3$ starts to dissolve in sediments is called the lysocline, and lies around 4.5 km in the western Atlantic Ocean, around 3.5 km in the western Indian Ocean and above 3 km in the North Pacific (Broecker and Peng, 1982). In the present ocean the strength of the organic carbon pump exceeds that of the $CaCO_3$ pump by about a factor of 10 (Yamanaka and Tajika, 1996; Harvey, 2001)

The turnover time of the ocean is about 1000 years. On this time scale the cold, DIC and alkalinity rich deep waters are brought back to the ocean's surface, mainly in tropical areas. Subsequent warming decreases the solubility for CO_2 and, depending on the DIC to alkalinity ratio and the biological activity, the ocean in these regions can act as a CO_2 source for the atmosphere.

While the magnitude of global temperature increase upon the projected doubling of current atmospheric CO_2 around the year 2100 (Houghton et al., 1995) is still under debate, the change in future ocean chemistry is highly predictable. Continued oceanic uptake of atmospheric CO_2 by the physical carbon pump will give rise to a 60% increase in hydrogen ion concentration in the surface ocean (Sabine et al., 2004), corresponding to a drop in pH of about 0.2 units in comparison to today. The effects of ocean acidification on the marine biota, especially on the strength of both biological carbon pumps, however, are unknown. The projected magnitude and rate of the changes in atmospheric CO_2 and hence in marine carbon cycling are unprecedented, at least for the last hundred of thousands years and possibly for the past 20 millions of years (IPCC 2001).

1.2 Coccolithophores and the marine carbon cycle

While the marine organic carbon pump is mainly driven by the silicifying group of diatoms a significant fraction of the marine carbonate pump is mediated by coccolithophores (Milliman, 1993). In the present ocean about 250 living species of coccolithophores have been described (Winter and Siesser, 1994) which evolutionary roots date back to the Triassic (about 230 Ma BP). These unicellular planktonic algae are generally covered with minute $\mathrm{CaCO_3}$ structures, the so-called coccoliths. With respect to their morphology they are divided into two general groups, the heterococcoliths and the holococcoliths. Our present knowledge of coccolith formation rests upon only a few well-studied species (e.g. *Emiliania huxleyi* and *Coccolithus pelagicus*). In these the complex heterococcolith $\mathrm{CaCO_3}$ structures are produced in intracellular vesicles, the coccolith production vesicle (CPV), and then transported to the cell's outer surface (Manton and Leedale, 1969; Westbroek et al., 1989). While there is evidence that the more simple $\mathrm{CaCO_3}$ holococcolith structures are precipitated externally at the cell's surface (Rowson et al., 1986), it is not clear whether they might also be produced in CPVs (Brownlee and Taylor, 2004).

Although the chemical and isotopic composition of the solution in CPVs from which $\mathrm{CaCO_3}$ is precipitated is clearly under tight cellular control, coccoliths have been found to record characteristics of ambient seawater. Hence, changes in the chemical and isotopic composition of calcareous coccolithophorid shells found in marine sediments have been proposed as an indicator for past climate conditions (for a review see Stoll and Ziveri (2004)).

1.3 Past changes in the marine carbon cycle

Atmospheric $\mathrm{CO_2}$ is known to have oscillated between 180 and 280 ppmv (parts per million per volume) during the last 400 kyr (1 kyr equals 1000 years), where 280 ppmv coincide with warm interglacial climate and low $\mathrm{pCO_2}$ values correspond to cold glacial climate conditions (Fig. 2). Another important feature of these climatic oscillations are the compa-

ratively abrupt transitions from glacial to interglacial conditions, the so-called terminations (Broecker and Van Donk, 1970; Broecker, 1984).

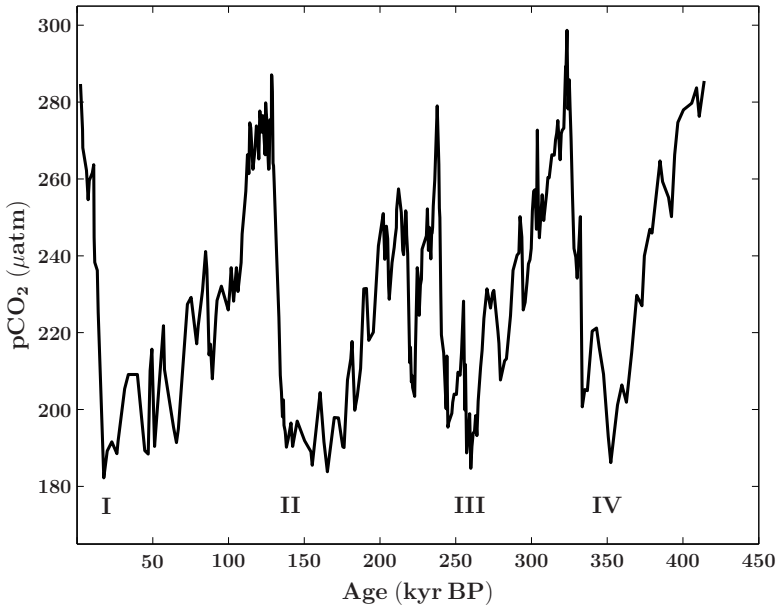

Figure 2: Changes in partial pressure of CO_2 in entrapped air of the Vostok ice core with time (GT4 timescale, gas age) (Petit et al., 1999). Roman numbers indicate the first four glacial terminations of the Late Pleistocene.

Glacial/interglacial cycles are associated with the build-up and melting of enormous Northern Hemisphere (NH) ice sheets with concomitant changes in sea-level. For instance, the sea-level at the last glacial maximum (LGM) around 20.000 years BP was about 120 meters lower than today. At first approximation, the oxygen isotopic composition ($\delta^{18}O$) in the calcareous shells of benthic foraminifera is a proxy for sea-level and hence global ice sheet extension (Shackelton, 2000). As ice on land is heavily depleted in ^{18}O compared to seawater, the ocean becomes enriched in ^{18}O in glacial times resulting in higher $\delta^{18}O$ values (compare Fig. 3). Therefore, Earth's climatic history can be extended beyond the reach of ice core data by sedimentary records of $\delta^{18}O$.

The Pleistocene, the last two million years, is characterised by regular oscillations in global ice volume. In the Late Pleistocene these fluctuations are less frequent but with

higher amplitude in comparison to the Early Pleistocene. The so-called Mid Pleistocene Revolution (MPR) marks this shift in frequency and amplitude.

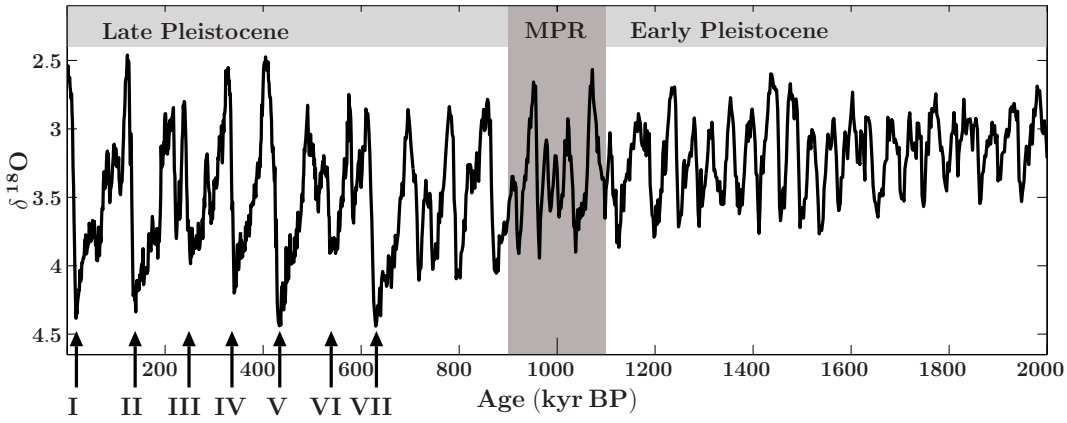

Figure 3: Comparison of climate variability in the Late Pleistocene (100 kyr world) and the Early Pleistocene (41 kyr world) with $\delta^{18}\mathrm{O}$ as an indicator for global ice volume of the LR04 benthic stack (Lisiecki and Raymo, 2005) against time. The Mid Pleistocene Revolution (MPR) marks the shift from the 41 kyr to the 100 kyr world. Roman numbers denote the seven glacial terminations of the Late Pleistocene.

The reduction in atmospheric $\mathrm{CO_2}$ by about 100 ppmv in glacial times translates to approximately 200 Pg C of carbon which must have been transfered to other reservoirs. On the time scales of glacial/interglacial change only the ocean or the terrestrial biosphere are possible candidates. The terrestrial biosphere, however, is likely to have been rather a carbon source in glacial climate as the enormous NH ice sheets covered Scandinavia, Canada and northern Russia, areas covered by large forests in interglacial times. This is supported by reduced glacial $\delta^{13}\mathrm{C}$ values in $\mathrm{CaCO_3}$ of a benthic foraminifera, indicating that the carbon reservoir of the terrestrial biosphere was reduced in glacial times (Shackleton, 1997).

Several mechanisms have been proposed to transfer carbon from the atmosphere into the ocean in glacial periods (for a review see Archer et al. (2000)). Stimulation of the organic carbon pump can significantly reduce atmospheric $\mathrm{CO_2}$. This enhancement could rest on an increase in the ocean's macronutrient (nitrate and phosphate) inventory or a change in the carbon to nutrient ratio (Redfield ratio) in marine phytoplankton (Broecker and Peng,

1982; McElroy, 1983; Broecker and Henderson, 1998). Enhanced dust and hence trace metal input into the so-called 'high nitrate low chlorophyll' areas, in which primary production is presently limited by the availability of iron, in glacial times constitutes another possible stimulation of the marine organic carbon pump (Martin, 1990). This could also have stimulated nitrogen fixation and increased the ocean's inventory of nitrate (Falkowski, 1997; Mills et al., 2004). A second scenario increasing the ocean's storage capacity for atmospheric CO_2 in glacial times is a reduction in the intensity of the $CaCO_3$ pump (Keir, 1988; Archer and Maier-Reimer, 1994; Sigman et al., 1998) which increases the pH of the ocean. Finally, a reduction of deep water ventilation was proposed which could explain glacial variations in atmospheric pCO_2 without significant changes in the strength of the biological carbon pump (Toggweiler, 1999).

However, all of these mechanisms, able to account for the re-partitioning of carbon between atmosphere and ocean during glacial/interglacial climate shifts, are lacking a trigger which sets them in motion. Milutin Milankovitch (1941) was the first to propose that the size of the NH ice sheets is determined by accumulation in the winter and melting in the summer season. Hence, he correlated glacial/interglacial cycles to variations in NH summer insolation which is driven by three orbital parameters, eccentricity (the shape of Earth's orbit around the sun), obliquity (the tilt of Earth's axis of rotation) and precession (the movement of Earth's rotational axis and its orbit around a full circle). Although it is now widely accepted that changes in orbital forcing are responsible for glacial/interglacial cycles, a mechanistic understanding is still missing.

1.4 Trace metals and the marine carbon cycle

One of the mechanisms proposed to change the partitioning of CO_2 between atmosphere and ocean on glacial/interglacial time scales are variations in dust and hence trace metal supply to the surface ocean (Martin, 1990; Morel et al., 1994). This rests on the coupling of biogeochemical cycling of carbon and trace metals, such as iron and zinc, which are es-

sential plant nutrients limiting phytoplankton growth in parts of today's ocean (for a review see Morel and Price (2003)). Iron is an integral part in photosystems I and II and required for photosynthetic electron transport (Greene et al., 1991, 1992). And zinc is an important co-factor in many enzymes, such as carbonic anhydrase, which are needed for synthesis and degradation of various metabolites. Furthermore, zinc stabilises proteins and nucleic acids, and is required for gene expression via the so-called 'zinc-finger' motive of the RNA polymerase (Vallee and Auld, 1990).

In the present ocean, iron is limiting primary production in the so-called high nitrate low chlorophyll (HNLC) areas, comprising the Southern Ocean, the equatorial Pacific and parts of the North Pacific (for a review see de Baar and Boyd (2000)). Outside these regions, export production is mainly limited by macronutrients such as nitrogen (Conkright et al., 1994). But also zinc has been found to limit phytoplankton growth in the North Pacific (Lohan et al., 2002; Crawford et al., 2003). Furthermore, total zinc concentrations in the central Pacific (Bruland, 1989) and North Atlantic (Kremling and Streu, 2001) have been measured as low as those in the North Pacific. Zinc limitation of phytoplankton could therefore be a more general phenomenon in parts of today's ocean.

1.5 Seawater carbonate system

The chemical basis of the marine carbon cycle is the carbonate system. Inorganic carbon in aqueous solutions is predominantly present in three forms, aqueous carbon dioxide (CO_2(aq)), bicarbonate (HCO_3^-), and carbonate ions (CO_3^{2-}). The concentration of the fourth compound, true carbonic acid (H_2CO_3), is much smaller than that of CO_2(aq). Hence, the sum of CO_2(aq) and H_2CO_3 is generally denoted by CO_2. In equilibrium with gaseous carbon dioxide (CO_2(g)) the concentration of CO_2 in seawater is given by Henry's law as

$$[CO_2] = K_0 \, fCO_2 \tag{1}$$

where K_0 is the solubility coefficient and fCO_2 denotes the fugacity of CO_2. Please note that fugacity rather than partial pressure is used as CO_2 is not an ideal gas. The difference between the partial pressure of CO_2 (pCO_2) and fugacity, however, is only a few permil. Dissolved CO_2 reacts with water forming HCO_3^- and CO_3^{2-}. The equilibria between CO_2, HCO_3^-, and CO_3^{2-} are then given by

$$CO_2 + H_2O \underset{}{\overset{K_1}{\rightleftharpoons}} HCO_3^- + H^+ \overset{K_2}{\rightleftharpoons} CO_3^{2-} + H^+ \tag{2}$$

with K_1 and K_2 being the first and second equilibrium constants, respectively. Please note that equilibria and not reaction pathways are considered as CO_2 converts to HCO_3^- not only by hydration, which includes the reaction pathway via H_2CO_3, but also by hydroxylation (for details see Zeebe and Wolf-Gladrow (2001), pp.95-98). The concentrations of the three carbonate species can be calculated introducing stoichiometric equilibrium constants, K_1^* and K_2^* as

$$K_1^* = \frac{[HCO_3^-][H^+]}{[CO_2]} \tag{3}$$

and

$$K_2^* = \frac{[CO_3^{2-}][H^+]}{[HCO_3^-]} \tag{4}$$

Stoichiometric equilibrium constants depend on temperature, salinity and pressure and have been determined in several studies (for a comparison see Lee et al. (2000)). The sum of these three dissolved carbonate species is referred to as total dissolved inorganic carbon (DIC).

$$DIC = [CO_2] + [HCO_3^-] + [CO_3^-] \tag{5}$$

The proportion of the three carbonate species relative to DIC is a function of pH (compare Eq. 2) where in acidic environments the equilibrium is shifted towards CO_2, in contrast to alkaline environments where it is more on the side of CO_3^{2-} (Fig. 4). At a typical seawater pH around 8.0 HCO_3^- is the dominant inorganic carbon specimen.

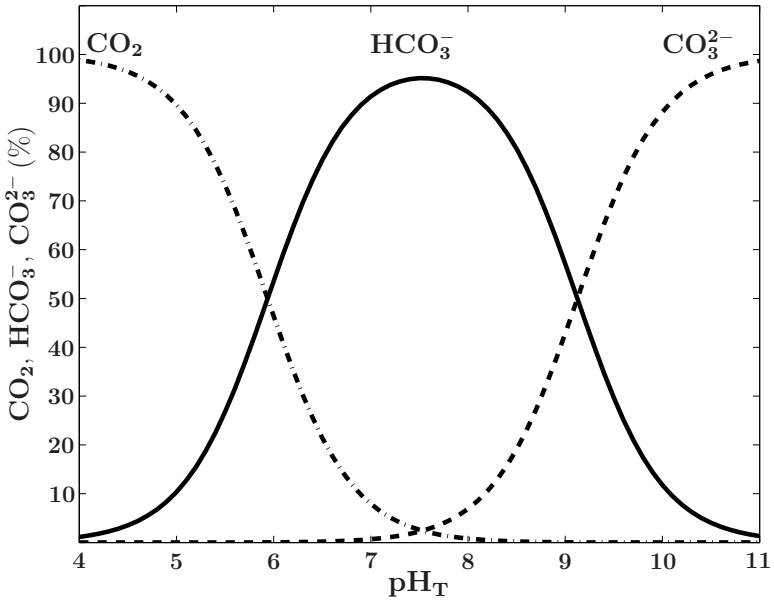

Figure 4: Relative proportion of the three carbonate species $\mathrm{CO_2}$ $\mathrm{HCO_3^-}$ and $\mathrm{CO_3^{2-}}$ in seawater (at a salinity of 35 and a temperature of $15°\mathrm{C}$) to the total inorganic carbon concentration as a function of pH. Please note that $\mathrm{pH_T}$ denotes the pH on the total scale (Hansson, 1973).

The description of the carbonate system would be incomplete without the concept of total alkalinity, TA. The most accurate definition is given by Dickson (DOE (1994)) as "The total alkalinity of a natural water is thus defined as the number of moles of hydrogen ion equivalent to the excess of proton acceptors (bases formed from weak acids with a dissociation constant $\mathrm{K} \leq 10^{-4.5}$ at $25°\mathrm{C}$ and zero ionic strength) over proton donors (acids with $\mathrm{K} \geq 10^{-4.5}$) in one kilogram of sample." Hence, for seawater the definition for total alkalinity reads

$$\begin{aligned} \mathrm{TA} &= [\mathrm{HCO_3^-}] + 2[\mathrm{CO_3^{2-}}] + [\mathrm{B(OH)_4^-}] + [\mathrm{OH^-}] + [\mathrm{HPO_4^{2-}}] + 2[\mathrm{PO_4^{3-}}] \\ &\quad + [\mathrm{H_3SiO_4^-}] + [\mathrm{NH_3^-}] + [\mathrm{HS^-}] - [\mathrm{H^+}]_\mathrm{F} - [\mathrm{HSO_4^-}] - [\mathrm{HF}] - [\mathrm{H_3PO_4}] \end{aligned} \quad (6)$$

with $[H^+]_F$ referring to the free concentration of hydrogen ion. Note that in seawater systems pH, the negative common logarithm of the hydrogen ion concentration, is generally defined on the total scale. The relation between total and free scale is given by $[H^+]_T = [H^+]_F + [HSO_4^-]$. From DIC and TA the concentrations of CO_2, HCO_3^- and CO_3^{2-}, and the pH can be calculated applying the stoichiometric equilibrium constants. However, as the six parameters of the carbonate system (CO_2, HCO_3^-, CO_3^{2-}, DIC, TA and pH) are interdependent, any combination of two of them is equally suitable for calculation of the remaining four (for details see Zeebe and Wolf-Gladrow (2001)).

Processes such as photosynthetic carbon fixation and $CaCO_3$ formation impact the carbonate system by changing TA and DIC. The reasoning is as follows. To a first approximation TA can be considered to equal the carbonate alkalinity CA

$$TA \simeq CA = [HCO_3^-] + 2[CO_3^{2-}] \tag{7}$$

Furthermore, as in natural seawater $[CO_2]$ is much smaller than $[HCO_3^-]$ and $[CO_3^{2-}]$ DIC can be approximated as

$$DIC \simeq [HCO_3^-] + [CO_3^{2-}] \tag{8}$$

The combination of these two equations shows that $[CO_3^{2-}]$ is roughly given as the difference between TA and DIC. Increasing the difference leads to increased $[CO_3^{2-}]$ compared to $[CO_2]$ and a higher pH whereas decreasing the difference yields lower pH (compare Fig. 4). Hence, as photosynthetic carbon fixation reduces DIC but hardly affects TA, the difference between TA and DIC increases leading to higher pH and decreased $[CO_2]$. This is opposite to the process of $CaCO_3$ formation which decreases DIC and TA in a 1 to 2 ratio. Thus, the difference between TA and DIC decreases and pH is reduced while $[CO_2]$ increases.

The carbonate system is not only characterised by equilibria but also by kinetics. While in chemical equilibrium the concentrations of the reactants are, by definition, constant with time, chemical kinetics describe the process of changing concentrations in the course of a

reaction. The inter-conversion reaction between HCO_3^- and CO_3^{2-}, for example, comprises two reaction pathways, the hydrolysis and protolysis of HCO_3^-, which are characterised by a so-called forward and backwards reaction.

$$HCO_3^- + OH^- \underset{k_{-5}^{OH^-}}{\overset{k_{+5}^{OH^-}}{\rightleftharpoons}} CO_3^{2-} + H_2O \tag{9}$$

$$CO_3^{2-} + H^+ \underset{k_{-5}^{H^+}}{\overset{k_{+5}^{H^+}}{\rightleftharpoons}} HCO_3^- \tag{10}$$

with $k_{+5}^{OH^-}$ and $k_{-5}^{OH^-}$ being the rate constants for the hydrolysis, and $k_{+5}^{H^+}$ and $k_{-5}^{H^+}$ those for the protrolysis reaction. Rate constants depend on temperature and salinity. However, the actual rate at which a reaction occurs also depends on the concentration of the reactants. The relation between equilibrium and kinetics in this HCO_3^- / CO_3^{2-} system is then given by

$$K_2^* = \frac{[CO_3^{2-}][H^+]}{[HCO_3^-]} = \frac{k_{+5}^{OH^-}}{k_{-5}^{OH^-}} K_W^* = \frac{k_{-5}^{H^+}}{k_{+5}^{H^+}} \tag{11}$$

with K_W^* being the equilibrium constant for the ion product of water. Even at chemical equilibrium the forward and backward reactions proceed, however the rate of both reactions is equal and hence, there is no change in the concentrations of the reactants. In this sense, chemical equilibrium can be regarded a special case of chemical kinetics in which the system reached the steady-state. The inter-conversion rate between HCO_3^- and CO_3^{2-} is orders of magnitude faster than that between CO_2 and HCO_3^- which is on the order of seconds.

1.6 Carbon isotope fractionation

Isotopes of an element have the same number of protons but a different number of neutrons. Carbon has two stable isotopes, $^{12}\mathrm{C}$ and $^{13}\mathrm{C}$ with natural abundances of about 99% and 1%, respectively. The ratio of atoms of $^{13}\mathrm{C}$ to $^{12}\mathrm{C}$ in a certain compound, for example organic matter ($\mathrm{C_{org}}$), is denoted by R.

$$^{13}\mathrm{R_{org}} = \frac{^{13}\mathrm{C_{org}}}{^{12}\mathrm{C_{org}}} \tag{12}$$

If two compounds in a reaction system exhibit different isotope ratios a fractionation factor α can be defined. For instance, the main carboxylating enzyme of marine phytoplankton, RubisCO (Ribulose-1,5-bisphosphate carboxylase/oxygenase), fixes $^{12}\mathrm{CO_2}$ at a higher rate than $^{13}\mathrm{CO_2}$. Hence, the isotopic composition of the organic matter produced during photosynthetic carbon fixation is isotopically lighter than the substrate $\mathrm{CO_2}$. The corresponding fractionation factor is given as

$$\alpha_{\mathrm{Rub}} = \frac{^{13}\mathrm{R_{C_{fixed}}}}{^{13}\mathrm{R_{CO_2}}} \tag{13}$$

were $^{13}\mathrm{R_{C_{fixed}}}$ denotes the isotopic ratio of the carbon fixed by RubisCO. As fractionation factors are generally very close to 1, for RubisCO it is about 1.029 (Roeske and O'Leary, 1984), isotopic fractionation is commonly expressed by ϵ in permil.

$$\epsilon_{\mathrm{Rub}} = (\alpha_{\mathrm{Rub}} - 1) \times 10^3 \tag{14}$$

The isotopic composition of a sample such as organic matter is determined by means of mass spectrometry with respect to a standard and expressed by the delta notation.

$$\delta^{13}\mathrm{C_{org}} = \left(\frac{^{13}\mathrm{C_{org}}}{^{13}\mathrm{C_{standard}}} - 1 \right) \times 10^3 \tag{15}$$

For many years the standard used for carbon isotope analyses was generally PDB (Pee-Dee Belemnite), a limestone of the Cretaceous Pee-Dee formation in South Carolina. As PDB is no longer available a new standard as been defined, V-PDB (Vienna-PDB). It follows that

the fractionation factor associated with photosynthetic carbon fixation (ϵ_{p}), which is given relative to RubisCO's substrate $\mathrm{CO_2}$, is defined as

$$\alpha_{\mathrm{p}} = \frac{\delta^{13}\mathrm{C}_{\mathrm{CO_2}} + 10^3}{\delta^{13}\mathrm{C}_{\mathrm{org}} + 10^3} \tag{16}$$

Hence, fractionation in per mil is given as

$$\epsilon_{\mathrm{p}} = \frac{\delta^{13}\mathrm{C}_{\mathrm{CO_2}} - \delta^{13}\mathrm{C}_{\mathrm{org}}}{1 + \delta^{13}\mathrm{C}_{\mathrm{org}}/10^3} \tag{17}$$

Stable carbon isotope fractionation by marine phytoplankton varies over a wide range depending on environmental conditions and physiological characteristics of algal species. Although RubisCO is known to fractionate with about $29‰$ against $^{13}\mathrm{CO_2}$, values for ϵ_{p} are generally lower. There are several models able to account for this observation (Farquhar et al., 1982; Rau et al., 1996). Most easily, however, this is understood considering a simple cell model comprising one compartment in which fractionation is given by the inorganic carbon fluxes into and out of the cell (Sharkey and Berry, 1985) as

$$\epsilon_{\mathrm{p}} = \mathrm{a}\epsilon_{\mathrm{db}} + \epsilon_{\mathrm{Rub}}\frac{\mathrm{CO_2eff}}{\mathrm{DICup}} \tag{18}$$

where ϵ_{Rub} denotes the kinetic fractionation of RubisCO, DICup the amount of inorganic carbon taken up and $\mathrm{CO_2}$eff the amount of $\mathrm{CO_2}$ leaking out of the cell. The factor a and ϵ_{db}, introduced by Burkhardt et al. (1999), describe the contribution of $\mathrm{CO_2}$ to the total DIC uptake and the equilibrium fractionation between the two carbonate species $\mathrm{CO_2}$ and $\mathrm{HCO_3^-}$, which is temperature and salinity dependent and on the order of $10‰$ (Mook, 1986). For a graphical representation of Eq. 18 see Fig. 5. It is obvious that ϵ_{p} is proportional to the ratio of $\mathrm{CO_2}$ efflux to DIC uptake, the so-called leakage. If there is no change in the relative contribution of $\mathrm{CO_2}$ and $\mathrm{HCO_3^-}$ to total DIC uptake, ϵ_{p} will increase with increasing leakage. Assuming that $\mathrm{CO_2}$ is the only inorganic carbon source taken up, in which case the factor a equals zero, ϵ_{p} reaches the characteristic value for the fractionation by RubisCO ($29‰$) only if the magnitude of the $\mathrm{CO_2}$ efflux approaches that of the DIC uptake. However, this would mean that inorganic carbon uptake would be quite inefficient

as all the carbon taken up is lost before being fixed. Additionally, most phytoplankton species take up inorganic carbon by active transport, investing considerable amounts of energy. Thus, theoretical maximum fractionation of $29‰$ is unlikely to be encountered in phytoplankton species.

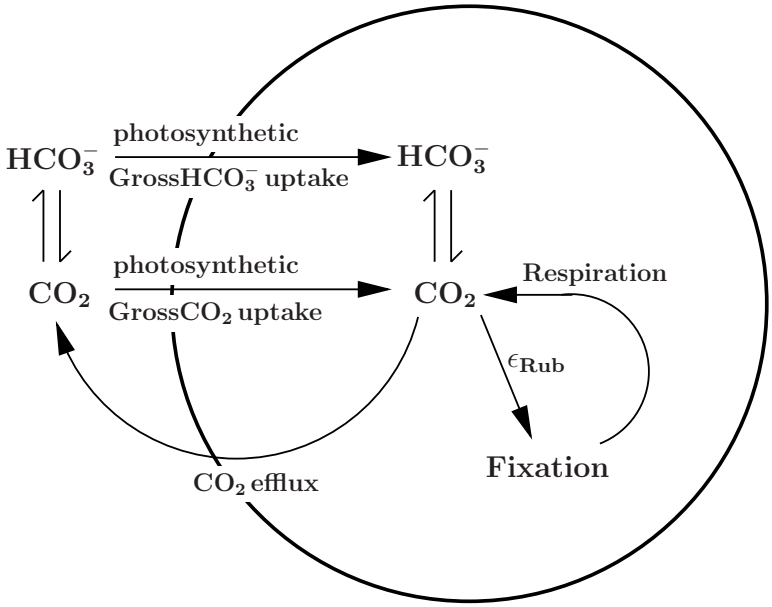

Figure 5: Simple cell model comprising one compartment in which CO_2 and HCO_3^- are taken up. It is assumed that inorganic carbon can leak out of the cell only as CO_2. ϵ_{Rub} illustrates carbon isotope fractionation associated with photosynthetic CO_2 fixation. Total DIC uptake is given by the sum of CO_2 and HCO_3^- uptake. Furthermore, fractionation associated with respiratory processes is considered to be negligible (Raven, 1990)

On the other hand, if leakage approaches zero, all inorganic carbon taken up is being fixed by RubisCO and hence, the carbon isotope composition of the organic matter produced approaches that of the inorganic carbon source. If only CO_2 is taken up ϵ_p will be zero and in the case of purely HCO_3^- uptake ϵ_p will be about $-10‰$.

It has been demonstrated that stable carbon isotope fractionation in marine phytoplankton varies over a wide range, depending on environmental conditions and physiological characteristics of algal species. Carbon isotope fractionation has been first hypothesised to be positively correlated with $[CO_2]$ by Degens et al. (1968). Furthermore, it has been shown

that ϵ_{p} was inversely correlated with growth rate (Fry and Wainright, 1991). To account for the two effects, changes in ϵ_{p} were proposed to be inversely correlated to changes in $\mu/[\mathrm{CO_2}]$ (Laws et al., 1995). However, it has been shown in laboratory cultures that ϵ_{p} is rather insensitive to changes in $[\mathrm{CO_2}]$ within its natural variations (Burkhardt et al., 1999). To complicate things even further, it was pointed out that carbon isotope fractionation is affected by the kind of growth limiting resource (Riebesell et al., 2000). For instance, ϵ_{p} was hardly affected ($2-3‰$) by changes in light intensity, although growth rates varied by a factor of two (Rost et al., 2002).

The basic model given in Eq. 18 indicates that cellular inorganic carbon fluxes and hence modes of carbon acquisition ultimately determine ϵ_{p}. Understanding inorganic carbon acquisition in marine phytoplankton is therefore required for solving the apparent paradoxes associated with stable carbon isotope fractionation (Wolf-Gladrow et al., 1999).

1.7 Inorganic carbon acquisition of marine phytoplankton

During photosynthesis light energy is converted into chemical energy, and ultimately stored in organic carbon compounds. The first step involves light capturing by photosystems I and II, and energy and electron transfers to ATP and NADPH, respectively. These two compounds are then used to fix $\mathrm{CO_2}$ in the Calvin cycle. Photosynthesis in marine phytoplankton can be described as a process in which water is split while $\mathrm{CO_2}$ is reduced as

$$2\mathrm{H_2O} + \mathrm{CO_2} \xrightarrow{\text{Light}} (\mathrm{CH_2O}) + \mathrm{H_2O} + \mathrm{O_2} \tag{19}$$

A significant portion of the photosynthetically generated reductive power (NADPH) and energy (ATP) is allocated by marine phytoplankton to reduce and assimilate inorganic carbon (Falkowski and Raven, 1997). Additionally, most species employ so-called carbon concentrating mechanisms (CCMs) to increase $\mathrm{CO_2}$ concentrations at the site of carboxylation (Badger et al., 1980; Kaplan et al., 1980; Raven and Lucas, 1985; Thomas et al., 2001). Operation of a CCM involves active uptake of $\mathrm{CO_2}$ and/or $\mathrm{HCO_3^-}$, and utilisation of the

enzyme carbonic anhydrase (CA) which accelerates the otherwise relatively slow interconversion rate between CO_2 and HCO_3^-. The reason to increase intracellular concentrations of CO_2 by such energy consuming processes rests on the comparatively low affinity of the main carboxylating enzyme RubisCO for its substrate CO_2, a slow maximum turnover rate and its susceptibility for a competing reaction with O_2 (Badger et al., 1998). A clear indication for active uptake of inorganic carbon is that half saturation constants for photosynthetic carbon fixation in marine phytoplankton range between $1 - 10\,\mu\mathrm{mol\,kg^{-1}}$ (Raven and Johnston, 1991), much lower than those of RubisCO (Badger et al., 1998) (compare Fig. 6).

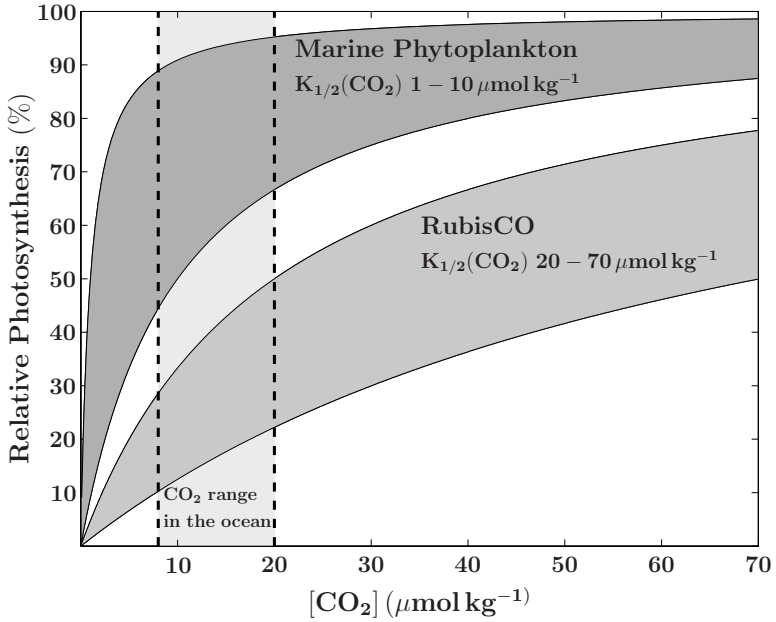

Figure 6: Comparison of CO_2 fixation between marine phytoplankton cells and isolated RubisCO. As $K_{1/2}(CO_2)$ values (half saturation for CO_2) of RubisCO are higher than those of marine phytoplankton cells, maximum rates for photosynthetic carbon fixation in phytoplankton are reached at lower $[CO_2]$ in comparison to RubisCO.

Furthermore, although DIC in the ocean is about 2200 $\mu\mathrm{mol\,kg^{-1}}$, $[CO_2]$ range between 8 and 20 $\mu\mathrm{mol\,kg^{-1}}$ because most DIC is present as HCO_3^- (compare Fig. 4). Hence, active uptake of inorganic carbon allows marine phytoplankton to enhance inorganic carbon fixation at subsaturating ambient $[CO_2]$ (Fig. 6). Additional evidence for operation of

a CCM stems from measurements of internal DIC concentrations in phytoplankton cells which can exceed external concentrations (for a review see Giordano et al. (2005)).

Regulation of CCM activity allows phytoplankton to actively match the supply of inorganic carbon with their demand. Thereby, they can optimise energy and resource allocation efficiencies. Hence, CCM activity is influenced by environmental conditions such as $[CO_2]$ (Rost et al., 2003), light (Beardall, 1991) and temperature (Davison, 1987). Finally, CCM activity is also reflected in the carbon isotope composition of the organic matter built up during photosynthesis. Fractionation is dependent on the ratio of CO_2 to HCO_3^- utilised (note that CO_2 is about $10‰$ depleted in ^{13}C compared to HCO_3^-), and the portion of inorganic carbon taken up which is not fixed by RubisCO but leaks out of the cell, called the leakage (Sharkey and Berry, 1985; Laws et al., 2002; Raven et al., 2002).

The method of choice for investigating inorganic carbon fluxes into and out of a cell is by means of membrane inlet mass spectrometry (MIMS). Basically, the MIMS technique is based on simultaneous $[CO_2]$ and $[O_2]$ measurements during consecutive light and dark cycles where in an initially DIC free assay buffer, DIC is gradually increased (Badger et al., 1994). The fluxes determined are indicative for CCM activity and provide valuable information for our understanding of carbon isotope fractionation in marine phytoplankton as ϵ_p and inorganic carbon fluxes can be considered as the two sides of the same coin (compare Eq. 18).

1.8 Outline of the thesis

This thesis investigates several processes relevant for carbon cycling on various time scales. The publications deal with processes on time scales of millions of years (climate change in the Pleistocene), hundreds and tens of thousands of years (impact of calcification on atmospheric CO_2 at glacial/interglacial change), hours to minutes (CCM activity of phytoplankton) to seconds and micro seconds (kinetics in the carbonate system).

Publication I analyses changes in NH and SH midsummer insolation in the last 2 million

years and suggests a possible trigger for glacial terminations. Glacial climate is proposed to be terminated by simultaneous increases in SH and NH midsummer insolation with a temporal SH lead, termed the 'insolation canon'. Furthermore, it is shown to solve the most striking paradoxes generally associated with orbitally forced climate change.

Publication II investigates the effect of iron and zinc availability on coccolithophorid calcification in *Emiliania huxleyi*. It is demonstrated that at low iron concentrations growth and calcification are equally reduced whereas at low zinc concentrations these two processes are de-coupled. The findings are evaluated in the context of changes in dust input during glacial/interglacial times and possible consequences for CO_2 partitioning between atmosphere and ocean are discussed.

Publication III reports and discusses the findings of publications II in respect to the marine carbon cycle for a general audience.

Publication IV deals with inorganic carbon acquisition and CCM activity in *Emiliania huxleyi* with respect to iron availability. It is shown that uptake rates for CO_2 and HCO_3^- are equally reduced due to iron limitation and that with decreasing growth rates concomitant leakage increases. However, although increasing leakage was proposed to lead to higher carbon isotope fractionation (ϵ_p), measured values for ϵ_p were rather constant. This seeming contradiction is solved by extending a cell model by an additional compartment, representing the chloroplast. This model reveals that the inorganic carbon fluxes in and out of the chloroplast are probably an order of magnitude higher than those in and out of the cell.

Publication V investigates the CO_2 to HCO_3^- inter-conversion kinetics in the carbonate system in pH-buffered seawater. The rate constants determined with this new approach by means of membrane inlet mass spectrometry compare well with calculated rate constants over a range of pH and temperature values. Additionally, a model for the carbonate system in seawater is employed to show how pH buffers operate. This model is also used to address a potential influence of pH buffers on the kinetics of the carbonate system.

1.9 References

Archer, D., Winguth, A., Lea, D., Mahowald, N., 2000. What caused the glacial/interglacial atmospheric $\mathrm{pCO_2}$ cycles. Rev. of Geophysics 38, 159–189.

Archer, D. E., Maier-Reimer, E., 1994. Effect of deep-sea sedimentary calcite preservation on atmospheric $\mathrm{CO_2}$. Nature 367, 260–264.

Badger, M. R., Andrews, T., Whitney, S. M., Ludgwig, M., Yellowlees, D. C., Leggat, W., Price, G. D., 1998. The diversity and coevolution of Rubisco, plastids, pyrenoids, and chloroplast-based $\mathrm{CO_2}$-concentrating mechanisms in algae. Can. J. Bot. 76, 1052–1071.

Badger, M. R., Palmqvist, K., Yu, J.-W., 1994. Measurement of $\mathrm{CO_2}$ and $\mathrm{HCO_3^-}$ fluxes in cyanobacteria and microalgae during steady-state photosynthesis. Physiol. Plant. 90, 529–536.

Badger, M. R. A., Kaplan, A., Berry, J. A., 1980. Internal inorganic carbon pool of *Chlamydomonas reinhardtii* - evidence for a carbon-dioxide concentrating mechanism. Plant. Physiol. 66, 407–413.

Beardall, J., 1991. Effects of photon flux density on the '$\mathrm{CO_2}$-concentrating mechanism' of the cyanobacterium *Anabaena variabilis*. J. Plankt. Res. 13, 133–141.

Broecker, W. S., 1984. Terminations. In: Berger, A. L., Imbrie, J., Hays, J., Kukla, G., Salzman, B. (Eds.), Milankovitch and Climate, Part 2. D. Reidel Publishing Group, pp. 687–698.

Broecker, W. S., Henderson, G., 1998. The sequence of events surrounding Termination II and their implications for the cause of glacial-intergacial $\mathrm{CO_2}$ changes. Paleoceanogr. 13, 352–364.

Broecker, W. S., Peng, T. H., 1982. Tracers in the Sea. Eldigio, New York.

Broecker, W. S., Van Donk, J., 1970. The Shape of Climatic Cycles As Shown By The $\delta^{18}\mathrm{O}$ Record. Rev. of Geophys. and Space Phys. 8, 170–198.

Brownlee, C., Taylor, A., 2004. Calcification in coccolithophores: A cellular perspective. *In* Thierstein, H. R. and Young, J. R. [eds.], Coccolithophores From Molecular Processes to Global Impact. Springer-Verlag Berlin Heidelberg .

Bruland, K. W., 1989. Complexation of zinc by natural organic ligands in the central North Pacific. Limnol. Oceanogr. 34, 269–285.

Burkhardt, S., Riebesell, U., Zondervan, I., 1999. Effects of growth rate, CO_2 concentration, and cell size on the stable carbon isotope fractionation in marine phytoplankton. Geochim. Cosmocim. Acta 63, 3729–3741.

Conkright, M. E., Levitus, S., Boyer, T. P., 1994. World Ocean Atlas 1994 Volume 1: Nutrients. NOAA Atlas NESDIS 1. U.S. Department of Commerce, Washington, D.C.

Crawford, D. W., Lipsen, M. S., Purdie, D. A., Lohan, M. C., Statham, P. J., Whitney, F. A., Putland, J. N., Johnson, W. K., Sutherland, N., Peterson, T. D., Harrison, P. J., Wong, C. S., 2003. Influence of zinc and iron enrichments on phytoplankton growth in the northeastern subarctic Pacific. Limnol. Oceanogr. 48, 1583–1600.

Davison, I., 1987. Adaption of photosynthesis in *Laminaria saccarina* (Phaeophyta) to changes in growth temperature. J. Phycol. 23, 273–283.

de Baar, H. J. W., Boyd, P. W., 2000. The Changing Ocean Carbon Cycle. Hanson, R.B. and Dicklow, H.W. and Fields, J.G., Cambridge Univ. Press, pp. 61-140.

Degens, E., Guillard, R., Sackett, W., Hellbust, J., 1968. Metabolic fractionation of carbon isotopes in marine plankton -I. Temperature and respiration experiments. Deep-Sea Res. 15, 1–9.

DOE, 1994. Handbook of Methods for the Analysis of the Various Parameters of the Carbon Dioxide System in Seawater, version 2. A. G. Dickson and C. Goyet, eds., ORNL/CDIAC-74.

Falkowski, P. G., 1997. Evolution of the nitrogen cycle and its influence on the biological sequestration of CO_2 in the ocean. Nature 387, 272–274.

Falkowski, P. G., Raven, J., 1997. Aquatic photosynthesis. Blackwell Science.

Farquhar, G. D., O'Leary, M. H., Berry, J. A., 1982. On the relationship between carbon isotope discrimination and the intercellular carbon dioxide concentration in leaves. Aust. J. Plant Physiol. 9, 121–137.

Fry, B., Wainright, S. C., 1991. Diatom sources of ^{13}C-rich carbon in marine food webs. Mar. Ecol. Prog. Ser. 76, 149–157.

Giordano, M., Beardall, J., Raven, J. A., 2005. CO_2 Concentrating mechanisms in Algae: Mechanisms, Environmental Modulation, and Evolution. Annu. Rev. Plant Biol. 56, 99–131.

Greene, R. M., Geider, R. J., Falkowski, P. G., 1991. Effect of iron limitation on photosynthesis in a marine diatom. Limnol. Oceanogr. 36, 1772–1782.

Greene, R. M., Geider, R. J., Kolber, Z., Falkowski, P. G., 1992. Iron-induced Changes in Light Harvesting and Photochemical Energy Conversion Processes in Eukaryotic Marine Algae. Plant Physiol. 100, 565–575.

Hansson, I., 1973. A new set of pH-scales and standard buffers for sea water. Deep Sea Res. 20, 479–491.

Harvey, L. D. D., 2001. A quasi-one-dimensional coupled climate-carbon cycle model. 2. The carbon cycle component. J. Geophys. Res. 106, 22,355–22,372.

Houghton, J. T., Meira Fiho, L. G., Bruce, J., Lee, H., Callander, B. A., Haites, E., Harris, N., Maskell, K. (Eds.), 1995. Climate Change 1994. Cambridge Univ. Press, Cambridge, Ch. Radiative Forcing of Climate Change and an Evaluation of the IPCC IS92 Emission Scenairo.

IPCC, 2001. *Climate Change 2001: The Scientific Basis. Contribution of Working Group 1 to the Third Assessment Report of the Intergovernmental Panel on Climate Change*. Houghton, J. T. and Ding, Y. and Griggs, D. J. and Nougher, M. and van der Linden, P. J. and Dai, X. and Maskell, K. and Johnson, C. A. [eds.]. Cambridge University Press, Cambridge, United Kindom and new York, NY, USA.

Kaplan, A., Badger, M. R., Berry, J. A., 1980. Photosynthesis and the intracellular inorganic carbon pool in the bluegreen alga *Anabaena variablis*: response to external $\mathrm{CO_2}$ concentration. Planta 149, 212–226.

Keir, R. S., 1988. On the late Pleistocene ocean geochemistry and circulation. Paleoceanogr. 3, 413–445.

Kremling, K., Streu, P., 2001. The behaviour of dissolved Cd, Co, Zn and Pb in North Atlantic near-surface waters ($30°\mathrm{N}/60°\mathrm{W} - 60°\mathrm{N}/2°\mathrm{W}$). Deep-Sea Res. 48, 2541–2567.

Laws, E. A., Popp, B. N., Bidigare, R. R., Kennicutt, M. C., Macko, S. A., 1995. Dependence of phytoplankton carbon isotopic composition on growth rate and $[\mathrm{CO_2}]_{\mathrm{aq}}$: Theoretical considerations and experimental results. Geochim. Cosmochim. Acta 59, 1131–1138.

Laws, E. A., Popp, B. N., Cassar, N., Tanimoto, J., 2002. $^{13}\mathrm{C}$ discrimination patterns in oceanic phytoplankton: likely influence of $\mathrm{CO_2}$ concentrating mechanisms, and implications for paleoreconstructions. Funct. Plant Biol., 323–333.

Lee, K., Millero, F., Byrne, R., Feely, R., Wanninkhof, R., 2000. The recommended dis-

sociation constants for carbonic acid in seawater. Geophysical Research Letters 27 (2), 229–232.

Lisiecki, L. E., Raymo, M. E., 2005. A Pliocene-Pleistocene stack of 57 globally distributed benthic $\delta^{18}\mathrm{O}$ records. Paleoceanogr. 20.

Lohan, M. C., Statham, P. J., Crawford, D. W., 2002. Total dissolved zinc in the upper water column of the subarctic North East Pacific. Deep-Sea Res. 49, 5793–5808.

Manton, I., Leedale, G. F., 1969. Observations on the microanatomy of *Coccolithus pelagicus* and *Cricosphera carterae*, with special reference to the origin and nature of coccoliths and scales. J. Mar. Biol. Assoc. UK 49, 1–16.

Martin, J. H., 1990. Glacial-interglacial CO_2 change: the iron hypothesis. Paleocenogr. 5, 1–13.

McElroy, M. B., 1983. Marine biological controls on atmospheric CO_2 and climate. Nature 302, 328–329.

Milankovitch, M., 1941. Kanon der Erdbestrahlung und seine Anwendung auf das Eiszeitproblem. Vol. **Spec. Publ. 132** .

Milliman, J. D., 1993. Production and accumulation of calcium carbonate in the ocean: budget of a nonsteady state. Glob. Biogeochem. Cycles 7, 927–957.

Mills, M. M., Ridame, C., Davey, M., La Roche, J., Geider, R. J., 2004. Iron and phosphorous co-limit nitrogen fixation in the eastern tropical North Atlantic. Nature 429, 292–294.

Mook, W. G., 1986. $^{13}\mathrm{C}$ in atmospheric CO_2. Neth. J. Sea Res. 20, 211–223.

Morel, F. M. M., Price, N. M., 2003. The Biogeochemical Cycles of Trace Metals in the Oceans. Science 300, 944–647.

Morel, F. M. M., Reinfelder, J. R., Roberts, S. B., Chamberlain, C. P., Lee, J. G., Yee, D., 1994. Zinc and carbon co-limitation of marine phytoplankton. Nature 369, 740–742.

Petit, J., Jouzel, J., Raynaud, D., Barkov, N., Barnola, J., Basile, I., Benders, M., Chappellaz, J., Davis, M., Delaygue, G., Delmotte, M., Kotlyakov, V., Legrand, M., Lipenkov, V., Lorius, C., Pépin, L., Ritz, C., Saltzman, E., Stievenard, M., 1999. Climate and atmospheric history of the past 420,000 years from the Vostok ice core, Antarctica. Nature 399, 429–236.

Rau, G. H., Riebesell, U., Wolf-Gladrow, D., 1996. A model of photosynthetic ^{13}C fractionation by marine phytoplankton based on diffusive molecular CO_2 uptake. Mar. Ecol. Progr. Ser. 133, 275–285.

Raven, J. A., 1990. Use of isotopes in estimating respiration and photorespiration in microalgae. Mar. Microb. Food Webs 4, 59–86.

Raven, J. A., Johnston, A. M., 1991. Mechanisms of inorganic-carbon acquisition in marine phyoplankton and their implications for the use of other resources. Limnol. Oceanogr. 36, 1701–1714.

Raven, J. A., Johnston, A. M., Kübler, J. E., Korb, R. E., McInroy, S. G., Handley, L. L., Scrimgeour, C. M., Walker, D. I., Beardall, J., Vanderklift, M., Fredriksen, S., Dunton, J. H., 2002. Mechanistic interpretation of carbon isotope discrimination by marine macroalgae and seagras. Funct. Plant Biol. 29, 355–378.

Raven, J. A., Lucas, W. J., 1985. Energy costs of carbon acquisition, p. 305-324 *In* Lucas, W. J. and Berry, J. A. [eds.], Inorganic carbon Uptake by Aquatic Photosynthetic Organisms. American Society of Plant Physiologists.

Riebesell, U., Burkhardt, S., Dauelsberg, A., Kroon, B., 2000. Carbon isotope fractionation by a marine diatom: dependence on the growth-rate-limiting resource. Mar. Ecol. Progr. Ser. 193, 295–303.

Roeske, C., O'Leary, M., 1984. Carbon isotope effects on the enzyme-catalyzed carboxilation of ribulose bisphosphate. Biochem. 23, 6275–6285.

Rost, B., Riebesell, U., Burkhardt, S., Sültemeyer, D., 2003. Carbon acquistion of bloom-forming marine phytoplankton. Limnol. Oceanogr. 48, 55–67.

Rost, B., Zondervan, I., Riebesell, U., 2002. Light-dependent carbon isotope fractionation in the coccolithophore *Emiliania huxleyi*. Limnol. Oceanogr. 47, 120–128.

Rowson, J. D., Leadbeater, B. S. C., Green, J. C., 1986. Calcium carbonate deposition in the motile (*Crystallolithus*) phase of *Coccolithus pelagicus*. Brit. Phycol. J. 21, 359–370.

Sabine, C. L., Feely, R. A., Gruber, N., Key, R. M., Lee, K., Bullister, J. L., Wanninkhof, R., Wong, C. S., Wallace, D. W. E., Tilbrook, B., Millero, F. J., Peng, T.-H., Kozyr, A., Ono, T., Rios, A. F., 2004. The Oceanic Sink for Anthropogenic CO_2. Science 305, 367–371.

Shackelton, N. J., 2000. The 100,000-Year Ice-Age Cycle Identified and Found to Lag Temperature, Carbon Dioxide and Orbital Eccentricity. Science 289, 1897–1902.

Shackleton, N. J., 1997. Carbon 13 in Uvigerina: Tropical rainforest history and the equatorial Pacific carbonate dissolution cycles. *In*: The Fate of Fossil Fuel CO_2 in the Oceans. Andersen, N. R. and Malahoff, A. (eds.). Plenum, New York .

Sharkey, T. D., Berry, J. A., 1985. Carbon isotope fractionation of algae as influenced by an inducible CO_2 concentrating mechanism *In* Lucas, W. J. and Berry, J. A. [eds.], Inorganic carbon Uptake by Aquatic Photosynthetic Organisms. American Society of Plant Physiologists.

Siegenthaler, U., Sarmiento, J., 1993. Atmospheric carbon dioxide and the ocean. Nature 365, 119–125.

Sigman, D. M., McCorcle, D. C., Martin, W. R., 1998. The calcite lysocline as a constraint on glacial/interglacial low-latitude production changes. Glob. Biogeochem. Cycles 12, 409–427.

Stoll, H. M., Ziveri, P., 2004. Coccolithophorid-based geochemical paleoproxies *In* Thierstein, H. R. and Young, J. R. [eds.], Coccolithophores From Molecular Processes to Global Impact. Springer-Verlag Berlin Heidelberg.

Sundquist, E., 1993. The global carbon dioxide budget. Science 259, 934–941.

Thomas, S., Pahlow, M., Wolf-Gladrow, D. A., 2001. Model of the Carbon Concentrating Mechanism in Chloroplasts of Eukaryotic Algae. J. theor. Biol. 208, 295–313.

Toggweiler, J. R., 1999. Variation of atmospheric CO_2 by ventilation of the ocean's deepest water. Paleoceanogr. 14, 571–588.

Vallee, B., Auld, D., 1990. Zinc coordination, function and structure of zinc enzymes and other proteins. Biochemistry 29 (24), 5647–5659.

Volk, T., Hoffert, M. I., 1985. Ocean carbon pumps: analysis of relative strengths and efficiencies in ocean-driven atmospheric CO_2 changes *In*: Sunquist, E. T and Broecker, W. S. [eds.], The carbon cycle and atmospheric CO_2: natural variation archean to present. American Geophysical Union, Washington, DC, Geophysical Monograph 32.

Westbroek, P., Young, J. R., Linschooten, K., 1989. Coccolith production (biomineralization) in the marine alga *Emiliania huxleyi*. J. Protozool. 36, 368–373.

Winter, A., Siesser, W. G. (Eds.), 1994. Coccolithopores. Cambridge University Press.

Wolf-Gladrow, D., Burkhardt, S. A., Riebesell, U., 1999. Carbon isotopic fractionation in microalgae: the effect of intracellular compartments. ASLO, Santa Fé, http://aslo.org/meetings/santafe99/abstracts/SS32MO0245E.html.

Yamanaka, Y., Tajika, E., 1996. The role of the vertical fluxes of particulate organic matter and calcite in the oceanic carbon cycle: Studies using an ocean biogeochemical general circulation model. Global Biogeochem. Cycles 10, 361–382.

Zeebe, R. E., Wolf-Gladrow, D., 2001. CO_2 in seawater: equilibrium, kinetics, isotopes. Vol. 65 of Elsevier Oceanography Series. Elsevier.

2 PUBLICATIONS

2.1 List of Publications

This doctoral thesis is based on the following publications:

I Kai G. Schulz & Richard E. Zeebe. Pleistocene glacial terminations triggered by Southern and Northern Hemisphere insolation canon. submitted to *Earth Planetary Science Letters*.

II Kai G. Schulz, Ingrid Zondervan, Loes, J. A. Gerringa, Klaas R. Timmermans, Marcel J. W. Veldhuis & Ulf Riebesell, 2004. Effect of trace metal availability on coccolithophorid calcification. *Nature* 430,673-676.

III Kai G. Schulz & Ulf Riebesell, 2004. Der ozeanische Kalkregen. *Naturwissenschaftliche Rundschau* 12, 686-688.

IV Kai G. Schulz, Ulf Riebesell, Björn Rost, Silke Thoms & Dieter A. Wolf-Gladrow. Iron availability and the regulation of inorganic carbon acquisition in *Emiliania huxleyi* with respect to carbon isotope fractionation. to be submitted to *Limnology and Oceanography*.

V Kai G. Schulz, Ulf Riebesell, Björn Rost, Silke Thoms & Richard E. Zeebe. Determination of the rate constants for the carbon dioxide to bicarbonate inter-conversion in pH buffered seawater systems. accepted by *Marine Chemistry*.

2.2 Erklärung über den von mir geleisteten Anteil an den Publikationen

Publikation I

Die Idee zu dieser Arbeit stammt von mir. Die mathematische Analyse der Insolationskurven wurde von mir mit Unterstützung von Richard E. Zeebe durchgeführt. Das Manuskript wurde von mir in Zusammenarbeit mit Richard E. Zeebe verfaßt.

Publikation II

Die Laborexperimente wurden zusammen mit Ingrid Zondervan geplant und durchgeführt. Die Auswertung, die Interpretation der Daten und das Verfassen des Manuskriptes habe ich in Zusammenarbeit mit den Koautoren durchgeführt.

Publikation III

Das Manuskript habe ich in Zusammenarbeit mit Ulf Riebesell verfaßt.

Publikation IV

Die Planung und Durchführung der Experimente erfolgte in Zusammenarbeit mit Björn Rost. Die Entwicklung der Gleichungen, welche das Karbonatsystem beschreiben, geschah im Austausch mit Richard E. Zeebe. Die Auswertung, die Interpretation der Daten und das Verfassen des Manuskriptes habe ich in Zusammenarbeit mit den Koautoren durchgeführt.

Publikation V

Die Planung und Durchführung der Experimente geschah in Zusammenarbeit mit Björn Rost. Die Auswertung, die Interpretation der Daten und das Verfassen des Manuskriptes habe ich in Zusammenarbeit mit den Koautoren durchgeführt.

Pleistocene glacial terminations triggered by Southern and Northern Hemisphere insolation canon

K.G. Schulz[1*], R.E. Zeebe[2]

[1]Leibniz Institute for Marine Sciences, Düsternbrooker Weg 20, 24105 Kiel, Germany

[2]University of Hawaii at Manoa SOEST Department of Oceanography 1000 Pope Road, MSB 504 Honolulu, HI 96822, USA

[*]Corresponding author: kschulz@ifm-geomar.de (K.G. Schulz)
phone: 0049 (0)431 600 4510
fax: 0049 (0)431 600 1515

submitted to *Earth Planetary Science Letters*

Abstract

Throughout the last ~ 900 kyr, the Late Pleistocene, Earth has experienced periods of cold glacial climate, punctuated by seven abrupt transitions to warm interglacials, the so-called terminations. Although most of glacial ice is located in the Northern Hemisphere (NH), the Southern Hemisphere (SH) seems to play a crucial role in deglaciation. Variation in the seasonal distribution of solar insolation is one candidate for the cause of these climatic shifts. But so far, no simple mechanism has been identified. Here we present a mathematical analysis of variations in midsummer insolation in both hemispheres at 65° latitude. Applying this analysis to the entire Pleistocene, the last 2 Myr, we find that prior to each termination the insolation in both hemispheres increases in concert, with a SH lead. Introducing time and energy thresholds to these overlaps, calculated times for the onsets of the seven terminations by this insolation canon are $\sim 23, 139, 253, 345, 419, 546$ and 632 kyr BP, perfectly matching the geologic record. Moreover, the timing originates from the interplay between the two orbital parameters of obliquity and precession, explaining why terminations occur at integer multiple of the precessional cycle. Furthermore, there is no such constellation between 1 and 2 Myr BP, the Early Pleistocene, in agreement with Earth's climate at that time. This change in orbital forcing coincides with the Mid Pleistocene Revolution, separating the Late from the Early Pleistocene. Therefore, we propose the insolation canon to be the trigger for glacial terminations.

Keywords: Glacial terminations, insolation, Northern Hemisphere, Southern Hemisphere

1 Introduction

Earth has gone through large climatic shifts during the past ~ 900 kyr with seven major glaciations (Broecker and Van Donk, 1970; Broecker, 1984) (see Fig. 1A). These glaciations were punctuated by seven mostly rapid transitions to warm interglacial climate conditions, occurring approximately every 100 kyr (Fig. 1B). This feature is absent in climate records from the Early Pleistocene (1.1 - 2 Myr), which are dominated by a 41 kyr periodicity (Fig. 1C), marking the Mid Pleistocene Revolution (MPR). The so-called 100 kyr glacial/interglacial cycles are associated with the built-up and melting of enormous Northern Hemisphere (NH) ice sheets extending over Canada and Scandinavia. Therefore, it has been suggested that changes in NH summer insolation are driving these climatic events (Milankovitch, 1941). However, only recently it became apparent that also the ice in the the Southern Hemisphere (SH) is reacting to glacial terminations (Weaver et al., 2003) and that the Antarctic might play a pivotal role in these climatic shifts (Knorr and Lohmann, 2003; Peeters et al., 2004). Additionally, considering changes in NH insolation as the sole driver poses several paradoxes. The astronomical theory of long-term changes in orbital parameters (Milankovitch, 1941; Berger, 1978; Berger and Loutre, 1991; Laskar et al., 2004) predicts quasi-periodic variations of eccentricity, obliquity and precession with dominant frequencies centered around 100, 41 and 23/19 kyr, respectively. While the 19/23 and 41 kyr cycles have been demonstrated to be coherent with the amplitude of NH insolation forcing in numerous climate records (Imbrie et al., 1993), the quasi 100 kyr glacial/interglacial cycle remains a mystery, since the amplitude of the eccentricity forcing is much too small to drive this cycle. Furthermore, the eccentricity forcing is partly out of phase (Imbrie et al., 1993). Besides this '100 kyr problem', explanation for the 'stage 11 problem' (the most prominent termination occurs at times of comparatively low orbital variations) and the 'Late Pleistocene transition problem' (the miraculous shift of climate cyclicity at the MPR) are still lacking (Paillard, 2001). Given the apparent involvement of both hemispheres in glacial terminations, a mechanism triggering this global phenomenon should therefore not

only provide answers to the paradoxes outlined above but also encompass and connect both hemispheres.

2 Methods

2.1 Concept of Insolation Analysis

We analyzed changes in midsummer insolation at 65° North (June 21) together with corresponding changes in the South (December 21) of the last 2 Myr using the astronomical solution given in (Laskar et al., 2004) (see next section for details). We found that prior to each termination the insolation in both hemispheres is increasing simultaneously and that the SH increase leads the NH, a feature we refer to as 'overlap' hereafter. Further analysis led us to postulate three prerequisites for a termination. First, and most importantly, the overlap has to be equal to or longer than 1000 years. Second, Earth's climate has to be in a full glacial mode, i.e. there must be '100 kyr ice' (Raymo, 1997) present in order to be terminated. Third, total energy supplied during the increase of southern and northern midsummer insolation has to exceed a threshold of $0.95\,\mathrm{TJ\,m^{-2}}$, which is the lowest observed at a termination. These three thresholds, simply postulated here, are interpreted and discussed in section 4.1. In general, however, thresholds between the two extreme states of glacial and interglacial climate (here, time and energy) can be considered the simplest representation for Earth's nonlinear climate system (Paillard, 1998; Paillard and Parrenin, 2004).

2.2 Details of Insolation Analysis

The analysis of variations in midsummer insolation changes at 65° North and South, the summer solstices, was performed on the (1,1) astronomical solution for Earth's orbital parameters given in (Laskar et al., 2004) with a solar constant set to 1368 $\mathrm{W\,m^{-2}}$ at a step size of 100 yr (provided by J. Laskar). This astronomical solution incorporates present

day values for dynamical ellipticity and tidal dissipation (1,1). Changes in tidal dissipation, resulting from the stresses exerted on Earth by the Moon and the Sun, and dynamical ellipticity, associated with mass load redistribution, e.g. during ice-age cycles, influence the phasing of precession and obliquity (Laskar et al., 1993). However, it is reasonable to use present day values and to keep them constant, as they remained close to todays values during the last millions of years (Pälike and Shackleton, 2000; Lourens et al., 2001).

We thoroughly checked whether the overlaps, the synchronous increase in SH and NH insolation with a SH lead, determined with this astronomical solution depends on the solution employed for Earth's orbital elements. Using the solution given in (Berger, 1978) for the last 800 kyr and the solution given in (Berger and Loutre, 1991) for the time between 0.8 and 2 Myr BP, we obtained essentially the same results. Thus, the overlaps are a robust feature of different solutions for Earth's orbital parameters.

3 Results

3.1 Linking Overlaps and Terminations

In the following the chronology of events around a glacial termination is described, as detected by our analysis (see Fig. 2A). 1) The SH midsummer insolation reaches a minimum ($\mathrm{t}_0^{\mathrm{S}}$) and starts to increase, defined here as Onset of SH Forcing (OSF). 2) While the SH insolation is still increasing, the NH insolation reaches a minimum ($\mathrm{t}_0^{\mathrm{N}}$) and also starts to rise. 3) After 1000 years of simultaneous increase the onset of a termination (OT) is triggered. Shortly after this event, SH insolation reaches a maximum and starts to decrease. 4) NH insolation continues to increase until reaching a maximum 10-15 kyr later.

Only at a glacial termination the increase in SH and NH midsummer insolation exceeds the threshold of $0.95\,\mathrm{TJm}^{-2}$ and the overlap is at least 1000 years long (Fig. 2B). The resulting OTs perfectly match the geologic record (Fig. 3A), coinciding with marine $\delta^{18}\mathrm{O}$ maxima, which in a first approximation reflect maxima in ice sheet extension (Shackelton,

2000). Additionally, the OTs which we date 23.1, 139.1, 253.3, 345.4, 418.6, 546.2 and 632.3 kyr BP roughly occur 10 kyr prior to the corresponding midpoint of termination, as suggested by various marine δ^{18}O records (Tab. 1). An exception is termination V, where OT and the midpoint of termination are indistinguishably close. Moreover, the time intervals between our onsets of terminations of 86, 128, 73, 92, 114, 116 kyr (terminations VII-VI, VI-V, V-IV, IV-III, III-II, II-I, respectively) agree very well with intervals between midpoints of terminations in marine δ^{18}O records, independent of the dating method applied (Tab. 1).

In addition to the sound prediction of the timing of glacial terminations there are three interesting results. First, there are two times at which only shortly after a termination an overlap longer than 1000 yr occurs. Event A lies between termination IV and III at 302.4 kyr and Event B between termination V and IV at 381.3 kyr BP (Fig. 4A). As those events occur only 40 kyr after a termination, no glacial climate could be 'terminated'. Second, there is not a single termination trigger between 2 Myr and 1 Myr (Fig. 4B), agreeing perfectly with the geologic record. Third, our analysis reveals one 'additional' termination trigger at 925.6 kyr BP, roughly coinciding with the mid-Pleistocene revolution (MPR), the switch from a 41 kyr to a 100 kyr dominated climate signal (Raymo and Nisancioglu, 2003).

3.2 Origin of Overlaps

The question arises, how the overlaps identified above are generated and what is determining their duration. In order to separate the individual influence of each of the orbital parameters precession, obliquity and eccentricity, we analyzed artificial insolation curves generated using routines given in (Berger, 1978) and (Laskar et al., 2004). With obliquity set constant at any arbitrary value, all overlaps disappear because SH and NH insolation changes are then exactly anti-phased. With eccentricity set constant at values within its natural variability (see Fig. 3B) of 0.02, 0.03, and 0.04, the structure and timing of overlaps is preserved. However, the overlap duration increases with decreasing eccentricity.

Setting the precessional parameter ' longitude of perihelion' constant (this corresponds to fixing the summer solstices on Earth's orbit at a constant angle to perihelion), there are overlaps (except for $0/360^\circ$ or 180°) but their timing and length depend on the actual angle considered.

Thus, the termination trigger identified here as a synchronous, prolonged ($\geq 1000\,\mathrm{yr}$) increase in SH and NH insolation stems from an interplay between the three orbital parameters precession, obliquity and eccentricity. In analogy to its counterpart in music we refer to it as the insolation canon. The timing of all overlaps is generated by a modulation of insolation through variations in obliquity and precession. This readily explains why the time interval between two consecutive terminations is always an integer multiple of the precessional cycles in this interval (Ridgwell et al., 1999). The duration of an overlap, however, is modulated also by eccentricity. Therefore, the absolute value of eccentricity is not irrelevant to the occurrence of overlaps > 1000 yr, the insolation canon.

4 Discussion

4.1 Possible Feedback Mechanisms

The mathematical analysis presented here is capable of identifying all seven Late Pleistocene glacial terminations. It is free of interpretation or speculation regarding the response of Earth's climate system, which ultimately leads to deglaciation. However, the two thresholds of time and energy, fundamental to our termination trigger, suggest the involvement of particular feedback mechanisms. The necessity for a certain amount of energy supplied to the Antarctic and Arctic in the summer seasons indicates that sea-/land-ice melting, impacting deep water formation, are pivotal for these dramatic climate shifts. Although the responsible feedback between high latitude SH insolation forcing and the temporal SH lead during ice-age terminations has yet to be identified, the very feedbacks described above have been demonstrated operating during glacial terminations in the Antarctic (Knorr and

Lohmann, 2003; Stocker, 2003; Peeters et al., 2004). These findings alone imply a dominant role of the SH during the initiation of deglaciation. However, according to our analysis, only the simultaneous increase in high latitude midsummer insolation in both hemispheres can push Earth's climate out of glacial conditions. We suggest that the tele-connection required is established by ocean circulation which has a typical time scale of ~ 1000 years as our time threshold. The necessity for SH and NH synchrony may be found in the concept of the bipolar seesaw (Broecker, 1998). It has been observed that warming in the South leads to cooling in the North and vice versa (Blunier and Brook, 2001; Jouzel et al., 1995). Hence, a SH decrease in insolation always amplifies the NH warming forcing by insolation because SH and NH insolation changes are almost completely anti-phased. However, during the rare events of synchronous insolation increase (overlaps) both hemispheres would warm in parallel by this insolation canon. Thus, simultaneous warming could be pictured as repeated upward pushing at both ends of the seesaw, elevating its fulcrum point. This elevation might be thought to change temperature and ocean circulation and ultimately set the stage for melting of the enormous '100 kyr' ice sheets in both hemispheres and thus for the transition to interglacial climate conditions.

4.2 Leads and Lags around a Termination: Phase Differences between NH and SH?

There is an ongoing debate whether the warming signal at a termination was synchronous in both NH and SH or whether one hemisphere was leading the other (Sowers and Bender, 1995; Alley et al., 2002). Although the insolation canon identified by our analysis encompasses both hemispheres, it originates in the SH as the increase in midsummer insolation at $65°\mathrm{S}$ occurs about 10 kyr prior to its NH counterpart. Hence, we would expect that around a termination changes of $\delta^{18}\mathrm{O}$ or $\delta\mathrm{D}$, proxies for local temperature, in Antarctic ice would precede those in Arctic ice. Unfortunately, direct comparison of Antarctic and Arctic climate records is difficult as uncertainties arise from translating core depth to calendar age

and synchronizing NH and SH records to a uniform time scale. Nonetheless, the SH origin of the insolation canon suggests that, if there are phase differences between NH and SH warming around a termination, it would rather be a SH lead than a lag.

4.3 The Three Classical Problems

Although the concept of the insolation canon provides a possible solution for the '100 kyr problem', one of the three classical problems of Pleistocene research (Paillard, 2001), several questions remain regarding the other two problems ('Late Pleistocene transition' and 'stage 11').

The Late Pleistocene transition problem: While our analysis provides the trigger for glacial terminations, the feedback involved in the initiation of a glaciation itself remains unclear. However, besides the finding that the orbital forcing changed in the Pleistocene about 1 Myr BP at the MPR (i.e. the absence of the insolation canon in the Early and its occurrence in the Late Pleistocene), our analysis furthermore identifies two extra clues for the beginning of the 100 kyr glaciations after the MPR. 1) The first occurrence of the insolation canon is dated at 926 kyr BP. This may have shifted Earth's climate system to a different mode of operation, leading to the initiation of 100 kyr ice sheets. 2) A 'negative' forcing, analogous to the 'positive' forcing (Fig. 2B), could be involved, i.e. synchronous midsummer insolation decrease in both hemispheres with a SH lead. In the last 2 Myr this opposing 'negative' forcing exhibits a similar distribution and energy pattern as the 'positive' termination forcing (Fig. 5). Applying the same energy and time thresholds, there is only one of these events prior to the MPR compared to eight afterwards. Interestingly, the first occurrence of such 'negative' insolation canon in the Late Pleistocene is 650 kyr BP, only about 20 kyr before termination VII. In this short period of time, marine $\delta^{18}\mathrm{O}$ reached a hitherto unprecedented high value. (compare Fig. 1A and Fig. 3A).

The stage 11 problem: At first glance the problem that the most prominent termination occurs at times of comparatively low orbital variation seems to escape elucidation. Howe-

ver, our analysis detects a feature at termination V which makes it unique. The fact that termination V is the most prominent one is possibly the consequence of the longest time interval ever observed between two terminations. Because there was no termination trigger after termination VI for 128 kyr, Earth's climate system went deeply into a full glacial mode and therefore would have responded strongly to the occurrence of the insolation canon at termination V. Also interesting in this context is that the midpoint of termination V from various $\delta^{18}\mathrm{O}$ records (Tab. 1) is indistinguishably close to OT. Yet, in recent $\delta\mathrm{D}$ ice core data from Antarctica (EPICA community members, 2004), our OSF exactly matches the increase of $\delta\mathrm{D}$ at termination V.

4.4 The Future

For the future, our analysis predicts the next termination trigger 53.4 kyr from now. However, model simulations predict an exceptionally long interglacial of 50 kyr ahead (see (Berger and Loutre, 2002) and references therein) with the next glacial maximum and subsequent termination in 100 kyr. These models are highly sensitive to atmospheric CO_2, producing almost no NH glaciation with conditions above 290 ppmv. It is therefore questionable whether there will be any glaciation in the coming 100 kyr because atmospheric CO_2 is likely to stabilize around 400 ppmv 10 kyr from now (Archer et al., 1998) as a long-term result of fossil fuel burning by humans.

5 Conclusions

Our analysis of changes in SH and NH midsummer insolation during the entire Pleistocene, the last 2 M years, has revealed a possible trigger for the global phenomenon of glacial terminations. The onset of the seven Late Pleistocene terminations is dated by this trigger to have occurred 23.1, 139.1, 253.3, 345.4, 418.6, 546.2 and 632.3 kyr BP, in agreement with various marine $\delta^{18}\mathrm{O}$ records.

The trigger is identified as a prolonged increase in midsummer insolation in both hemispheres, with a temporal SH lead (the insolation canon). This is consistent with observations of the pivotal role of the SH in the initiation of deglaciations (Weaver et al., 2003; Knorr and Lohmann, 2003; Peeters et al., 2004). Furthermore, we showed that the timing of the insolation canon stems from insolation modulation through obliquity and precession, thereby providing an explanation why terminations occur at integer multiple of the precessional cycle. Moreover, we find a change in orbital forcing about 1 Myr BP at the Mid Pleistocene Revolution. The trigger is only existent in the Late Pleistocene while it is absent between 1 and 2 M years BP, the Early Pleistocene, in agreement with Earth's climate at that time.

Acknowledgments

To be added

References

Alley, R. B., Brook, E. J., Anandakrishnan, S., 2002. A northern lead in the orbital band: north-south phasing of ice-age events. Quat. Sci. Rev. 21, 431–441.

Archer, D., Kheshgi, H., Maier-Reimer, E., 1998. Dynamics of fossil fuel CO_2 neutralization by marine $CaCO_3$. Glob. Biochem. Cycles 12, 259–276.

Berger, A., 1978. Long-term variations of daily insolation and Quaternary climatic changes. J. Atmos. Sc 35, 2362–2367.

Berger, A., Loutre, M., 2002. An Exceptionally Long Interglacial Ahead? Science 297, 1287–1288.

Berger, A., Loutre, M. F., 1991. Insolation values for the climate of the last 10 million years. Quat. Sc. Rev. 10, 297–317.

Blunier, T., Brook, E. J., 2001. Timing of Millennial-Scale Climate Change in Antarctica and Greenland During the Last Glacial Period. Science 291, 109–112.

Broecker, W. S., 1984. Terminations. In: Berger, A. L., Imbrie, J., Hays, J., Kukla, G., Salzman, B. (Eds.), Milankovitch and Climate, Part 2. D. Reidel Publishing Group, pp. 687–698.

Broecker, W. S., 1998. Paleocean circulation during the last deglaciation. Paleoceanogr. 13, 119–121.

Broecker, W. S., Van Donk, J., 1970. The Shape of Climatic Cycles As Shown By The $\delta^{18}O$ Record. Rev. of Geophys. and Space Phys. 8, 170–198.

EPICA community members, 2004. Eight glacial cylces from an Antarctic ice core. Nature 429, 623–628.

Huybers, P., Wunsch, C., 2004. A depth-derived Pleistocene age model: Uncertainty estimates, sedimentation variability, and nonlinear climate change. Paleocenogr. 19 (1).

Imbrie, J., Berger, A., Boyle, E. A., Clemens, S. C., Duffy, A., Howard, W., Kukla, G., Kutzbach, J., Martinson, D. G., McIntyre, A., Mix, A. C., Molfino, B., Morley, J. J., Peterson, L. C., Pisias, N. G., Prell, W. L., Raymo, M. E., Shackelton, N. J., Toggweiler, J. R., 1993. On the structure and origin of major glaciation cycles 2. the 100.000-year cycle. Paleoceanogr. 8, 699–735.

Imbrie, J., Hays, J. D., Martinson, D., McIntyre, A., Mix, A. C., Morley, J. J., Pisias, N. G., Prell, W. L., Shackleton, N. J., 1984. The orbital theory of Pleistocence climate: Support from a revised chronology of the marine δ^{18}O record. In: Berger, A. L., Imbrie, J., Hays, J., Kukla, G., Salzman, B. (Eds.), Milankovitch and Climate, Part 1. D. Reidel Publishing Group, pp. 269–305.

Jouzel, J., Vaikmae, R., Petit, J. R., Martin, M., Duclos, Y., Stievenard, M., Lorius, C., Toots, M., Mélières, Burckle, L. H., Barkov, N. I., Kotlyakov, V. M., 1995. The two-step shape and timing of the last deglaciation in Antarctica. Clim. Dyn. 11, 151–161.

Knorr, G., Lohmann, G., 2003. Southern Ocean origin for the resumption of Atlantic thermohaline circulation during deglaciation. Nature 424, 532–536.

Laskar, J., Joutel, F., Boudin, F., 1993. Orbital, precessional, and insolation quantities from the Earth from -20Myr to +10Myr. Astron. Astrophys. 270, 522–533.

Laskar, J., Robutel, P., Joutel, F., Gastineau, M., Correia, A.C.M. Levrard, B., thishadtobeincluded, T., 2004. A long term numerical solution for the insolation quantities of the earth. Astron. Astrophys. 428, 261–285.

Lisiecki, L. E., Raymo, M. E., 2005. A Pliocene-Pleistocene stack of 57 globally distributed benthic δ^{18}O records. Paleoceanogr. 20.

Lourens, L. J., Wehausen, R., Brumsack, H., 2001. Geological constraints on tidal dissipation and dynamical ellipticity of the earth over the past three million years. Nature 409, 1029–1033.

Milankovitch, M., 1941. Kanon der Erdbestrahlung und seine Anwendung auf das Eiszeitproblem. Vol. **Spec. Publ. 132** .

Paillard, D., 1998. The timing of Pleistocene glaciations from a simple multiple-state model. Nature 391, 378–381.

Paillard, D., 2001. Glacial cylces: towards a new paradigm. Rev. Geophys. 39, 325–346.

Paillard, D., Parrenin, F., 2004. The Antarctic ice sheet and the triggering of deglaciations. Earth Planet. Sci. Lett. 227, 263–271.

Pälike, H., Shackleton, N. J., 2000. Constraints on astronomical parameters from the geologic record for the last 25 Myr. Earth. Planet. Sci. Lett. 182, 1–14.

Peeters, F. J. C., Acheson, R., Bummer, G. J. A., de Ruijter, W. P. M., Schneider, R. R., Ganssen, G. M. Ufkes, E., Kroon, D., 2004. Vigorous exchange between the Indian and Atlantic oceans at the end of the past five glacial periods . Nature 430, 661–665.

Raymo, M. E., 1997. The timing of major climate terminations. Paleoceanogr. 12, 577–585.

Raymo, M. E., Nisancioglu, K., 2003. The 41 kyr world: Milankovitch's other unsolved mystery. Paleoceanogr. 18 (1).

Ridgwell, A. J., Watson, A. J., Raymo, M. E., 1999. Is the spectral signiture of the 100 kyr glacial cycle consistent with a Milankovitch origin. Paleoceanogr. 14, 437–440.

Shackelton, N. J., 2000. The 100,000-Year Ice-Age Cylce Identified and Found to Lag Temperature, Carbon Dioxide and Orbital Eccentricity. Science 289, 1897–1902.

Sowers, T., Bender, M., 1995. Climate Records Covering the Last Deglaciation. Science 269, 210–214.

Stocker, T. F., 2003. South dials north. Nature 424, 496–499.

Weaver, A. J., Saenko, O. A., Clark, P. U., Mitrovica, J. X., 2003. Meltwater Pulse 1A from Antarctica as a Trigger of the Bølling-Allerød Warm Interval. Science 299, 1709–1713.

Figure 1 Comparison of climate variability in the Late Pleistocene (100 kyr world) and the Early Pleistocene (41 kyr world). (**A**) $\delta^{18}\mathrm{O}$ of the LR04 benthic stack (Lisiecki and Raymo, 2005) against time over the entire Pleistocene. The Mid Pleistocene Revolution (MPR) marks the shift from the 41 kyr to the 100 kyr world. The seven glacial terminations of the Late Pleistocene are shown in Roman numbers. (**B**) Power spectral densities of the above $\delta^{18}\mathrm{O}$ signal against their frequencies during the last 900 kyr, the Late Pleistocene, and (**C**) between 1100 to 2000 kyr BP, the Early Pleistocene.

Figure 2 Graphical illustration of the mathematical analysis used to identify terminations (shown in Roman numbers). (**A**) Northern midsummer insolation at 65° N (blue), its extrema (circles), and southern midsummer insolation at 65° S (red) and its extrema (circles) against time. $\mathrm{t}_0^{\mathrm{S}}$ and $\mathrm{t}_0^{\mathrm{N}}$ are the times for the onset of SH and NH insolation increase and $\mathrm{t}_\mathrm{i}^{\mathrm{S}}$ and $\mathrm{t}_\mathrm{i}^{\mathrm{N}}$ are their following maxima, respectively. $\mathrm{t}_0^{\mathrm{S}}$ is defined as the Onset of Southern Hemisphere Forcing (OSF) and 1000 years after $\mathrm{t}_0^{\mathrm{N}}$, the Onset of Termination (OT) is triggered, as marked by vertical lines. Shaded red areas illustrate the overlaps during SH and NH insolation increase, the insolation canon. Note that a prerequisite for this overlap is that the SH precedes the NH midsummer insolation increase. The shaded blue area highlights the time overlap during SH and NH insolation decrease, with a SH lead ('negative' insolation canon) prior to termination I (see text for details).(**B**) Thick blue bars represent the length of an overlap which meets our three termination conditions. Yellow bars denote the total energy supplied during the corresponding increase of southern and northern midsummer insolation ($\mathrm{I_S}$ and $\mathrm{I_N}$, respectively), i.e. $\mathrm{E} = \int_{\mathrm{t}_0^{\mathrm{S}}}^{\mathrm{t}_\mathrm{i}^{\mathrm{S}}} \mathrm{I_S(t)\,dt} + \int_{\mathrm{t}_0^{\mathrm{N}}}^{\mathrm{t}_\mathrm{i}^{\mathrm{N}}} \mathrm{I_N(t)\,dt}$. Thin blue bars represent overlaps shorter than 1000 years (pos. ordinate) and overlaps of the 'negative' insolation canon (neg. ordinate).

Figure 3 Comparison of the stacked $\delta^{18}\mathrm{O}$ LR04 record (Lisiecki and Raymo, 2005), terminations and eccentricity forcing. (**A**) $\delta^{18}\mathrm{O}$ of this benthic stack against time (black line).

Roman numbers indicate terminations. Blue circles and vertical lines represent the times of the Onset of Termination (OT), as determined in this study (see text for details). Red circles denote the Onset of Southern Hemisphere Forcing (OSF) before a termination, i.e. the start of increasing midsummer insolation at 65° S. See also Tab. 1 for a detailed comparison of OT with terminations determined in various marine $\delta^{18}\mathrm{O}$ records. (**B**) Eccentricity variations according to the astronomical solution of (Berger, 1978) (red) and (Laskar et al., 2004) (blue) against time.

Figure 4 All overlaps of the last 2 Myr and corresponding energy (energy only shown if overlap is equal to or longer than 1000 yr). Blue bars in **A)** (0-1 Myr BP) and **B)** (1-2 Myr BP) indicate the length of an overlap (thin bars $< 1000\,\mathrm{yr}$, thick bars $\geq 1000\,\mathrm{yr}$), yellow bars the total energy supplied (see Fig. 2). The black horizontal line represents our energy constraint, see text for details. Roman numbers indicate terminations. 'A' and 'B' refer to Event A and B, respectively (see text for details).

Figure 5 The 'negative' insolation canon with its overlaps of the last 2 Myr and corresponding energy (energy only shown if overlap is equal to or longer than 1000 yr). In analogy to the 'positive' insolation canon (see Fig. caption 2 for details), total energy during insolation decrease was calculated as the integrated area between insolation curves and twice the value of the average insolation during the last 2 Myr. This seemingly arbitrary baseline was chosen to ensure comparability with energy values of the 'positive' insolation canon. The resulting energy can be pictured as a mirror image of the energy increase and is representative for the total energy decrease of the 'negative' insolation canon. Blue bars in **A)** (0-1 Myr BP) and **B)** (1-2 Myr BP) indicate the length of an overlap (thin bars $< 1000\,\mathrm{yr}$, thick bars $\geq 1000\,\mathrm{yr}$), yellow bars represent a measure for the total energy decrease. The black horizontal line illustrates our energy constraint.

Table 1: Comparison between results from this study and various deep-sea records [a]

	Termination (kyr BP)							
Author	I	II	III	IV	V	VI	VII	Method
This work, OT	23.1	139.1	253.3	345.4	418.6	546.2	632.3	1
RAYMO			247.9	339.3	423.6	534.5	621.6	2
L & R	14	130	243	337	424	533	621	3
H & W	11	129	239	332	419	532	623	4
SPECMAP	11	128	244	337	423	531	621	5
	Δt_{OT-MT} (kyr)							
	11.1	10.1	9.8	9.0		13.6	10.7	
	Δt_{Term} (kyr)							
This work		116	114	92	73	128	86	
RAYMO				91	84	111	87	
L & R		116	113	91	87	109	88	
H & W		118	110	93	87	113	91	
SPECMAP		117	116	93	86	108	90	

[a] OT refers to the Onset of Termination obtained in our analysis in kyr BP. For comparison the midpoints of termination (kyr BP) determined by Raymo (Raymo, 1997) (RAYMO), Lisiecki & Raymo (Lisiecki and Raymo, 2005) (L & R), Huybers & Wunsch (Huybers and Wunsch, 2004) (H & W) and Imbrie et al. (Imbrie et al., 1984) (SPECMAP) are shown. Additionally, the offset in kyr between our calculated OTs and the mean of the midpoints of termination (MT) are tabulated (Δt_{OT-MT}). Δt_{Term} values denote the time interval between two terminations in kyr. Methods applied are: mathematical analysis, this work (1), depth-derived with constant accumulation rate assumed (2), automated graphic correlation algorithm (3), depth-derived with sedimentation model (4), orbitally tuned (5).

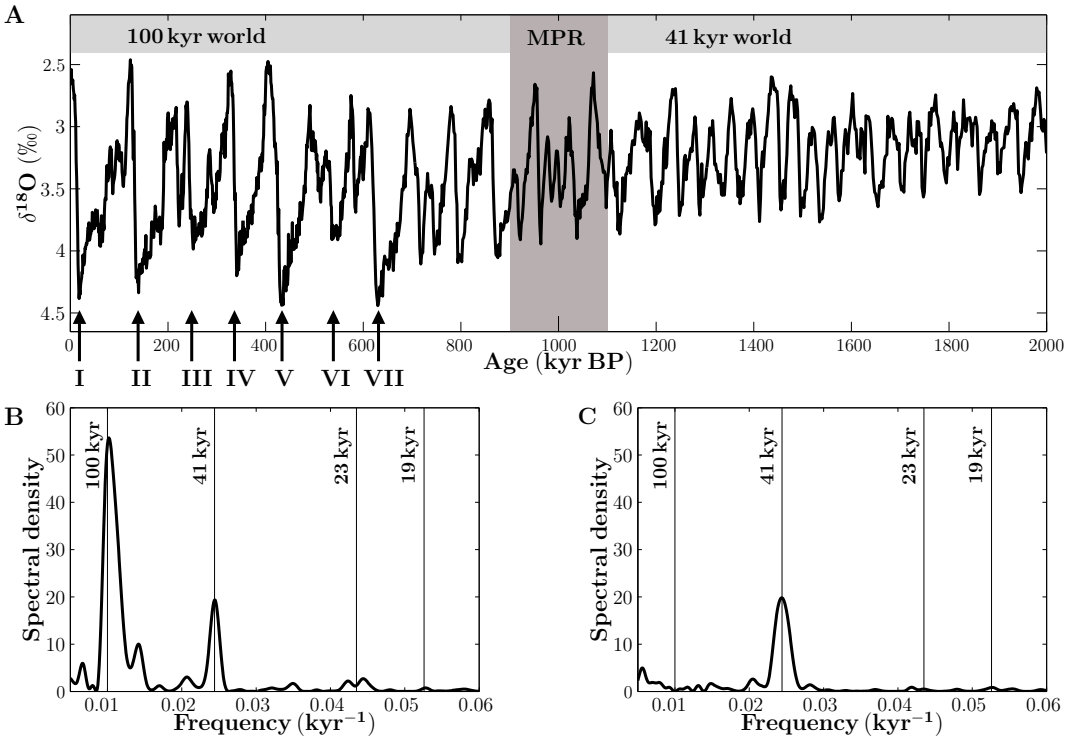
A
100 kyr world
MPR
41 kyr world
δ^{18}O (‰)
Age (kyr BP)
I II III IV V VI VII
B
C
Spectral density
100 kyr
41 kyr
23 kyr
19 kyr
Frequency (kyr^{-1})

Figure 1

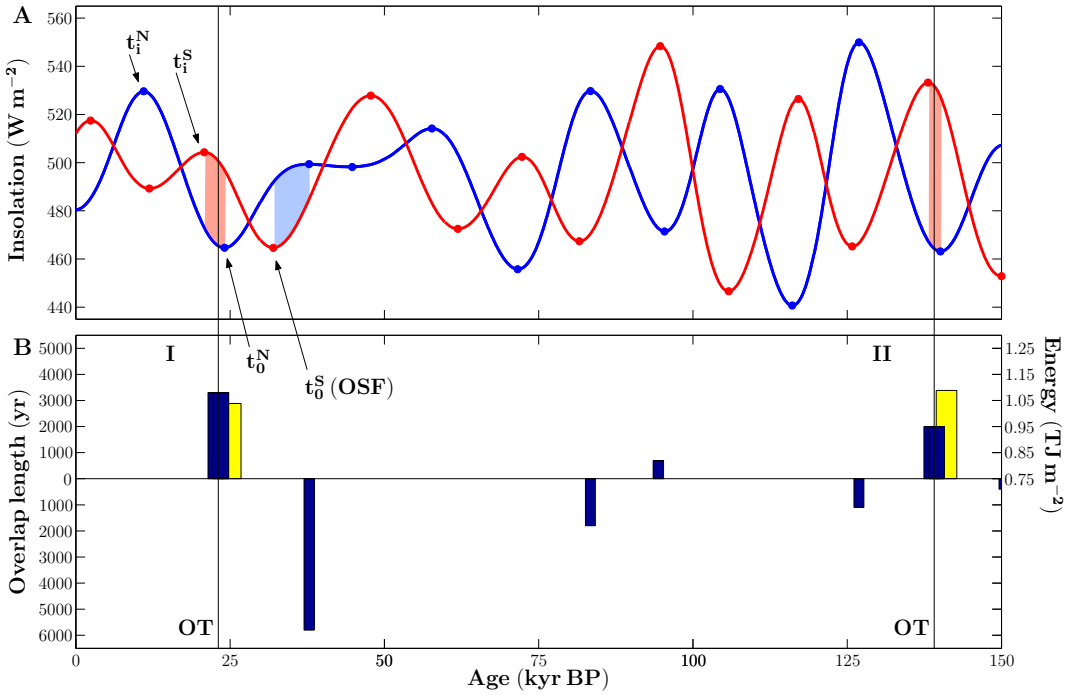
A
B
Insolation (W m^{-2})
Overlap length (yr)
Energy (TJ m^{-2})
Age (kyr BP)
t_i^N
t_i^S
t_0^N
t_0^S (OSF)
I
II
OT
OT

Figure 2

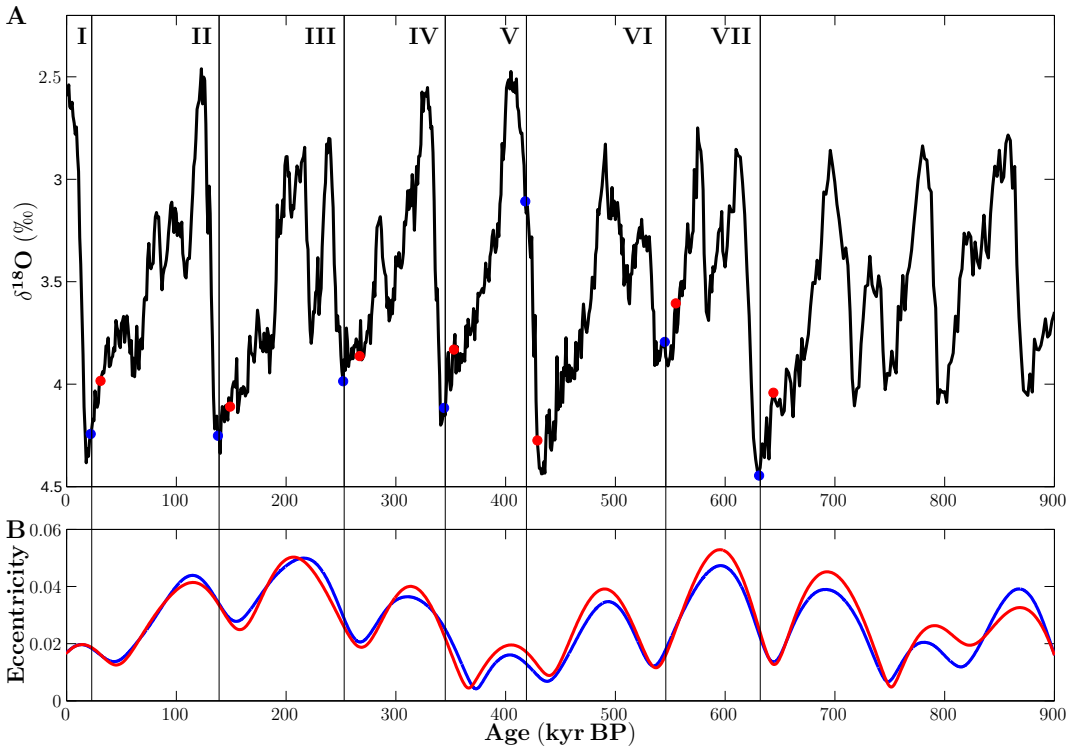
A
I
II
III
IV
V
VI
VII
2.5
3
3.5
4
4.5
δ^{18}O (‰)
0
100
200
300
400
500
600
700
800
900
B
0.06
0.04
0.02
0
Eccentricity
Age (kyr BP)

Figure 3

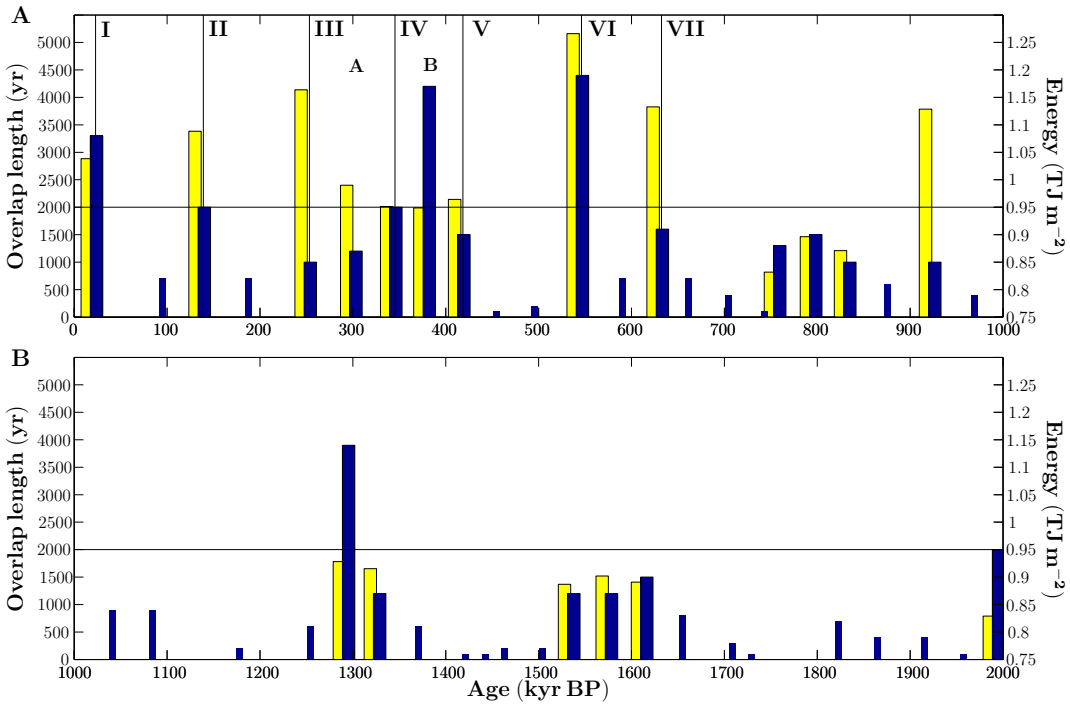
A
I
II
III
IV
V
VI
VII
A
B
Overlap length (yr)
Energy (TJ m^{-2})
B
Overlap length (yr)
Energy (TJ m^{-2})
Age (kyr BP)

Figure 4

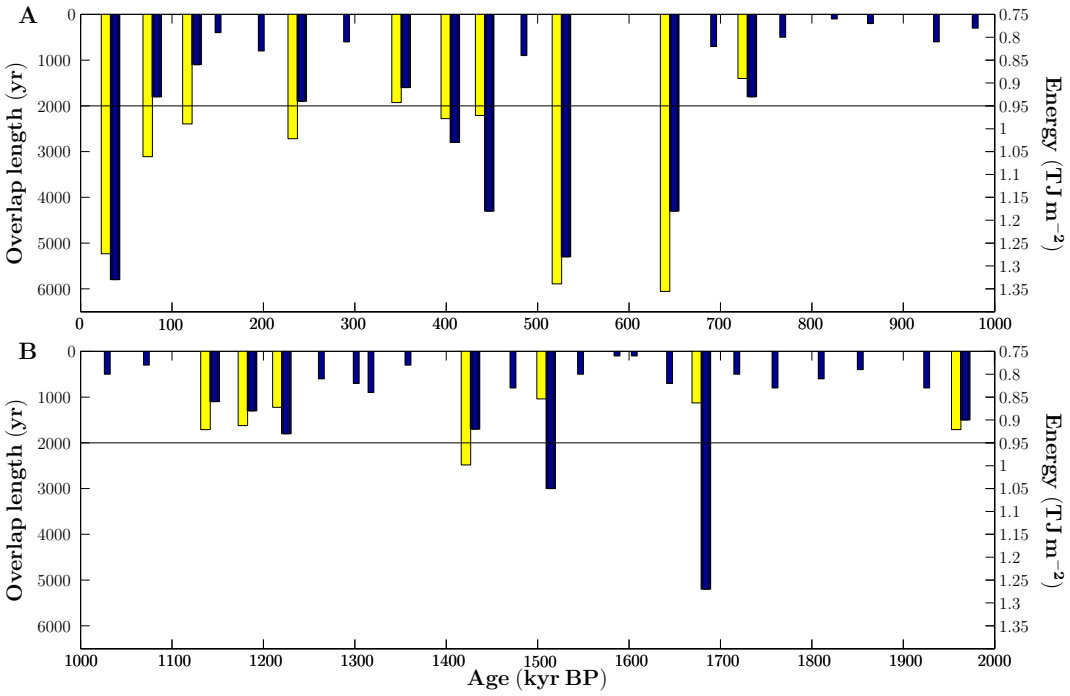
A
B
Overlap length (yr)
Energy (TJ m^{-2})
Age (kyr BP)
0
1000
2000
3000
4000
5000
6000
0.75
0.8
0.85
0.9
0.95
1
1.05
1.1
1.15
1.2
1.25
1.3
1.35
0
100
200
300
400
500
600
700
800
900
1000
1100
1200
1300
1400
1500
1600
1700
1800
1900
2000

Figure 5

irregular in shape, and lack the features characteristic of the AHT starches (Fig. 2f, g).

It is also clear that using specific grain types together with attribute combinations in a multiple grain analysis is an effective and perhaps the most conservative means to distinguish individual genera and species. Such an approach employs all the morphological characteristics that account for the population of starches in a single species as well as their quantitative frequency tendencies, and it takes into account intra- and interspecific variation in grain attributes. For example, starch grain populations from *T. dicoccoides* contain high proportions (about 40%) of grains that have distinctive, large crater-like impressions on the surface; these grains are also without lamellae (Fig. 2a). These types were not observed in either *Hordeum* or *Aegilops*, which, in turn contributed high frequencies of other types of characteristic starch grains (Fig. 2b–e and Supplementary Figs 1–4). In archaeological starch grain assemblages of sufficient sample sizes it would be possible to identify the presence and/or probable absence or low frequency of individual genera and species using these kinds of signatures.

Other families and species represented through their carbonized remains at Ohalo II were: Asteraceae (*Centaurea pallescens* Delile, *Silybum marianum* (L.) Gaertner), Chenopodiaceae (*Atriplex halimus* L., *Suaeda aegyptiaca* (Hasselquist) Zohary), Fabaceae (*Melilotus indicus* (L.) Allioni, *Pisum elatius* Marschall von Bieberstein), Malvaceae (*Malva aegyptia* L.), Potamogetonaceae (*Potamogeton pectinatus* L., *Potamogeton perfoliatus* L.), Ruppiaceae (*Ruppia maritima* L.) and Zygophyllaceae (*Nitraria schoberi* L.). Most of these species produced oils and not starches. The taxa with starches (*Pisum, Potamogeton* and *Ruppia*) have grains that can be distinguished from others in our and other established reference collections (Supplementary Figs 5–7).

Received 4 May; accepted 4 June 2004; doi:10.1038/nature02734.

1. Zohary, D. & Hopf, M. *Domestication of Plants in the Old World*, 3rd edn (Oxford Science Publications, Oxford, 2000).
2. Nadel, D. *Ohalo II—A 23,000-Year-Old Fisher-Hunter-Gatherers' Camp on the Shore of the Sea of Galilee* (Catalogue No. 20, Hecht Museum, Univ. Haifa, Haifa, 2002).
3. Nadel, D. & Werker, E. The oldest ever brush hut plant remains from Ohalo II, Jordan Valley, Israel. *Antiquity* **73,** 755–764 (1999).
4. Nadel, D., Carmi, I. & Segal, D. Radiocarbon dating of Ohalo II: Archaeological and methodological implications. *J. Archaeol. Sci.* **22,** 811–822 (1995).
5. Kislev, M. E., Nadel, D. & Carmi, I. Epipaleolithic (19,000 BP) cereal and fruit diet at Ohalo II, Sea of Galilee, Israel. *Rev. Palaeobot. Palynol.* **73,** 161–166 (1992).
6. Weiss, E., Kislev, M. E., Simchoni, O. & Nadel, D. Small-grained wild grasses as staple foods at the 23,000 year old site of Ohalo II, Israel. *Econ. Bot.* (in the press).
7. Piperno, D. R., Ranere, A. J., Holst, I. & Hansell, P. Starch grains reveal early root crop horticulture in the Panamanian tropical forest. *Nature* **407,** 894–897 (2000).
8. Pearsall, D. M., Chandler-Ezell, K. & Zeidler, J. A. Maize in ancient Ecuador: Results of residue analysis of stone tools from the Real Alto site. *J. Archaeol. Sci.* **31,** 423–442 (2004).
9. Palmer, C. Milk and cereals; identifying food and food identity among Fellahin and Bedouin in Jordan. *Levant* **34,** 173–195 (2002).
10. Hobbs, J. J. *Bedouin Life in the Egyptian Wilderness* (Univ. of Texas Press, Austin, 1992).
11. Nicolaisem, J. *Ecology and Culture of the Pastoral Tuareg* (Copenhagen National Museum, Copenhagen, 1963).
12. Jenkins, D. J. A. *et al.* Glycemic index: overview of implications in health and disease. *Am. J. Clin. Nutr.* **76,** 266–273 (2002).
13. Foster-Powell, K., Holt, S. H. & Brand-Miller, J. C. International table of glycemic index and glycemic load values. *Am. J. Clin. Nutr.* **76,** 5–56 (2002).
14. Stahl, A. in *Foraging and Farming* (eds Harris, D. R. & Hillman, G. C.) 171–194 (Unwin Hyman, London, 1989).
15. Wright, K. Ground-Stone tools and hunter-gatherer subsistence in southwest Asia: Implications for the transition to farming. *Am. Antiq.* **59,** 238–263 (1994).
16. Kuhn, S. L. & Stiner, M. C. in *Hunter-Gatherers: An Interdisciplinary Perspective* (eds Painter-Brick, C., Layton, R. H. & Rowley-Conwy, P.) 99–142 (Cambridge Univ. Press, Cambridge, 2001).
17. Bar-Yosef, O. & Kislev, M. E. in *Foraging and Farming: The Evolution of Plant Exploitation* (eds Harris, D. R. & Hillman, G. C.) 633–642 (Unwin Hyman, London, 1989).
18. Flannery, K. V. in *The Domestication and Exploitation of Plants and Animals* (eds Ucko, P. J. & Dimbleby, G. W.) 73–100 (Duckworth, London, 1969).
19. Hawkes, K., O'Connell, J. F. & Rogers, L. The behavioral ecology of modern hunter-gatherers, and human evolution. *Trends Ecol. Evol.* **12,** 29–32 (1997).
20. Kennett, D. & Winterhalder, B. in *Foraging Theory and the Transition to Agriculture* (eds Kennett, D. & Winterhalder, B.) (Smithsonian Institution Press, Washington DC, in the press).
21. Weiss, E., Wetterstrom, W., Nadel, D. & Bar-Yosef, O. The broad spectrum revolution revisited: Evidence from plant remains. *Proc. Natl Acad. Sci. USA* **101,** 9551–9555 (2004).
22. Bar-Yosef, O. From sedentary foragers to village hierarchies: The emergence of social institutions. *Proc. Br. Acad.* **110,** 1–38 (2001).
23. Reichert, E. T. *The Differentiation and Specificity of Starches in Relation to Genera, Species, Etc.* (Carnegie Institution of Washington, Washington DC, 1913).
24. Seidemann, J. *Starke Atlas* (Paul Parey, Berlin, 1966).
25. Cortello, A. R. & Pochettino, M. L. Starch grain analysis as a microscopic identification feature in the identification of plant material. *Econ. Bot.* **48,** 171–181 (1994).
26. Perry, L. Starch analyses reveal the multiple functions of quartz 'manioc' grater flakes from the Orinoco Basin, Venezuela. *Interciencia* **27,** 635–639 (2002).
27. Piperno, D. R. & Holst, I. The presence of starch grains on prehistoric stone tools from the lowland Neotropics: Indications of early tuber use and agriculture in Panama. *J. Archaeol. Sci.* **25,** 765–776 (1998).
28. Torrence, R., Wright, R. & Conway, R. Identification of starch granules using image analysis and multivariate techniques. *J. Archaeol. Sci.* **31,** 519–532 (2004).

Supplementary Information accompanies the paper on **www.nature.com/nature**.

Acknowledgements Supported by the Smithsonian Tropical Research Institute (STRI), a grant to the STRI from the Andrew W. Mellon Foundation, the American School of Prehistoric Research (Peabody Museum), Harvard University and the National Museum of Natural History. We acknowledge the help of the following people and institutions for supplying the seed reference collection used in this study: E. Wood and D. Pfister (Harvard University Herbarium), the United States National Plant Germplasm System (North Central Regional Plant Introduction Station, Western Regional Plant Introduction Station and Plant Genetic Resources Conservation Unit), and the Royal Botanic Gardens, Kew (Seed Conservation Department). The Ohalo II project was supported by the Irene-Levi Sala CARE Archaeological project Foundation, the Israel Academy of Science, the Jerusalem Center for Anthropological Studies, the L.S.B. Leakey Foundation, the M. Stekelis Museum of Prehistory in Haifa, the MAFCAF Foundation, the National Geographic Society and the Israel Antiquities Authority.

Competing interests statement The authors declare that they have no competing financial interests.

Correspondence and requests for materials should be addressed to D.R.P. (pipernod@tivoli.si.edu) and E.W. (eweiss@fas.harvard.edu).

Effect of trace metal availability on coccolithophorid calcification

K. G. Schulz[1,2], I. Zondervan[1], L. J. A. Gerringa[3], K. R. Timmermans[3], M. J. W. Veldhuis[3] & U. Riebesell[1,2]

[1]*Alfred Wegener Institute for Polar and Marine Research, PO Box 120161, 27515 Bremerhaven, Germany*
[2]*Leibniz Institute for Marine Sciences (IFM-GEOMAR), Düsternbrooker Weg 20, 24105 Kiel, Germany*
[3]*Royal Netherlands Institute for Sea Research, PO Box 59, 1790 AB Den Burg, Texel, The Netherlands*

The deposition of atmospheric dust into the ocean has varied considerably over geological time[1,2]. Because some of the trace metals contained in dust are essential plant nutrients which can limit phytoplankton growth in parts of the ocean, it has been suggested that variations in dust supply to the surface ocean might influence primary production[3,4]. Whereas the role of trace metal availability in photosynthetic carbon fixation has received considerable attention, its effect on biogenic calcification is virtually unknown. The production of both particulate organic carbon and calcium carbonate ($CaCO_3$) drives the ocean's biological carbon pump. The ratio of particulate organic carbon to $CaCO_3$ export, the so-called rain ratio, is one of the factors determining CO_2 sequestration in the deep ocean. Here we investigate the influence of the essential trace metals iron and zinc on the prominent $CaCO_3$-producing microalga *Emiliania huxleyi*. We show that whereas at low iron concentrations growth and calcification are equally reduced, low zinc concentrations result in a de-coupling of the two processes. Despite the reduced growth rate of zinc-limited cells, $CaCO_3$ production rates per cell remain unaffected, thus leading to highly calcified cells. These results suggest that changes in dust deposition can affect biogenic calcification in oceanic regions characterized by trace metal limitation, with possible consequences for CO_2 partitioning between the atmosphere and the ocean.

The production of $CaCO_3$ in the surface ocean, its export to greater depths and its deposition in the sediment above the lysocline (the depth below which $CaCO_3$ dissolves) affect atmospheric CO_2 in two ways. On a timescale that is shorter than the ocean mixing time, $CaCO_3$ export reduces alkalinity in the surface ocean and lowers its storage capacity for atmospheric CO_2. On a timescale of thousands of years, a mechanism called carbonate compensation balances $CaCO_3$ burial with its supply of raw materials (riverine calcium and carbonate ions) by adjusting the depth of the lysocline[5]. This determines the deep ocean's carbonate ion concentration and

controls surface water carbonate chemistry and consequently atmospheric CO_2. On both timescales a reduction in $CaCO_3$ export lowers CO_2 concentrations in the atmosphere.

$CaCO_3$ is predominantly produced in the open ocean, to a large extent by coccolithophores[6]. These open-ocean areas are subject to strong changes in atmospheric trace metal deposition. The rates for both iron and zinc deposition are probably up to ten times lower in today's ocean compared with the glacial ocean (see ref. 1 and references therein for iron, and Fig. 1 for zinc). Today iron concentrations limit phytoplankton productivity in large parts of the ocean known as high nitrate low chlorophyll (HNLC) areas[7]. Outside these regions iron availability is generally sufficient for most primary producers; however, productivity is often limited by the macronutrient nitrogen[8]. Although the significance of open-ocean zinc limitation awaits further assessment, prevailing zinc concentrations have been found to limit phytoplankton growth[9], particularly that of coccolithophores[10].

To simulate open-ocean iron and zinc limitation and to examine their effect on biogenic calcification, the prominent $CaCO_3$ producer *E. huxleyi* was grown under well-defined trace metal conditions, using the trace metal chelator EDTA and varying additions of iron chloride ($FeCl_3$) or zinc chloride ($ZnCl_2$). Because *E. huxleyi* has the ability to substitute cobalt for zinc[11], cells were grown at low free cobalt concentrations ($[Co^{2+}]$) of about 0.2 pmol kg^{-1}, which are comparable to values found in open-ocean waters[12]. Furthermore, because marine biogenic calcification is sensitive to CO_2-related changes in seawater carbonate chemistry[13], which has varied in parallel with atmospheric trace metal deposition[1], incubations were carried out at different CO_2 concentrations.

The effect of iron on calcification was tested in incubations covering a range of calculated $[Fe(III)']$ (total dissolved inorganic iron(III) species) between 0.06–360 pmol kg^{-1}, at CO_2 concentrations of 20 and 7 μmol kg^{-1} (pH ~7.9 and ~8.35, respectively). The instantaneous growth rate decreased with decreasing $[Fe(III)']$ and was half-saturated at ~0.7 pmol kg^{-1} (Fig. 2a). Over the observed range neither the $CaCO_3$ content per cell (Fig. 2b) nor the cellular $CaCO_3$ to nitrogen ratio (Fig. 2d) changed significantly; however, the $CaCO_3$ production rate per cell decreased about sixfold with decreasing $[Fe(III)']$ (Fig. 2c), proportionally with the growth rate.

In a second experiment the effect of zinc on calcification was studied. Four different $[CO_2]$ of 30, 20, 13 and 7 μmol kg^{-1} (pH ~7.75, ~7.9, ~8.1 and ~8.35, respectively) were applied and the calculated free zinc concentration ($[Zn^{2+}]$) ranged from 0.3 to 6 pmol kg^{-1}. The instantaneous growth rate decreased with decreasing $[Zn^{2+}]$ and was half-saturated at ~0.5 pmol kg^{-1} (Fig. 3a), in close agreement with the previously determined value of ~0.6 pmol kg^{-1} (ref. 11). At the same time, the amount of $CaCO_3$ per cell increased from 10 to almost 60 pg with decreasing $[Zn^{2+}]$ (Fig. 3b). This was confirmed by scanning electron microscopy, which showed that cells of *E. huxleyi* were covered with multiple layers of calcite platelets (coccoliths) under zinc-depleted conditions, compared with 1–2 layers of coccoliths at high $[Zn^{2+}]$ (Fig. 4a and b, respectively). The ratio of cellular $CaCO_3$ to nitrogen increased more than twofold, from about four at high $[Zn^{2+}]$ to approximately nine at low $[Zn^{2+}]$ (Fig. 3d). In contrast, the $CaCO_3$ production rate per cell was hardly affected (Fig. 3c).

In the iron experiment, higher $CaCO_3$ contents and production rates per cell were observed at low $[CO_2]$, consistent with previous findings[14] (Fig. 2b, c). Owing to the massive zinc-related response of the cellular $CaCO_3$ content (Fig. 3b) and the comparatively high variability within and between CO_2 treatments, the relatively small effect of carbonate chemistry on calcification could not be detected in the zinc assay.

The observed differences in calcification between iron- and zinc-limited cells may reflect the different roles of the two micronutrients in cellular processes. Although zinc deficiency slows down cellular growth and nitrogen utilization rates, it does not significantly affect the rate of $CaCO_3$ production (Fig. 3c). The resulting de-coupling of growth and calcification causes $CaCO_3$ accumulation in slow-growing cells of *E. huxleyi* (Fig. 3b). This also leads to a steady increase in the cellular $CaCO_3$ to nitrogen ratio when changing from high to low $[Zn^{2+}]$ (Fig. 3d). On the contrary, iron depletion not only reduces growth and nitrogen utilization rates, but equally reduces the rate of cellular $CaCO_3$ production (Fig. 2c). Therefore, the cellular $CaCO_3$ to nitrogen ratio remains fairly constant with varying iron availability (Fig. 2d).

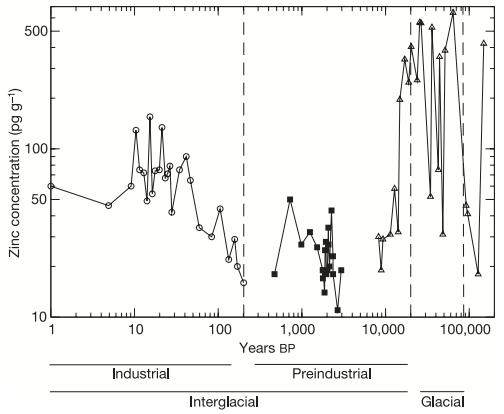

Figure 1 Zinc concentration in central Greenland snow and ice over the past 150,000 years. Data compiled from previous research: ref. 28, circles; ref. 29, squares; and ref. 30, triangles.

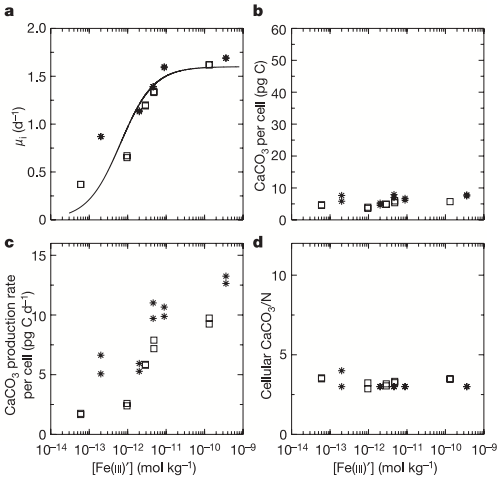

Figure 2 Response of *E. huxleyi* to varying free iron concentrations ($[Fe'(III)]$). Responses shown are instantaneous growth rate (μ_i) (**a**), $CaCO_3$ content per cell (**b**), the specific $CaCO_3$ production rate per cell and day (**c**) and the ratio of cellular $CaCO_3$ to nitrogen (**d**). The solid line in **a** was obtained by fitting the data nonlinearly to a modified Monod curve, which accounts for a cell's minimum free metal requirement. The squares and asterisks denote CO_2 concentrations of 20 and 7 μmol kg^{-1}, respectively.

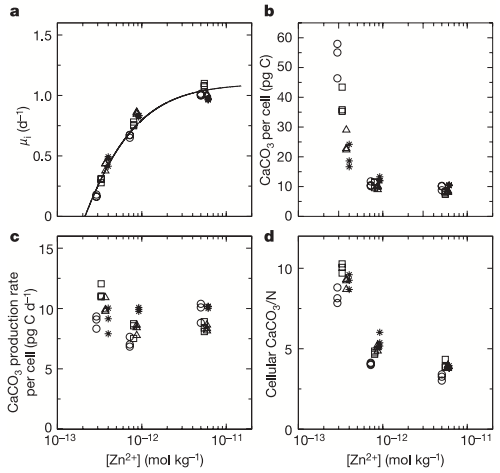

Figure 3 Response of *E. huxleyi* to varying free zinc concentrations ($[Zn^{2+}]$). **a**–**d**, As Fig. 2. The symbols denote four CO_2 concentrations as follows: circles, 30; squares, 20; triangles, 13; and asterisks, 7 μmol kg^{-1}. Note that the lower maximum growth rate in this experiment compared with the iron experiment (Fig. 2a) was due to the lack of the vitamin thiamine. A control experiment with thiamine added at selected $[Zn^{2+}]$ (data not shown) resulted in the same trends at higher μ_i.

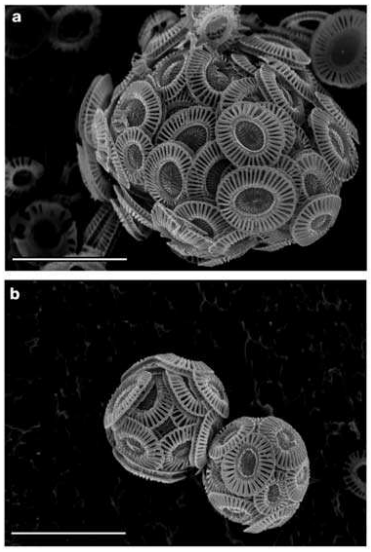

Figure 4 Scanning electron microscopy images of *E. huxleyi* grown under different free zinc and CO_2 concentrations. **a**, 0.3 pmol kg^{-1} $[Zn^{2+}]$ and 20 μmol kg^{-1} $[CO_2]$. **b**, 6 pmol kg^{-1} $[Zn^{2+}]$ and 13 μmol kg^{-1} $[CO_2]$. Scale bars, 5 μm. Note that the effect of CO_2 on calcification is minute compared with that of zinc. See text for details.

The biogeochemical relevance of the observed responses to iron and zinc limitation is likely to differ between oceanic regions. Increased atmospheric deposition of iron and zinc in the ocean's HNLC areas during glacial times has probably not significantly altered global $CaCO_3$ production. For reasons not fully understood, pelagic calcification is only of minor importance in these regions. In the largest HNLC region, the Southern Ocean, $CaCO_3$ production seems to be negligible[6]. This is also true for the equatorial Pacific, which is dominated by siliceous primary production, as is clearly reflected in the underlying sediments[15] above the lysocline. Only in the iron-deficient Pacific above 45° N does $CaCO_3$ production match that in the rest of the North Pacific[6]. As this area is comparatively small, however, its contribution to global calcification is bound to be low. Additionally, in HNLC areas diatoms have been shown to benefit most from iron or combined iron and zinc additions (see refs 9, 10 and references therein) by increasing nitrogen utilization and biomass production.

Outside the HNLC areas, export production is limited by the supply of macronutrients, primarily nitrate[8]. In many of these areas total dissolved zinc concentrations (see refs 16, 17 and references therein) are as low as those found in parts of the North Pacific[18], where coccolithophorid growth has been shown to be limited by zinc[10]. Considering that in the present ocean up to 450 μg m^{-2} dissolvable zinc is deposited atmospherically per year[19] compared with 1,000 μg m^{-2} zinc per year which is upwelled (taking a deep-ocean zinc concentration of 5.4 nmol kg^{-1} and a mean deep-surface water exchange volume of 3 m^3 m^{-2} per year[15]), a tenfold increase (Fig. 1) in atmospheric deposition can be expected to significantly alter surface ocean zinc concentrations. Moreover, Northern Hemisphere atmospheric zinc deposition in the recent pre-industrial period was probably one-half to one-third of that today, as indicated by zinc measurements taken in Arctic ice and snow (Fig. 1). Thus, regions in which growth of coccolithophores is potentially zinc-limited today probably experienced significant alleviation during glacial times.

There are two ways in which changes in zinc supply to the surface ocean by means of atmospheric dust deposition could alter global $CaCO_3$ production on glacial/interglacial timescales. On the one hand, results of a recent study[10] indicate that alleviation of zinc limitation may be accompanied by changes in the natural phytoplankton assemblages in favour of coccolithophores. This would lead to higher coccolithophorid-based biomass and potentially higher total $CaCO_3$ production at the community level. The results of this study, on the other hand, indicate that the amount of $CaCO_3$ that is precipitated in conjunction with a given amount of coccolithophorid biomass produced is expected to decrease with increasing surface-water zinc concentrations. On the basis of this effect, higher atmospheric zinc deposition during glacial periods would correspond to lower $CaCO_3$ production.

If coccolithophorid zinc limitation proves to be a general phenomenon in today's oceans, the observed processes may influence the strength of the ocean's $CaCO_3$ pump. Any change in its intensity directly affects the rain ratio, thereby altering carbon sequestration in the ocean. Long-term variation in atmospheric zinc deposition and its potential effect on biogenic calcification may therefore need to be considered in the context of glacial/interglacial changes in CO_2 partitioning between atmosphere and ocean. □

Methods

Experimental setup

Mono-specific cultures of *E. huxleyi* clone PML B92/11 were grown in triplicates (zinc experiment) or duplicates (iron experiment) at 15 °C in 0.2 μm filtered sea water, originating from the Gulf of Biscay (zinc experiment) and the Antarctic Ocean (iron experiment), at a photon flux density of 180 μmol m^{-2} s^{-1} (supplied from cool white fluorescent bulbs (Philips TLD 36W/54) on a 16/8-h light/dark cycle). Precultures and experimental incubations in dilute batch cultures ensured exponential growth throughout the experiment. The medium was enriched with nitrate and phosphate (64 and 4 μmol kg^{-1}, respectively), vitamin B12 (0.59 nmol kg^{-1}), biotin (0.2 nmol kg^{-1}) and 59 nmol kg^{-1} of thiamine-HCl (see Fig. 3 legend for details). Final trace metal concentrations were obtained by adding: $FeCl_3$ (1 μmol kg^{-1}) (zinc experiment), $ZnCl_2$ (1 μmol kg^{-1}) (iron experiment), $CuSO_4{\cdot}5H_2O$ (40 nmol kg^{-1}), $CoCl_2$ (10 nmol kg^{-1}), $MnCl_2{\cdot}4H_2O$ (450 nmol kg^{-1}), $(NH_4)_6Mo_7O_{24}{\cdot}4H_2O$ (1.43 nmol kg^{-1}), $Na_2SeO_3{\cdot}5H_2O$

($100\,nmol\,kg^{-1}$), KBr ($92\,\mu mol\,kg^{-1}$), $SrCl_2{\cdot}6H_2O$ ($13\,\mu mol\,kg^{-1}$), $AlCl_3$ ($100\,nmol\,kg^{-1}$), LiCl ($70\,nmol\,kg^{-1}$), KI ($60\,nmol\,kg^{-1}$), H_3BO_3 ($3.23\,\mu mol\,kg^{-1}$), RbCl ($250\,nmol\,kg^{-1}$). To achieve defined trace metal conditions for $[Zn^{2+}]$ or $[Fe(III)']$, $1\,mmol\,kg^{-1}$ of $Na_2EDTA{\cdot}6H_2O$ and varying amounts of $ZnCl_2$ or $FeCl_3$ were added to the media, which after pH adjustment with NaOH was stored for 24 h in the dark to allow chemical equilibration. In a control experiment at low, widely used culture media [EDTA] of $6\,\mu mol\,kg^{-1}$ the same maximum growth rates were observed, indicating that the comparatively high [EDTA] applied here did not have any detrimental effect on *E. huxleyi*.

Trace metal speciation

$[Zn^{2+}]$ and $[Fe(III)']$ were calculated from total metal concentrations using an equilibrium complexation model. Therefore, conditional stability constants for Fe(III) complexes with chlorine, fluoride, sulphate and the Fe(III) hydroxides (see refs 20, 21 and references therein) were included and, for the sake of consistency, thermodynamic stability constants[22] were used for all EDTA complexes with Fe, Cu, Co, Mn, Zn, Ca, Mg, the protonated forms of EDTA, and $ZnCO_3$ and $ZnSO_4$ after correction for ionic strength (salinity 34) with ion activity coefficients obtained either by Pitzer modelling[23] or Davies approximation. Light-induced photo-dissociation of Fe–EDTA complexes was accounted for following the model given in ref. 24. On the basis of this model two pH-dependent factors, linearly interpolated to 15 °C, were calculated and corrected for the lower photon-flux density and the light/dark cycle in our experiments (resulting in factors of 1.5 at pH 7.9 and 3 at pH 8.35). The absolute values for $[Fe(III)']$, however, crucially depend on the selected set of hydrolysis constants, particularly on β_3^*, which is so far not well constrained (see Table 2 in ref. 24 and references therein for details). The total zinc and iron concentrations in the natural sea water before nutrient addition were 7 and 1 $nmol\,kg^{-1}$, respectively and the $[Zn^{2+}]/[Zn_{total}]$ in the zinc experiments was about 1/75,000.

Sampling and measurements

The carbonate system was calculated from pH and total dissolved inorganic carbon using the dissociation constants of ref. 25 as refitted in ref. 26. The pH was measured using the recommendations of ref. 21 and the total dissolved inorganic carbon was measured using a photochemical approach[27]. To calculate growth rates, cell counts were obtained at the beginning and end of incubations on a Coulter Epics XL-MCL flowcytometer. For measurements of cellular particulate organic carbon (POC) and nitrogen (PON) and total particulate carbon (TPC), subsamples were filtered on precombusted (500 °C) Whatman GF/F filters at the end of the experiments and stored at −25 °C. Before analysis POC filters were fumed for 2 h with concentrated HCl. POC, PON and TPC were analysed on an ANCA-SL 20-20 Europa Scientific mass spectrometer after 2 h of drying the filters at 60 °C. $CaCO_3$ was calculated by subtracting POC from TPC. $CaCO_3$ production rates were calculated from growth rates and cellular $CaCO_3$ contents. Owing to the experimental approach used in this study (see above), these parameters did not change significantly over the course of the experiments.

Received 24 January; accepted 10 May 2004; doi:10.1038/nature02631.

1. Petit, J. R. *et al.* Climate and atmospheric history of the past 420,000 years from the Vostok ice core, Antarctica. *Nature* **399,** 429–436 (1999).
2. Mahowald, N. *et al.* Dust sources and deposition during the last glacial maximum and current climate: A comparison of model results with paleodata from ice cores and marine sediments. *J. Geophys. Res.* **104,** 15895–15916 (1999).
3. Martin, J. H. Glacial-interglacial CO_2 change: the iron hypothesis. *Paleoceanogr.* **5,** 1–13 (1990).
4. Morel, F. M. M. *et al.* Zinc and carbon co-limitation of marine phytoplankton. *Nature* **369,** 740–742 (1994).
5. Broecker, W. S. & Peng, T.-H. The role of $CaCO_3$ compensation in the glacial to interglacial atmospheric CO_2 change. *Glob. Biogeochem. Cycles* **1,** 15–29 (1987).
6. Milliman, J. D. Production and accumulation of calcium carbonate in the ocean: budget of a nonsteady state. *Glob. Biogeochem. Cycles* **7,** 927–957 (1993).
7. Baar de, H. J. W. & Boyd, P. W. in *The Changing Ocean Carbon Cycle* (eds Hanson, R. B., Ducklow, H. W. & Fields, J. G.) 61–140 (Cambridge Univ. Press, Cambridge, 2000).
8. Conkright, M. E., Levitus, S. & Boyer, T. P. *World Ocean Atlas 1994,* Vol. 1 *Nutrients* (NOAA Atlas NESDIS 1, US Department of Commerce, Washington DC, 1994).
9. Coale, K. H. Effects of iron, manganese, copper, and zinc enrichments on productivity and biomass in the subarctic Pacific. *Limnol. Oceanogr.* **36,** 1851–1864 (1991).
10. Crawford, D. W. *et al.* Influence of zinc and iron enrichments on phytoplankton growth in the northeastern subarctic Pacific. *Limnol. Oceanogr.* **48,** 1583–1600 (2003).
11. Sunda, W. G. & Huntsman, S. A. Cobalt and zinc interreplacement in marine phytoplankton: Biological and geochemical implications. *Limnol. Oceanogr.* **40,** 1404–1417 (1995).
12. Ellwood, M. J. & Van den Berg, C. M. G. Determination of organic complexation of cobalt in seawater by cathodic stripping voltammetry. *Mar. Chem.* **75,** 33–47 (2001).
13. Riebesell, U. *et al.* Reduced calcification of marine plankton in response to increased atmospheric CO_2. *Nature* **407,** 364–367 (2000).
14. Zondervan, I., Rost, B. & Riebesell, U. Effect of CO_2 concentration on the PIC/POC ratio in the coccolithophore *Emiliania huxleyi* grown under light-limiting conditions and different daylengths. *J. Exp. Mar. Biol. Ecol.* **272,** 55–70 (2002).
15. Broecker, W. S. & Peng, T.-H. *Tracers in the Sea* (Eldigio, New York, 1982).
16. Bruland, K. W. Complexation of zinc by natural organic ligands in the central North Pacific. *Limnol. Oceanogr.* **34,** 269–285 (1989).
17. Kremling, K. & Streu, P. The behaviour of dissolved Cd, Co, Zn and Pb in North Atlantic near-surface waters (30°N/60°W–60°N/2°W). *Deep-Sea Res. I* **48,** 2541–2567 (2001).
18. Lohan, M. C., Statham, P. J. & Crawford, D. W. Total dissolved zinc in the upper water column of the subarctic North East pacific. *Deep-Sea Res. II* **49,** 5793–5808 (2002).
19. Duce, R. *et al.* The atmospheric input of trace species to the world ocean. *Glob. Biogeochem. Cycles* **5,** 193–259 (1991).
20. Liu, X. & Millero, F. J. The solubility of iron in seawater. *Mar. Chem.* **77,** 43–54 (2002).
21. DOE. *Handbook of Methods for the Analysis of the Various Parameters of the Carbon Dioxide System in Seawater* (eds Dickson, A. G. & Goyet, C.) Version 2.1 ORNL/CDIAC-74 ⟨http://andrew.ucsd.edu/co2qc/handbook.html⟩ (1994).
22. Pettit, L. D. & Powell, K. J. *IUPAC Stability Constants Database* (IUPAC and Academic Software, Otley, 2001).
23. Millero, F. J. & Pierrot, D. A chemical equilibrium model for natural waters. *Aquat. Geochem.* **4,** 153–199 (1998).
24. Sunda, W. & Huntsman, S. Effect of pH, light, and temperature on Fe-EDTA chelation and Fe hydrolysis in seawater. *Mar. Chem.* **84,** 35–47 (2003).
25. Mehrbach, C., Culberson, C. H., Hawley, J. E. & Pytkowicz, R. N. Measurement of the apparent dissociation constants of carbonic acid in seawater at atmospheric pressure. *Limnol. Oceanogr.* **18,** 897–907 (1973).
26. Dickson, A. G. & Millero, F. J. A comparison of the equilibrium constants for the dissociation of carbonic acid in seawater media. *Deep-Sea Res.* **34,** 1733–1743 (1987).
27. Stoll, M. H. C., Bakker, K., Nobbe, G. H. & Haese, R. R. Continuous flow analysis of dissolved inorganic carbon content in seawater. *Anal. Chem.* **73,** 4111–4116 (2001).
28. Candelone, J.-P., Hong, S., Pellone, C. & Boutron, C. F. Post-Industrial Revolution changes in large-scale atmospheric pollution of the northern hemisphere by heavy metals as documented in central Greenland snow and ice. *J. Geophys. Res.* **100,** 16605–16616 (1995).
29. Hong, S., Candelone, J.-P. & Boutron, C. F. Changes in zinc and cadmium concentrations in Greenland ice during the past 7760 years. *Atmos. Environ.* **31,** 2235–2242 (1997).
30. Hong, S., Candelone, J.-P., Turetta, C. & Boutron, C. F. Changes in natural lead, copper, zinc and cadmium concentrations in central Greenland ice from 8250–149,100 years ago: their association with climate changes and resultant variations of dominant source contributions. *Earth Planet. Sci. Lett.* **143,** 233–244 (1996).

Acknowledgements We thank A. Terbrüggen, K.-U. Richter and B. van der Wagt for laboratory assistance, and M. Lohan, K. W. Bruland and R. E. Zeebe for discussions during the preparation of this manuscript. This work was partly funded by the German Research Foundation (DFG).

Competing interests statement The authors declare that they have no competing financial interests.

Correspondence and requests for materials should be addressed to K.G.S. (kschulz@ifm-geomar.de).

Aggression by polyembryonic wasp soldiers correlates with kinship but not resource competition

David Giron[1], Derek W. Dunn[2], Ian C. W. Hardy[2] & Michael R. Strand[1]

[1]*Department of Entomology, University of Georgia, Athens, Georgia 30602, USA*
[2]*School of Biosciences, University of Nottingham, Sutton Bonington Campus, Loughborough LE12 5RD, UK*

Kin selection theory predicts that individuals will show less aggression and more altruism towards relatives[1,2]. However, recent theoretical developments suggest that with limited dispersal, competition between relatives can override the effects of relatedness[3–9]. The predicted and opposing influences of relatedness and competition are difficult to approach experimentally because conditions that increase average relatedness among individuals also tend to increase competition. Polyembryonic wasps in the family Encyrtidae are parasites whose eggs undergo clonal division to produce large broods[10]. These insects have also evolved a caste system: some embryos in a clone develop into reproductive larvae that mature into adults, whereas others develop into sterile soldier larvae that defend siblings from competitors[11–14]. In a brood from a single egg, reproductive altruism by soldiers reflects clone-level allocation to defence at the cost of reproduction, with no conflict between individuals. When multiple eggs are laid into a host, inter-clone conflicts of interest arise. Here we report that soldier aggression in *Copidosoma floridanum* is inversely related to the genetic relatedness of competitors but shows no correlation with the level of resource competition.

Polyembryonic encyrtids are small (1 mm) parasitoid wasps that

ÖKOLOGIE

Der ozeanische Kalkregen

Auch im Ozean regnet es, und zwar Kalk. Dieser wird vor allem von mikroskopisch kleinen Kalkalgen in den oberen Wasserzonen gebildet und rieselt nach ihrem Absterben in die Tiefe. Da die Bildung von Kalk die Aufnahmefähigkeit der Ozeane für das Treibhausgas Kohlendioxid vermindert, wirkt sich die Aktivität der Kalkalgen auch auf das Klima aus. In vergangenen Eiszeiten war ihre Kalkbildung möglicherweise reduziert, was zu den damals verringerten Kohlendioxid-Konzentrationen in der Atmosphäre beigetragen haben könnte.

Unbeachtet von uns Menschen rieselt ein stetiger Kalkregen von der Licht durchfluteten Oberfläche der Ozeane auf die dunklen Gebirge der Tiefsee herab. Dafür sind vor allem mikroskopisch kleine, einzellige Kalkalgen (Coccolithophoriden) verantwortlich, die während ihres Wachstums in den oberen Wasserzonen bizarr anmutende Kalkstrukturen bilden. Bei Massenentwicklungen nimmt das Meer sogar eine milchige Färbung an, was selbst vom Weltraum aus zu sehen ist (Abb. 1). Nach dem Absterben der Algen regnet der Kalk ($CaCO_3$) dann in die Tiefe. Dieser Export von Kalk aus dem Oberflächenozean in die Tiefsee, wo er in Sedimenten abgelagert wird, ist von großem Interesse, reduziert er doch das Speichervermögen der Ozeane für das Treibhausgas Kohlendioxid (CO_2). Dies liegt an der Verschiebung des chemischen Gleichgewichtes von CO_2 im

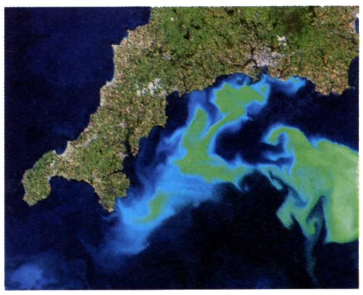

Abb. 1. Satellitenaufnahme (LANDSAT) vom 24. 7. 1999 eines Massenvorkommens von Kalkalgen vor der Küste Cornwalls, Südengland [Andrew Wilson, Steve Groom]

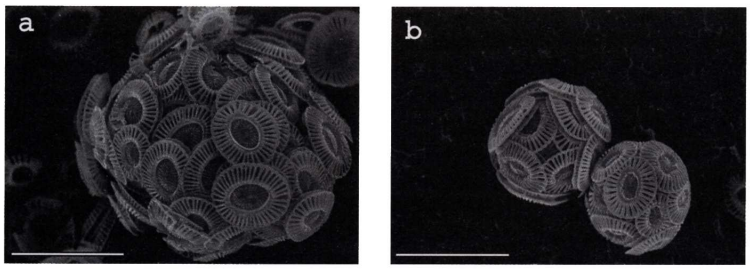

Abb. 2. Kalkalge *Emiliana huxleyi* gewachsen unter geringen (a) und hohen (b) Zinkkonzentrationen. Balken: 5 µm. Aus [2]

Meerwasser. Kohlendioxid reagiert mit Wasser und ist dort deshalb nicht nur in Form von CO_2, sondern auch als Hydrogencarbonat und Carbonat vorhanden:

$$CO_2 + H_2O \rightleftarrows HCO_3^- + H^+ \rightleftarrows CO_3^{2-} + H^+.$$

So liegen über 90% dieses gelösten, anorganischen Kohlenstoffs im heutigen Ozean als Hydrogencarbonat vor. Ist der CO_2-Partialdruck in den oberen Wasserzonen geringer als in der Atmosphäre, wird sich weiteres CO_2 aus der Atmosphäre im Wasser lösen, bis wieder ein Gleichgewicht hergestellt ist. Nur ein geringer Anteil des sich lösenden CO_2 wird dabei jedoch in dieser Form verbleiben, der weitaus größere Teil wird mit dem im Wasser vorhandenen Carbonat zu Hydrogencarbonat reagieren:

$$CO_2 + H_2O + CO_3^{2-} \rightleftarrows 2HCO_3^-.$$

Verständlicherweise wird der Ozean umso mehr CO_2 aus der Atmosphäre aufnehmen können, je höher die Konzentration von Carbonat im Meerwasser ist. Durch die Kalkbildung, also das Binden von CO_3^{2-} in $CaCO_3$ und die Ablagerung des Kalkes in Sedimenten der Tiefsee wird die Carbonatkonzentration in den oberen Meereszonen jedoch verringert. Je mehr Kalk im Ozean gebildet wird, desto geringer ist also dessen Aufnahmefähigkeit für atmosphärisches CO_2.

Zu geringeren CO_2-Konzentrationen in den oberen Wasserzonen im Vergleich zur Atmosphäre kommt es insbesondere durch den Aufbau und Export von organischer Biomasse. Diese wird im Meer von einzelligen Mikroalgen, vor allem Kieselalgen (Diatomeen), während ihres Wachstums durch CO_2-Fixierung in der Photosynthese gebildet. Dabei wird dem Meerwasser CO_2 entzogen und in organische Kohlenstoffverbindungen umgewandelt. Sinkt diese Biomasse nach dem Absterben der Algen in die Tiefe, bevor sie von bakteriellen Abbauprozessen wieder zu CO_2 veratmet werden kann, verringert dieser Export den CO_2-Partialdruck in den oberen Wasserschichten. Je mehr organische Biomasse und je weniger Kalk also exportiert werden, desto größer ist die CO_2-Aufnahmefähigkeit des Ozeans für atmosphärisches CO_2.

Algenwachstum und die damit verbundene Biomasseproduktion sind jedoch von der Verfügbarkeit von Nährstoffen abhängig. Neben Makronährstoffen (Nitrat und Phosphat) benötigen die Algen auch Mikronährstoffe, wie die Spurenmetalle Eisen und Zink. Diese sind in einigen Regionen des heutigen Ozeans jedoch in so geringen Konzentrationen vorhanden, dass sie das Algenwachstum und damit die Produktion organischer Biomasse einschränken. Eine solche Nährstofflimitation ist für Warmzeiten wie die heutige charakteristisch. In Eiszeiten hingegen dürfte aufgrund stärkerer Winde mehr Staub, der reich an Spurenmetallen ist, in die Ozeane geweht worden sein. Dies könnte zu einer gesteigerten Produktion organischer Biomasse und damit CO_2-Fixierung durch Algen geführt haben. Wenn dadurch mehr organischer Kohlenstoff in die Tiefe exportiert wurde, könnte dies zu den in Eiszeiten vergleichsweise niedrigen CO_2-Konzentrationen in der Atmosphäre beigetragen haben. In zahlreichen Studien, wie etwa den so genannten Eisendüngungsexperimenten im Südpolarmeer, wurde der positive Effekt von Spurenmetallen auf die CO_2-Fixierung von Diatomeen schon nachgewiesen [1]. Doch ob die Verfügbarkeit von Spurenmetallen auch die Kalkbildung von Coccolithophoriden beeinflussen kann, war bislang unbekannt. Meeresforscher vom Leibniz Institut für Meereswissenschaften (Kiel) widmeten sich zusammen mit Kollegen vom Alfred Wegener Institut für Polar- und Meeresforschung (Bremerhaven) und vom königlich niederländischen Institut für Meeresforschung (Texel) dieser Frage [2].

In Laborexperimenten mit der in allen Weltmeeren verbreiteten Coccolithophoride *Emiliania huxleyi* wurde der Einfluss von Eisen- und Zinkverfügbarkeit auf die Kalkbildung untersucht. In den Versuchen führten geringe Eisenkonzentrationen zwar zu reduzierten Wachstumsraten, die Algen bildeten aber unabhängig davon die gleichen Mengen an Kalk. Bei geringer Zinkverfügbarkeit hingegen waren zwar auch die Wachstumsraten niedriger, die Anzahl der Kalkplättchen pro Zelle stieg jedoch um ein Vielfaches an, verglichen mit höheren Zinkkonzentrationen (Abb. 2).

In einigen Regionen der Weltmeere ist das Wachstum von Coccolithophori-

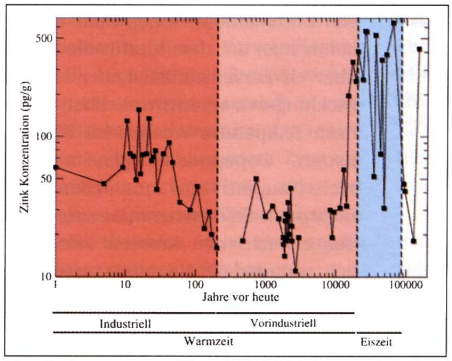

Abb. 3. Zinkkonzentration in arktischem Schnee und Eis der letzten 150 000 Jahre. Aus [2]

den durch geringe Zinkkonzentrationen eingeschränkt. Welche Auswirkungen könnte nun der vermehrte Eintrag von Staub und damit Zink in Eiszeiten (Abb. 3) auf ihre Kalkproduktion gehabt haben? Denkbar ist, dass die Gesamtkalkbildung verringert war, da pro Zelle weniger Kalk gebildet wurde. Dies hätte, weil auch weniger Kalk aus den oberen Meereszonen in die Tiefe exportiert worden wäre, die Speicherkapazität des Ozeans für CO_2 vergrößert und zu niedrigen CO_2-Konzentrationen in der Atmosphäre beigetragen, wie sie für Eiszeiten nachgewiesen sind. Es ist jedoch nicht auszuschließen, dass infolge höherer Wachstumsraten die Kalkalgen größere Zelldichten erreicht haben könnten als bei geringer Zinkverfügbarkeit. Da in diesem Fall zwar die einzelne Zelle weniger Kalk bildet, diese aber nun zahlreicher sind, ist es schwierig, mögliche Änderungen in der Gesamtkalkproduktion abzuschätzen. Eine endgültige Antwort auf die Frage, ob die Zinkverfügbarkeit die Intensität des Kalkregens beeinflusst, kann wohl nur in zukünftigen Feldstudien in Analogie zu den Eisendüngungsexperimenten gegeben werden.

Doch nicht nur das Klima mit seinen stärkeren oder schwächeren Winden besitzt das Potential, die Gesamtkalkbildung im Ozean zu verändern. Bohrkerne aus dem arktischen Eis zeigen, dass seit Beginn der Industrialisierung der Eintrag von Zink in die Meere deutlich gestiegen ist (Abb. 3). Dies wäre dann ein weiteres Beispiel dafür, wie der Mensch durch sein Handeln in komplexe Systeme unserer Erde unbewusst eingreift.

[1] H. J. W. de Baar, P. W. Boyd in: R. B. Hanson, H. W. Ducklow, J. G. Field (Hrsg): The Changing Ocean Carbon Cycle: A Midterm Synthesis of the Joint Global Ocean Flux Study. International Geosphere Biosphere Programme Book Series, Vol. 5., S. 61–140. Cambridge University Press. Cambridge, USA (2000). – [2] K. G. Schulz et al., Nature **430,** 673 (2004)

Kai Schulz, Dr. Ulf Riebesell, Kiel

Iron availability and the regulation of inorganic carbon acquisition in Emiliania huxleyi with respect to carbon isotope fractionation

K.G. Schulz[1], U. Riebesell[1], B. Rost[2], S. Thoms[2], D.A. Wolf-Gladrow[2]

[1]Leibniz Institute for Marine Sciences, Düsternbrooker Weg 20, 24105 Kiel, Germany

[2]Alfred Wegener Institute for Polar and Marine Research, P.O. Box 12016, 27515 Bremerhaven, Germany

To be submitted to *Limnology and Oceanography*

Abstract

Iron is one of the key elements limiting phytoplankton productivity in large parts of today's oceans, the so-called HNLC (high nitrate low chlorophyll) areas. Dissolved inorganic carbon (DIC) uptake during photosynthesis is generally enhanced by phytoplankton operating so-called carbon concentrating mechanisms (CCMs). Here we CCM regulation in the coccolithophorid *Emiliania huxleyi* in response to varying degrees of iron limitation by means of membrane-inlet mass spectrometry (MIMS). Compared to iron replete conditions rates of both CO_2 and HCO_3^- uptake were markedly reduced under iron limitation leading to significantly diminished growth rates. Moreover, there was a concomitant decrease in CCM activity, indicated by increased CO_2 loss from the cells in relation to total inorganic carbon uptake. Under such conditions higher values for carbon isotope fractionation (ϵ_p) would be expected. Surprisingly, however, direct measurements of ϵ_p showed that carbon isotope fractionation was insensitive to changes in growth rates and CCM activity. This can be explained by reduced rates of internal DIC circulation in and out the chloroplast, demonstrated with a simple cell model comprising two compartments. Furthermore, results of this model indicate that measured uptake rates for inorganic carbon are probably an order of magnitude lower compared to the cell's internal fluxes. This has to be kept in mind when relating carbon uptake rates to CCM activity. The insensitivity of carbon isotope fractionation to changes in the availability of iron could be of potential interest for paleoreconstructions in the HNLC areas of today's oceans.

Acknowledgements

to be added

Introduction

In large parts of the ocean, the so-called High Nutrients Low Chlorophyll (HNLC) areas, phytoplankton growth is limited by the availability of iron (Baar de and Boyd, 2000). The inability of phytoplankton to completely utilize the macronutrients present stems from the essential role of iron in photosynthesis, where it is integral part of photosystems I and II (PSI and PSII, respectively) and various cytochromes of the photosynthetic electron transport chain (Greene et al., 1991, 1992). Additionally, iron limitation induces the well known phenomenon of chlorosis, reduced levels of chlorophyll concentration within the chloroplast. Together, this yields reduced rates of photosynthetic oxygen evolution (Greene et al., 1991) and hence cellular growth rates of marine phytoplankton.

A significant portion of the photosynthetically generated reductive power (i.e. NADPH) and energy (i.e. ATP) is used to reduce and assimilate inorganic carbon (Falkowski and Raven, 1997). Additionally, most species invest considerable amounts of energy for inorganic carbon acquisition by operating so-called carbon concentrating mechanisms (CCMs) to increase CO_2 concentrations at the site of carboxylation (Raven and Lucas, 1985; Badger et al., 1998). The reason for employing such energy consuming processes, such as active uptake of CO_2 and/or HCO_3^-, rests on the comparatively low affinity of the main carboxylating enzyme RubisCO (Ribulose-1,5-bisphosphate carboxylase/oxygenase) for its substrate CO_2, a slow maximum turnover rate and its susceptibility for a competing reaction with O_2 (Badger et al., 1998). Thus, increasing [CO_2] at the site of RubisCO activity allows for higher carbon fixation and hence cellular growth rates.

Clearly, the availability of inorganic carbon and the cellular demand can change depending on environmental conditions. Thus, CCM activity is influenced by various abiotic factors such as [CO_2] (Burkhardt et al., 2001; Rost et al., 2003), light (Beardall, 1991; Rost et al., 2006) and temperature (Davison, 1987). CCM regulation allows phytoplankton to actively match the supply with their demand, optimizing energy and resource allocation efficiencies. Finally, CCM activity is reflected in the carbon isotopic composition of the

organic matter built up during photosynthesis, depending on the ratio of CO_2 to HCO_3^- utilized and the portion of inorganic carbon taken up which is not fixed by RubisCO but escapes the cell, called leakage (Sharkey and Berry, 1985; Laws et al., 2002; Raven et al., 2002).

Here we investigate the role of iron availability for inorganic carbon acquisition, certain parameters of CCM activity and stable carbon isotope fractionation in the coccolithophore *Emiliania huxleyi*.

Methods

Experimental setup

Mono-specific cultures of *Emiliania huxleyi* clone PML B92/11 were grown in duplicate at $15°C$ in 0.2 μm filtered Antarctic seawater (salinity of 31) at a photon flux density (PFD) of 180 $\mu mol\,m^{-2}\,s^{-1}$, supplied from cool white fluorescent bulbs (Philips TLD 36W/54) on a 16/8 light/dark cycle. The growth medium was enriched with nitrate and phosphate (64 and 4 $\mu mol\,kg^{-1}$, respectively), the vitamins B12, biotine and thiamine-HCl (0.59, 9.2 and 59 $nmol\,kg^{-1}$, respectively) and a metal mix (excluding iron) described in Schulz et al. (2004). Final [Fe(III)'] (total dissolved inorganic iron(III) species) were achieved by addition of 1.2 $mmol\,kg^{-1}$ of $Na_2EDTA \cdot 6H_2O$ and varying amounts of $FeCl_3$ (2000, 8 and 0 $nmol\,kg^{-1}$, referred to hereafter as iron replete, intermediate and deplete) to the media, which after adjustment to a pH_F (pH determined on the free scale) of about 8.0 with NaOH was stored for 24h in the dark to allow chemical equilibration. Precultures and experimental incubations in dilute batch cultures ensured exponential growth throughout the experiment.

Investigation of photosynthetic oxygen evolution and inorganic carbon fluxes were performed in a thermostated cuvette attached to a sectorfield multicollector mass spectrometer (Isoprime; GV Instruments England) via a gas permeable membrane (0.01mm PTFE) inlet system at an incident PFD of 300 $\mu mol\,m^{-2}\,s^{-1}$.

For measurements at the end of incubations, cells were concentrated by centrifugation at $450 \times \mathrm{g}$ and $15°\mathrm{C}$ for 10 minutes. After the measurements subsamples were taken for chlorophyll *a* (Chl *a*) and cell density determination. Chl *a* was measured spectrophotometrically as described by Strickland and Parsons (1968). Cell counts were obtained on a BD FacsCalibur flowcytometer and growth rates calculated from counts taken at the beginning and end of incubations.

Determination of net photosynthesis and inorganic carbon fluxes

In principle, investigation of photosynthetic oxygen evolution and inorganic carbon fluxes during steady-state photosynthesis followed the method and equations described by Badger et al. (1994). It is based on simultaneous measurement of $[\mathrm{CO_2}]$ and $[\mathrm{O_2}]$ during consecutive light (7 min.) and dark (7 min.) cycles in an initially DIC free assay buffer (seawater buffered with 50 mM HEPES at $\mathrm{pH_T} \sim 7.9$ at $15.5°\mathrm{C}$). The MIMS was calibrated for $\mathrm{CO_2}$ by injections of known amounts of $\mathrm{NaH^{12}CO_3}$ and $\mathrm{NaHC^{13}CO_3}$ into 8 ml of 0.2 M HCl (from here on, carbon species without $^{13}\mathrm{C}$ or $^{12}\mathrm{C}$ notation will refer to the sum of both). The $\mathrm{CO_2}$ baseline was determined by addition of 20 $\mu\mathrm{l}$ 10 M NaOH. Calibration for $\mathrm{O_2}$ was achieved by measuring an air saturated (21% $\mathrm{O_2}$), for which $[\mathrm{O_2}]$ was calculated according to Garcia and Gordon (1992), and an oxygen free assay buffer sample. The measured $[\mathrm{O_2}]$ were corrected for the $\mathrm{O_2}$ consumption by the MIMS which was determined by following the oxygen evolution in an initially air saturated assay buffer for approximately 1 hour and deriving a linear relation between $[\mathrm{O_2}]$ and $\mathrm{dO_2/dt}$. In contrast, $\mathrm{CO_2}$ consumption is negligible. The simultaneously recorded argon signal, which is not affected by biological activities, was used to correct for periodical signal fluctuations and smooth the oxygen, and in some cases, the carbon dioxide recordings.

$\mathrm{CO_2}$ and $\mathrm{HCO_3^-}$ fluxes during steady state photosynthesis have to be deduced from measurements of $\mathrm{O_2}$ and $\mathrm{CO_2}$ evolution during consecutive dark/light cycles (Fig. 1) at

increasing [DIC], making use of the chemical disequilibrium in the carbonate system created. For that purpose, the organisms of interest are incubated in the assay buffer in the presence of an inhibitor for extracellular carbonic anhydrase (dextran-bound sulfonamide, DBS). This blocks the otherwise rapid inter-conversion between CO_2 and HCO_3^- mediated by CA and allows establishing of a chemical disequilibrium. Calculations of the net fixation rates of carbon, the rates of respiration in the dark (in terms of carbon) and the total amount of carbon fixed then follow as

$$\mathrm{NetFix_{rate}} = \left(\frac{\mathrm{dO_2}}{\mathrm{dt}}\mathrm{L}\right)/\mathrm{PQ} \tag{1}$$

with PQ being the photosynthetic quotient assumed to be 1.1 and $\frac{\mathrm{dO_2}}{\mathrm{dt}}\mathrm{L}$ the temporal oxygen evolution at the end of the light phase (Fig. 1). Respiration rates in the dark are

$$\mathrm{Resp_{rate}} = -\left(\frac{\mathrm{dO_2}}{\mathrm{dt}}\mathrm{D}\right)/\mathrm{RQ} \tag{2}$$

with RQ being the respiratory quotient (assumed to be 1). $\frac{\mathrm{dO_2}}{\mathrm{dt}}\mathrm{D}$ denotes the temporal oxygen evolution at the end of the dark (Fig. 1). The amount of net inorganic carbon fixation during a certain period of time (t) in the light is

$$\mathrm{NetFix_{amount}} = (\Delta \mathrm{O_2})/\mathrm{PQ} \tag{3}$$

Considering net CO_2 uptake, it is necessary to account for the chemical disequilibrium in the carbonate system caused by the inorganic carbon uptake and release during photosynthesis and respiration, respectively. For that purpose, $[CO_2]$ and $[HCO_3^-]$ at the end of the light phase have to be known. However, of all three carbon species, only CO_2 can be monitored with the MIMS. Therefore, $[HCO_3^-]$ has to be deduced in the following manner. The respiration rate in the dark, calculated according to Eq. 2, can equally be expressed in terms of the temporal change in $[CO_2]$ in the dark when accounting for the chemical disequilibrium as

$$\mathrm{Resp_{rate}} = \frac{\mathrm{dCO_2}}{\mathrm{dt}}\mathrm{D1} + k_+[\mathrm{CO_2}]_{\mathrm{BL}} - k_-[\mathrm{HCO_3^-}]_{\mathrm{BL}} \tag{4}$$

with k_+ and k_- being the rate constants for the CO_2 to HCO_3^- inter-conversion, calculated according to Schulz et al. (2005). $\frac{dCO_2}{dt}D1$ denotes the temporal CO_2 evolution at the end of the dark phase, and $[CO_2]_{BL}$ and $[HCO_3^-]_{BL}$ the respective [CO_2] and [HCO_3^-] before the light phase (Fig 1). Solving for $[HCO_3^-]_{BL}$ yields

$$[HCO_3^-]_{BL} = \left(\frac{dCO_2}{dt}D1 + k_+[CO_2] - Resp_{rate}\right)/k_- \quad (5)$$

For assessment of [DIC] before the light $CO_3^{2-}$is described as a constant fraction of the HCO_3^- pool (with $f = CO_3^{2-}/HCO_3^-$). This is justified as there is no chemical disequilibrium between HCO_3^- and CO_3^{2-} on the timescale of seconds, owing to the relatively rapid inter-conversion rates between them (for details see Schulz et al. (2005)). The factor f was determined together with the CO_2 calibration of the MIMS. It involves calculation of the carbonate system from the ratio of known additions of DIC to measured CO_2 in the assay buffer using the dissociation constants of Mehrbach et al. (1973) as refitted by Dickson and Millero (1987). [DIC] before the light period is then given as

$$[DIC]_{BL} = [CO_2]_{BL} + [HCO_3^-]_{BL} + f[HCO_3^-]_{BL} \quad (6)$$

It follows that the [DIC] at the end of the light period is then determined by $[DIC]_{BL}$ and the amount of net inorganic carbon fixation during photosynthesis.

$$[DIC]_{EL} = [DIC]_{BL} - NetFix_{amount} \quad (7)$$

If calcifying organisms such as coccolithophores are investigated, Eq. 7 can be extended to account for the light dependent inorganic carbon uptake used in calcification. In coccolithophores there is good evidence that the inorganic carbon incorporated into calcium carbonate ($CaCO_3$) enters the cell in the form of HCO_3^- (Paasche, 2001; Berry et al., 2002). Application of the particulate inorganic carbon (PIC) to particulate organic carbon (POC) ratio allows to express calcification in terms of net carbon fixation during photosynthesis. However, while the amount of PIC produced in the light remains unaltered in the dark phase, some of the POC will be respired. Therefore, measured PIC/POC (see end of next section

for details) have to be corrected for respiratory loss of POC in the dark. Given a 16/8 hour light/dark cycle, the PIC to POC production rate in the light is therefore

$$\frac{\mathrm{PIC}}{\mathrm{POC}}\mathrm{L} = \frac{16\,\mathrm{NetFix_{rate}} - 8\,\mathrm{Resp_{rate}}}{16\,\mathrm{NetFix_{rate}}} \times \frac{\mathrm{PIC}}{\mathrm{POC}} \tag{8}$$

Calculated values for PIC/POC in the light were 0.48, 0.43 and 0.38 for iron replete, intermediate and replete conditions, respectively. Hence, it follows that

$$\mathrm{Calc_{amount}} = \mathrm{NetFix_{amount}}\mathrm{PIC/POC_L} \tag{9}$$

To account for calcification, calculated values are then subtracted from $[\mathrm{DIC}]_{\mathrm{EL}}$. It should be noted that an inherent assumption in this approach is that the half-saturation constants for net carbon fixation and calcification are the same. Finally, the $[\mathrm{HCO_3^-}]$ at the end of the light period is given by

$$[\mathrm{HCO_3^-}]_{\mathrm{EL}} = ([\mathrm{DIC}]_{\mathrm{EL}} - [\mathrm{CO_2}]_{\mathrm{EL}})/(1+\mathrm{f}) \tag{10}$$

Having derived $[\mathrm{HCO_3^-}]$ at the end of the light period allows calculation of the net $\mathrm{CO_2}$ uptake rate as

$$\mathrm{NetCO_2up_{rate}} = -\frac{\mathrm{dCO_2}}{\mathrm{dt}}\mathrm{L} - k_-[\mathrm{HCO_3^-}]_{\mathrm{EL}} + k_+[\mathrm{CO_2}]_{\mathrm{EL}} \tag{11}$$

The portion of net carbon fixation which can not be explained by $\mathrm{CO_2}$ uptake must then have other inorganic carbon sources. Assuming that $\mathrm{CO_2}$ and $\mathrm{HCO_3^-}$ are the only inorganic carbon species taken up for photosynthesis by phytoplankton cells, net $\mathrm{HCO_3^-}$ uptake rates are then given as the difference between net carbon fixation and net $\mathrm{CO_2}$ uptake as

$$\mathrm{NetHCO_3^-up_{rate}} = \mathrm{NetFix_{rate}} - \mathrm{NetCO_2up_{rate}} \tag{12}$$

Provided that inorganic carbon can leak out of phytoplankton cells only as $\mathrm{CO_2}$ and not in the ionic forms it follows that net equals gross $\mathrm{HCO_3^-}$ uptake. Furthermore, it is assumed that $\mathrm{HCO_3^-}$ uptake for calcification does not constitute a significant DIC source for photosynthetic carbon fixation (see Fig. 2 for a graphical representation). This is supported by

the following considerations. In coccolithophores $CaCO_3$ is internally produced nearly in isotopic equilibrium with the external DIC pool of which about 90% is HCO_3^-. However, CO_2 is about $10‰$ depleted in ^{13}C compared to HCO_3^-. If calcification in the so-called coccolith vesicle (CV) would share the same internal DIC pool as photosynthesis its isotopic composition would have to be same as the external medium. This, however, is not very likely as the isotopic composition of the internal DIC pool fueling photosynthesis is strongly modified by such factors as the ratio of CO_2 to HCO_3^- uptake, the CO_2 leakage out of the cell and the fractionation against $^{13}CO_2$ by RubisCO. Furthermore, because high pH facilitates $CaCO_3$ formation, the pH in the CV is much higher than in the cytosol or chloroplast. Hence, the CV would rather act as a CO_2 and hence DIC sink for the internal DIC pool fueling photosynthesis than a source. In essence, the HCO_3^- taken up for calcification is not likely to be a significant DIC source for photosynthetic carbon fixation (see Rost and Riebesell (2004) for further details).

Gross CO_2 uptake is estimated from the temporal CO_2 evolution right after switching off the light, $\frac{dCO_2}{dt}D2$ (Fig. 1). Accounting for the chemical disequilibrium in the carbonate system and assuming that inorganic carbon uptake and fixation ceases immediately without the supply of light, CO_2 efflux rates are given by

$$CO_2 eff_{rate} = \frac{dCO_2}{dt}D2 - k_-[HCO_3^-]_{EL} + k_+[CO_2]_{EL} \quad (13)$$

Note that this calculated CO_2 efflux is most likely smaller than the true one, because initial slopes determined with the MIMS setup, such as $\frac{dCO_2}{dt}D2$, tend to be underestimates (for details see Badger et al. (1994); Schulz et al. (2005)). Then, gross CO_2 uptake rate is given as

$$GrossCO_2up_{rate} = NetCO_2up_{rate} + CO_2eff_{rate} \quad (14)$$

It follows that the sum of gross CO_2 and HCO_3^- is the total inorganic carbon uptake rate ($DICup_{rate}$). In summary, the modifications in these calculations compared to those

described previously (Badger et al., 1994) are the explicit inclusion of CO_3^{2-}, the incorporation of calcification and the calculation of the rate constants for the CO_2 to HCO_3^- inter-conversion (Schulz et al., 2005).

Carbon isotope fractionation

In a second experimental approach *Emiliania huxleyi* was grown in duplicate under varying [Fe(III)'] (with the same dilute batch culture setup used for investigation of inorganic carbon fluxes) and stable carbon isotope fractionation was investigated. The carbonate system of the culture media was calculated from pH and total dissolved inorganic carbon (DIC) using the dissociation constants of Mehrbach et al. (1973) as refitted by Dickson and Millero (1987). The pH was measured following the procedure described by DOE (1994) and DIC concentration was determined using a photochemical approach (Stoll et al., 2001).

For analysis of the stable carbon isotope composition of POC, duplicate subsamples of the incubations were filtered on precombusted ($500°C$) Whatman GF/F filters and stored at $-25°C$. Prior to analysis POC filters were fumed with concentrated HCl and analyzed on an ANCA-SL 20-20 Europa Scientific mass spectrometer after 2h of drying at $60°C$. The isotopic composition is reported relative to the PeeDee belemnite (PDB) standard as

$$\delta^{13}C_{\text{sample}} = \left[\frac{(^{13}C/^{12}C)_{\text{sample}}}{(^{13}C/^{12}C)_{\text{PDB}}} - 1 \right] \times 1000 \tag{15}$$

The carbon isotope fractionation associated with POC production (ϵ_p) was calculated relative to the isotopic composition of CO_2 in the medium as

$$\epsilon_p = \left(\frac{\delta^{13}C_{CO_2} + 1000}{\delta^{13}C_{POC} + 1000} - 1 \right) \times 1000 \tag{16}$$

$\delta^{13}C_{CO_2}$ was calculated from the isotopic composition of the DIC pool ($\delta^{13}C_{DIC}$) (Zeebe and Wolf-Gladrow, 2001) making use of the temperature dependent fractionation factors between CO_2 and HCO_3^- (ϵ_{db}), and HCO_3^- and CO_3^{2-} (ϵ_{cb}) given by Mook (1986) and Zhang et al. (1995), respectively

$$\delta^{13}\mathrm{C}_{\mathrm{CO2}} = \delta^{13}\mathrm{C}_{\mathrm{HCO_3^-}} - (1 + \epsilon_{\mathrm{db}} \times 10^{-3}) + \epsilon_{\mathrm{db}} \quad (17)$$

with

$$\delta^{13}\mathrm{C}_{\mathrm{HCO_3^-}} = \frac{\delta^{13}\mathrm{C}_{\mathrm{DIC}}[\mathrm{DIC}] - (\epsilon_{\mathrm{db}}[\mathrm{CO_2}] + \epsilon_{\mathrm{cb}}[\mathrm{CO_3^{2-}}])}{(1 + \epsilon_{\mathrm{db}} \times 10^{-3})[\mathrm{CO_2}] + [\mathrm{HCO_3^-}] + (1 + \epsilon_{\mathrm{cb}} \times 10^{-3})[\mathrm{CO_3^-}]} \quad (18)$$

For determination of the isotopic composition of the DIC pool ($\delta^{13}\mathrm{DIC}$), 8 ml of 0.2 $\mu\mathrm{m}$ filtered subsamples were fixed with $\mathrm{HgCl_2}$ (final concentration $\sim 150\,\mathrm{mg\,kg^{-1}}$) which were analyzed in the laboratory of H. Spero, University of California Davis.

The relationship between stable carbon isotope fractionation and inorganic carbon fluxes was described by Farquhar et al. (1982) and Sharkey and Berry (1985). The two key variables in their model are the so-called leakage, defined as the ratio of the $\mathrm{CO_2}$ efflux to the total inorganic carbon taken up, and the isotopic composition of the inorganic carbon source.

$$\epsilon_{\mathrm{p}} = \mathrm{a}\epsilon_{\mathrm{db}} + \epsilon_{\mathrm{Rub}}\frac{\mathrm{CO_2eff}}{\mathrm{DICup}} \quad (19)$$

where ϵ_{Rub} denotes the kinetic fractionation of RubisCO, which is approximately $29‰$ (Roeske and O'Leary, 1984), ϵ_{db} the equilibrium fractionation between the two carbon sources $\mathrm{CO_2}$ and $\mathrm{HCO_3^-}$. The factor a, introduced by Burkhardt et al. (1999), describes the contribution of $\mathrm{HCO_3^-}$ to the total DIC uptake. However, implicit in this model are the assumptions that (1) the cell consists only of a single compartment, (2) there is no fractionation associated with respiration, and (3) DIC can leak out of the cell only as $\mathrm{CO_2}$ and not in the form of $\mathrm{HCO_3^-}$.

Additionally, in this second experimental approach PIC was determined as the difference between total particulate organic carbon (TPC) and POC, yielding PIC/POC. TPC measurement followed those for POC except that the filters were not fumed with concentrated HCL.

Results

Iron limitation significantly decreased growth rates, cellular Chl *a* concentrations, net photosynthetic CO_2 fixation, as well as concomitant net CO_2 and HCO_3^- uptake rates (see Tab. 1 and Fig. 3). While maximum rates (V_{max}) for net CO_2 fixation per cell were ten times lower under iron limiting compared to iron-replete conditions, changes in corresponding half-saturation concentrations ($K_{1/2}$) did not follow a general trend. Similarly, V_{max} values for net CO_2 uptake rates per cell were highest in iron-replete and dropped to almost zero in iron limiting incubations. Respective $K_{1/2}$ values, however, where highest under iron-replete compared to deplete conditions. The decrease in DIC uptake with increasing iron limitation was the result of almost equally reduced gross CO_2 and HCO_3^- uptake rates. Hence, there was only a slight change in the relative contribution of HCO_3^- to total inorganic carbon uptake towards lower values with decreasing [Fe(III)']. However, DIC and HCO_3^- uptake rates could only be described by Michaelis-Menten uptake kinetics under iron replete conditions. Respiration rates in the dark were about twice as high under iron replete conditions in comparison to limited cells. CO_2 efflux rates were markedly reduced at lower compared to replete iron concentrations but not as much as the DIC uptake rates. Therefore, the leakage ($CO_2 eff_{rate}/DIC up_{rate}$) was calculated to be about twice as high under iron deplete compared to replete conditions. Hence, calculated carbon isotope fractionation (ϵ_p) with respect to external CO_2 according to Eq. 19 would yield $\sim 3.0,\ 8.3$ and $\sim 14.7‰$ under iron replete, intermediate and deplete conditions, respectively. Measured values for ϵ_p obtained in the second experimental setup are in reasonable agreement with those calculated only in the lowest [Fe(III)'] incubation but far too low in the two others (compare Tab. 2). Furthermore, measured values for ϵ_p did not change with the degree of iron limitation but instead stayed rather constant around $12 - 13‰$ (Tab. 1).

Maximum rates of net CO_2 fixation, gross CO_2, HCO_3^- and DIC uptake, and CO_2 efflux normalized to chlorophyll *a*, all decreased with increasing iron limitation, although not as pronounced as corresponding values normalized on a per cell basis (data not shown). This

is due to the markedly diminished chlorophyll *a* content per cell which dropped from about 0.19 under iron replete to 0.02 pg per cell under iron deplete conditions.

Discussion

Iron limitation is a widespread phenomenon in large parts of today's oceans, comprising the Southern Ocean, parts of the North, and the Equatorial Pacific. Hence, physiological responses of phytoplankton to iron limitation, in particular potential changes in modes of carbon acquisition and CCM activity are of great importance for our understanding of marine carbon cycling.

Physiological response to iron limitation

There are many physiological responses to iron limitation. Among those the most pronounced is the remodeling of the photosynthetic apparatus with the loss of functional PSII and most likely PSI reaction centers (Vassiliev et al., 1995), and PSI antenna complexes (Moseley et al., 2002). This leads to increased fluorescence of PSII and decreased chlorophyll *a* content per cell, the so-called chlorosis. Furthermore, the cellular amount of various cytochromes involved in the photosynthetic electron transport are significantly reduced (Greene et al., 1992). Together, these processes result in diminished rates of electron transfer within the photosynthetic apparatus and reduced rates of net photosynthesis (Greene et al., 1991). Reduced growth (division) rates under iron limitation are reflected by the increasing importance of respiration in the dark over net photosynthesis in the light period (see Fig. 3 and Tab. 1). The concomitant down-regulation of net $\mathrm{CO_2}$ and $\mathrm{HCO_3^-}$ uptake rates are most likely the result of both, diminished demand for inorganic carbon, and decreased capability to actively take it up. Demand for and uptake of inorganic carbon are ultimately determined by the amount of energy (ATP) and reductive power (NADPH) generated by electron transport within the photosynthetic apparatus. The ratio is adjusted by the relative proportions of linear ($\mathrm{PSII} \rightarrow \mathrm{PSI} \rightarrow \mathrm{NADPH}$) to cyclic electron flow around PSI (ATP

generation) and Mehler reaction ($\mathrm{PSII} \rightarrow \mathrm{PSI} \rightarrow \mathrm{O_2}$). In all three pathways, however, iron is an integral part of various electron transport components (e.g. cytochromes and FeS clusters). Thus, although the relative proportion of these pathways might change to some extent, iron limitation is likely to reduce both energy and reductive power supply. This, in turn, results in reduced uptake rates for DIC. In contrast, the $\mathrm{CO_2}$ loss from the cells was not reduced as much as compared to DIC uptake, indicating diminished CCM efficiency under iron limitation.

Carbon isotope fractionation

Stable carbon isotope fractionation in marine phytoplankton has been shown to vary with changing environmental conditions such as temperature and [$\mathrm{CO_2}$] (Freeman and Hayes, 1992; Goericke and Fry, 1994). More specifically, it has been suggested that ϵ_p can be described with an inverse relationship between growth rate and $\mathrm{CO_2}$ concentration (Laws et al., 1995). Furthermore, it was pointed out that carbon isotope fractionation is affected by the kind of growth rate limiting resource (Riebesell et al., 2000). Surprisingly, although in this study growth rates varied about 3 fold, there was no measured change in carbon isotope fractionation (Tab.2). These results seem to contradict the inorganic carbon flux measurements which show increasing leakage under iron limitation. Thus, the basic model given in Eq. 19 would predict a significant enhancement of carbon isotope fractionation. However, this model considers the cell comprising only one compartment which is obviously far from a realistic representation of a cell's internal structure. Therefore a new model was constructed with an additional compartment, representing the chloroplast (Fig. 4). From a mass-balance of the fluxes into and out of the two compartments, termed hereafter as the cytosol and the chloroplast, ϵ_p can be calculated. The mass balance for the cytosol reads

$$\mathrm{F_{cyt}CO_2} + \mathrm{F_{cyt}HCO_3^-} = \mathrm{F_{chl}CO_2} + \mathrm{F_{chl}HCO_3^-} - \mathrm{F_{chl}out} + \mathrm{F_{cyt}out} \tag{20}$$

and for the chloroplast

$$\mathrm{F_{chl}CO_2} + \mathrm{F_{chl}HCO_3^-} = \mathrm{FIX} + \mathrm{F_{chl}out} \tag{21}$$

From total $^{12}\mathrm{C}$ and $^{13}\mathrm{C}$ fluxes $^{13}\mathrm{C}$ fluxes can be derived introducing the isotopic ratio R of a carbon specimen defined as $\mathrm{R} = {}^{13}\mathrm{C}/{}^{12}\mathrm{C}$. Multiplying the total fluxes with the respective R introduces an error in the mass balance because $^{12}\mathrm{C}$ and the total amount of carbon are not identical. However, this error will be small for carbon as about 99% of carbon is $^{12}\mathrm{C}$. As $\mathrm{HCO_3^-}$ is about $10‰$ enriched in $^{13}\mathrm{C}$ compared to $\mathrm{CO_2}$ this fractionation is taken into account by introducing a fractionation factor α_{db} between $\mathrm{CO_2}$ and $\mathrm{HCO_3^-}$ defined as $\alpha_{\mathrm{db}} = \mathrm{R_{CO_2}}/\mathrm{R_{HCO_3^-}}$. It is calculated from the fractionation factor ϵ_{db} given by Mook (1986) as $\alpha_{\mathrm{db}} = (\epsilon_{\mathrm{db}} + 1) \times 1000$. For convenience the fractionation is expressed between $\mathrm{HCO_3^-}$ and $\mathrm{CO_2}$ as $\alpha_{\mathrm{bd}} = 1/\alpha_{\mathrm{db}}$. In analogy, a fractionation factor α_{Rub} is taken to describe the isotopic fractionation against $^{13}\mathrm{C}$ by RubisCO associated with organic carbon fixation. Because ϵ_{Rub} is defined as $\epsilon_{\mathrm{Rub}} = \mathrm{R_{POC}}/\mathrm{R_{CO_2}}$ it follows that $\alpha_{\mathrm{Rub}} = (\epsilon_{\mathrm{Rub}} + 1) \times 1000$.

Hence, the mass balance for $^{13}\mathrm{C}$ in the cytosol can be written as

$$\begin{aligned} \mathrm{R_{ext}F_{cyt}CO_2} + \alpha_{\mathrm{bd}}\mathrm{R_{ext}F_{cyt}HCO_3^-} &= \mathrm{R_{cyt}\,F_{chl}CO_2} + \alpha_{\mathrm{bd}}\mathrm{R_{cyt}\,F_{chl}HCO_3^-} \\ &\quad -\mathrm{R_{chl}\,F_{chl}out} + \mathrm{R_{cyt}\,F_{cyt}out} \end{aligned} \tag{22}$$

and for the chloroplast as

$$\mathrm{R_{cyt}\,F_{chl}CO_2} + \alpha_{\mathrm{bd}}\mathrm{R_{cyt}\,F_{chl}HCO_3^-} = \mathrm{R_{chl}\,Fixation}/\alpha_{\mathrm{Rub}} + \mathrm{R_{chl}\,F_{chl}out} \tag{23}$$

with $\mathrm{R_{ext}}$, $\mathrm{R_{cyt}}$ and $\mathrm{R_{chl}}$ denoting the ratio between $^{13}\mathrm{C}$ and $^{12}\mathrm{C}$ of $\mathrm{CO_2}$ in the external medium, the cytosol and the chloroplast, respectively. Eq. 23 can be rearranged for $\mathrm{R_{cyt}}$ and substituted into Eq. 22, which in turn is solved for $\mathrm{R_{chl}}$, resulting in

$$\begin{aligned} \mathrm{R_{chl}} &= (\mathrm{R_{ext}\,F_{cyt}CO_2} + \alpha_{\mathrm{bd}}\mathrm{R_{ext}\,F_{cyt}HCO_3^-})/ \\ &\left[\frac{(\mathrm{FIX}/\alpha_{\mathrm{Rub}} + \mathrm{F_{chl}out})(\mathrm{F_{chl}CO_2} + \alpha_{\mathrm{bd}}\mathrm{F_{chl}HCO_3^-} + \mathrm{F_{cyt}out})}{\mathrm{F_{chl}CO_2} + \alpha_{\mathrm{bd}}\mathrm{F_{chl}HCO_3^-}} - \mathrm{F_{chl}out}\right] \end{aligned} \tag{24}$$

Hence, fractionation between the isotopic composition of the external $\mathrm{CO_2}$ and the particulate organic matter built up during carbon fixation is given as

$$\epsilon_{\mathrm{p}} = (\alpha_{\mathrm{Rub}}\frac{\mathrm{R_{ext}}}{\mathrm{R_{chl}}} - 1) \times 1000 \tag{25}$$

Note that fractionation is independent of the external isotopic composition of $\mathrm{CO_2}$ as it is defined relative to $\mathrm{R_{ext}}$.

The results from the two compartment model demonstrate that for the leakage determined with the MIMS ϵ_{p} can vary enormously. It is dependent on the $\mathrm{HCO_3^-}$ fraction of the total DIC uptake into the chloroplast, but most importantly on the '$\mathrm{DIC\,turnover\,factor_{chloroplast}}$' (Fig. 5). It describes the magnitude of the fluxes in and out of the chloroplast in relation to the external fluxes measured by the MIMS (DIC fluxes into the cytosol and the $\mathrm{CO_2}$ efflux). Comparing this and the one compartment model given by Eq. 19 (Fig. 5) it becomes evident that ϵ_{p} calculated by the one box compartment model can be envisioned as the maximum fractionation possible for a compartmented cell. Furthermore, given the fact that under most environmental conditions there is significant fractionation between the external isotopic composition of $\mathrm{CO_2}$ and the POC fixed by RubisCO, implies that the internal fluxes in and out of the chloroplast generally exceed those from and to the external medium by at least an order of magnitude (Fig. 5). Therefore, it is likely that under iron and hence energy limitation the magnitude of the fluxes in and out of the chloroplast is much more affected compared to the others. This in turn, can explain why there is no measured change in fractionation with rising iron limitation, although the leakage via the plasmalemma is increasing. The reason that the absolute values calculated for fractionation are lower than

the ones measured is probably caused by underestimating the CO_2 efflux right after turning off the light (determined by the initial slope of the CO_2 evolution). This is based on the fact that mixing in the cuvette and changes of the gas flow through the membrane upon rapid disturbance in the carbonate system are not instant processes, masking the initial CO_2 evolution (Badger et al., 1994; Schulz et al., 2005; Rost et al., 2005).

In summary, the fluxes determined with the MIMS probably only represent the tip of an iceberg when compared to the total carbon fluxes within the CCM system.

Iron versus light limitation: Fe = mc^2 ?

For phytoplankton cells, iron limitation poses a severe problem, i.e a reduction in energy available for cellular processes. Although chlorophyll content per cell decreases under iron and increases under light limitation, these responses can be seen as the two sides of the same coin. While the first is thought to prevent damage to the photosynthetic apparatus because electrons cannot be transported at maximum speed to the terminal electron acceptor, the second is employed to increase the amount of photons absorbed by the antenna complexes of PSI and PSII. Nevertheless, both limitations will results in a strong reduction of electrons transported and therefore energy availability will be reduced. Interestingly, measured carbon isotope fractionation in *Emiliania huxleyi* under various light dark cycles showed only a minor response ($3 - 4‰$) to changes in light intensity, although growth rates varied by a factor of two (Rost et al., 2002). This suggests that total carbon fluxes (external and internal) under light limitation are likely to be equally affected as by the lack of sufficient amounts of iron. The insensitivity of ϵ_p to a 3 fold decrease in growth rate due to lower light intensities was also observed in a marine diatom (Riebesell et al., 2000).

Implications for paleoreconstructions

The apparent lack of any significant response in ϵ_p to changes in the degree of iron limitation may be of potential interest for the interpretation of sedimentary records of carbon

isotope data in today's HNLC areas of the ocean. Here, the diverse group of diatoms is dominating the phytoplankton biomass. If the results of this study proof to equally apply to marine diatoms, higher dust and therefore iron input to today's HNLC regions in glacial times (Mahowald et al., 1999) should not alter their carbon isotope fractionation. In contrast, it has been shown that $\delta^{13}\mathrm{C}_{\mathrm{phytol}}$, the isotopic composition of a biomarker for marine phytoplankton, decreased by about $7‰$ upon several additions of iron in the equatorial Pacific (Bidigare et al., 1999). Although Trull and Armand (2001) also observed a decrease of $\delta^{13}\mathrm{C}_{\mathrm{org}}$, the isotopic composition of POC, upon iron addition in the Southern Ocean, they showed that phytoplankton in the range between 1 and 5 $\mu\mathrm{m}$ is about $8‰$ more depleted in $^{13}\mathrm{C}$ in comparison to phytoplankton in the range of 20 to 70 $\mu\mathrm{m}$. Moreover, $\delta^{13}\mathrm{C}_{\mathrm{org}}$ in different size classes of phytoplankton was insensitive to iron additions, remaining rather constant. This implies that $\delta^{13}\mathrm{C}_{\mathrm{phytol}}$ or $\delta^{13}\mathrm{C}_{\mathrm{org}}$ was likely to be related to a change in phytoplankton community structure from smaller to larger cells upon alleviation of iron limitation. Furthermore, the isotopic composition of organic matter produced by phytoplankton is hardly affected by changes in atmospheric $p\mathrm{CO}_2$, within its natural variations, nor by changes in temperature. Oscillation of $\delta^{13}\mathrm{C}_{\mathrm{org}}$ in the sedimentary records in the HNLC areas of today's oceans may therefore be indicative for changes in the contribution of larger phytoplankton cells to total biomass and hence changes in the strength of marine carbon sequestration.

References

Baar de, H. J. W., Boyd, P. W., 2000. The role of iron in plankton ecology and carbon dioxide transfer of the global oceans, p.61-140 *In* Hanson, R.B. and Dicklow, H.W. and Fields, J.G. [eds.], The Changing Ocean Carbon Cycle. Cambridge Univ. Pres.

Badger, M. R., Andrews, T., Whitney, S. M., Ludgwig, M., Yellowlees, D. C., Leggat, W., Price, G. D., 1998. The diversity and coevolution of Rubisco, plastids, pyrenoids, and chloroplast-based CO_2-concentrating mechanisms in algae. Can. J. Bot. 76, 1052–1071.

Badger, M. R., Palmqvist, K., Yu, J.-W., 1994. Measurement of CO_2 and HCO_3^- fluxes in cyanobacteria and microalgae during steady-state photosynthesis. Physiol. Plant. 90, 529–536.

Beardall, J., 1991. Effects of photon flux density on the 'CO_2-concentrating mechanism' of the cyanobacterium *Anabaena variabilis*. J. Plankt. Res. 13, 133–141.

Berry, L., Taylor, A. R., Lucken, U., Ryan, K. P., Brownlee, C., 2002. Calcification and inorganic carbon acquisition in coccolithophores. Func. Plant. Bio. 29, 289–299.

Bidigare, R. R., Hanson, K. L., Buesseler, K. O., Wakeham, S. G., Freeman, K. H., Pancost, R. D., Millero, F. J., Steinberg, P., Popp, B. N., Latasa, M., Landry, M. R., Laws, E. A., 1999. Iron-stimulated changes in ^{13}C fractionation and export by equatorial Pacific phytoplankton: Toward a paleogrowth rate proxy. Paleoceanogr. 14, 589–595.

Burkhardt, S., Amoroso, G., Riebesell, U., Sültemeyer, D., 2001. CO_2 and HCO_3^- uptake in marine diatoms acclimated to different CO_2 concentrations. Limnol. Oceanogr. 46, 1378–1391.

Burkhardt, S., Riebesell, U., Zondervan, I., 1999. Effects of growth rate, CO_2 concentration, and cell size on the stable carbon isotope fractionation in marine phytoplankton. Geochim. Cosmocim. Acta 63, 3729–3741.

Davison, I., 1987. Adaption of photosynthesis in *Laminaria saccarina* (Phaeophyta) to changes in growth temperature. J. Phycol. 23, 273–283.

Dickson, A. G., Millero, F. J., 1987. A comparison of the equilibrium constants for the dissociation of carbonic acid in seawater media. Deep-Sea Res. 34, 1733–1743.

DOE, 1994. Handbook of Methods for the Analysis of the Various Parameters of the Car bon Dioxide System in Seawater, version 2. A. G. Dickson and C. Goyet, eds., ORNL/CDIAC-74.

Falkowski, P. G., Raven, J., 1997. Aquatic photosynthesis. Blackwell Science.

Farquhar, G. D., O'Leary, M. H., Berry, J. A., 1982. On the relationship between carbon isotope discrimination and the intercellular carbon dioxide concentration in leaves. Aust. J. Plant Physiol. 9, 121–137.

Freeman, K. H., Hayes, J. M., 1992. Fractionation of cabon isotopes by phytoplankton and estimates of ancient CO_2 levels. Glob. Biochem. Cycl. 6, 185–198.

Garcia, H. E., Gordon, L. I., 1992. Oxygen solubility in seawater: Better fitting equations. Limnol. Oceanogr. 37, 1307–1312.

Goericke, R., Fry, B., 1994. Variations of marine plankton $\delta^{13}C$ with latitude, temperature, and dissolved CO_2 in the world ocean. Glob. Biochem. Cycles 8, 85–90.

Greene, R. M., Geider, R. J., Falkowski, P. G., 1991. Effect of iron limitation on photosynthesis in a marine diatom. Limnol. Oceanogr. 36, 1772–1782.

Greene, R. M., Geider, R. J., Kolber, Z., Falkowski, P. G., 1992. Iron-induced Changes in Light Harvesting and Photochemical Energy Conversion Processes in Eukaryotiv Marine Algae. Plant Physiol. 100, 565–575.

Laws, E. A., Popp, B. N., Bidigare, R. R., Kennicutt, M. C., Macko, S. A., 1995. Dependence of phytoplankton carbon isotopic composition on growth rate and $[CO_2]_{aq}$: Theoretical considerations and experimental results. Geochim. Cosmochim. Acta 59, 1131–1138.

Laws, E. A., Popp, B. N., Cassar, N., Tanimoto, J., 2002. ^{13}C discrimination patterns in oceanic phytoplankton: likely influence of CO_2 concentrating mechanisms, and implications for paleoreconstructions. Funct. Plant Biol., 323–333.

Mahowald, N., Kohfeld, K., Hansson, M., Balkanski, Y., Harrison, S. P., Prent ice, I. C., Schulz, M., Rodhe, H., 1999. Dust sources and deposition during the last glacial maximum and current climate: A comparis ion of model results with paleodata from ice cores and marine sediments. J. Geophys. Res. 104, 15895–15916.

Mehrbach, C., Culberson, C. H., Hawley, J. E., Pytkowicz, R. N., 1973. Measurement of the apparent dissociation constants of carbonic acid in seawater. Limnol. Oceanogr. 18, 897–907.

Mook, W. G., 1986. ^{13}C in atmospheric CO_2. Neth. J. Sea Res. 20, 211–223.

Moseley, J. L., Allinger, T., Herzof, S., Hoerth, P., Wehinger, E., Merchant, S., Hippler, M., 2002. Adaptation to Fe-deficiency requires remodeling of the photosynthetic apparatus. EMBO Journal 21, 6709–6720.

Paasche, E., 2001. A review of the coccolithophorid *Emiliania huxleyi* (Prymnesiophyceae). Phycologia 40, 508–529.

Raven, J. A., Johnston, A. M., Kübler, J. E., Korb, R. E., McInroy, S. G., Handley, L. L., Scrimgeour, C. M., Walker, D. I., Beardall, J., Vanderklift, M., Fredriksen, S., Dunton,

J. H., 2002. Mechanistic interpretation of carbon isotope discrimination by marine macroalgae and seagras. Funct. Plant Biol. 29, 355–378.

Raven, J. A., Lucas, W. J., 1985. Energy costs of carbon acquisition, p. 305-324 *In* Lucas, W. J. and Berry, J. A. [eds.], Inorganic carbon Uptake by Aquatic Photosynthetic Organisms. American Society of Plant Physiologists.

Riebesell, U., Burkhardt, S., Dauelsberg, A., Kroon, B., 2000. Carbon isotope fractionation by a marine diatom: dependence on the growth-rate-limiting resource. Mar. Ecol. Progr. Ser. 193, 295–303.

Roeske, C., O'Leary, M., 1984. Carbon isotope effects on the enzyme-catalyzed carboxilation of ribulose bisphosphate. Biochem. 23, 6275–6285.

Rost, B., Richter, K.-W., Riebesell, U., Hansen, R. J., 2005. Inorganic carbon acquisition in red tide dinoflagellates. accepted by Plant Cell and Environ.

Rost, B., Riebesell, U., 2004. Coccolithophore calcification and the biological carbon pump: response to environmental changes *In* Thierstein, H. R. and Young, J. R. [eds.], Coccolithophores From Molecular Processes to Global Impact. Springer-Verlag Berlin Heidelberg.

Rost, B., Riebesell, U., Burkhardt, S., Sultemeyer, D., 2003. Carbon acquistion of bloom-forming marine phytoplankton. Limnol. Oceanogr. 48, 55–67.

Rost, B., Riebesell, U., Sültemeyer, D., 2006. Carbon acquisition of marine phytoplankton: Effect of photoperiod length. accepted by Limnol. Oceanogr.

Rost, B., Zondervan, I., Riebesell, U., 2002. Light-dependent carbon isotope fractionation in the coccolithophore *Emiliania huxleyi*. Limnol. Oceanogr. 47, 120–128.

Schulz, K. G., Riebesell, U., Rost, B., Thoms, S., Zeebe, R. E., 2005. Determination of the rate constants for the carbon dioxide to bicarbonate inter-conversion in pH-buffered seawater systems. Mar. Chem., accepted.

Schulz, K. G., Zondervan, I., Gerringa, L. J. A., Timmermans, K. R., Veldhuis, M. J. W., Riebesell, U., 2004. Effect of trace metal availability on coccolithophorid calcification. Nature 430, 673–676.

Sharkey, T. D., Berry, J. A., 1985. Carbon isotope fractionation of algae as influenced by an inducible CO_2 concentrating mechanism *In* Lucas, W. J. and Berry, J. A. [eds.], Inorganic carbon Uptake by Aquatic Photosynthetic Organisms. American Society of Plant Physiologists.

Stoll, M. H. C., Bakker, K., Nobbe, G. H., Haese, R. R., 2001. Continuous flow analysis of dissolved inorganic carbon content in seawater. Anal. Chem. 73, 4111–4116.

Strickland, J. D. H., Parsons, T. R., 1968. A practical handbook of seawater analysis. Bull. Fish. Res. Bd. Canada, 167.

Trull, T. W., Armand, L., 2001. Insights into Southern Ocean carbon export from $\delta^{13}C$ of particles and dissolved inorganic carbon during the SOIREE iron release experiment. Deep See Res. 48, 2655–2680.

Vassiliev, I. R., Kolber, Z., Wyman, K., Mauzerall, D., Shukla, V. K., Falskowski, P. G., 1995. Effects of Iron Limitation on Photosystem II Composition and Light Utilization in *Dunaliella teriolecta*. Plant Physiol. 109, 963–972.

Zeebe, R. E., Wolf-Gladrow, D., 2001. CO_2 in seawater: equilibrium, kinetics, isotopes. Vol. 65 of Elsevier Oceanography Series. Elsevier.

Zhang, J., Quay, P. D., Wilbur, D. O., 1995. Carbon isotope fractionation during gas-water exchange and dissolution of CO_2. Geochim. Cosmochim. Acta 59, 107–114.

Table 2: V_{max} and $K_{1/2}$ values for net CO_2 fixation, net CO_2 and HCO_3^- uptake, HCO_3^- to DIC uptake ratio, leakage, growth rates and cellular chlorophyll *a* content of *Emiliania huxleyi* cultured under iron replete, intermediate and deplete conditions. Kinetic parameters were obtained from a modified Michaelis-Menten fit, accounting for a cellular minimum CO_2 or HCO_3^- requirement, to the combined data from independent measurements. Values for V_{max} and $K_{1/2}$ are given in $pmol\,kg^{-1}\,cell^{-1}\,h^{-1}$ and $\mu mol\,kg^{-1}$, growth rates in divisions per day and chlorophyll *a* per cell in pg, respectively.

	Net fixation				Net CO_2 uptake	
[Fe(III)']	V_{max} (CO_2)	$K_{1/2}$ (CO_2)	V_{max} (HCO_3^-)	$K_{1/2}$ (HCO_3^-)	V_{max}	$K_{1/2}$
replete	0.071	5.0	0.070	328	0.025	4.8
intermediate	0.017	4.2	0.017	265	0.005	5.7
deplete	0.007	7.5	0.008	436	0.0003	–

	Net HCO_3^- uptake		HCO_3^-/DIC	Leakage	Growth	Chl *a*/cell
[Fe(III)']	V_{max}	$K_{1/2}$			μ	
replete	0.051	443	0.48±0.05	0.28±0.03	0.86±0.01	0.19±0.03
intermediate	–	–	0.43±0.09	0.45±0.04	0.43±0.01	0.05±0.01
deplete	–	–	0.38±0.03	0.66±0.04	0.28±0.01	0.02±0.01

Table 3: Growth rates (μ), carbon isotope fractionation (ϵ_{p}) and ratio of particulate inorganic to particulate organic carbon (PIC/POC) of *Emiliania huxleyi* grown at $\mathrm{pH_T}$ 7.85 and 8.3 under varying [Fe(III)']. Growth rates are reported in divisions per day, fractionation in permil and [Fe(III)'], calculated as described in Schulz et al. (2004), in $\mathrm{pmol\,kg^{-1}}$

	[Fe(III)']	μ	ϵ_{p}	PIC/POC
$\mathrm{pH_T}$ 7.85				
	132	1.00±0.00	12.6±0.2	0.55±0.02
	4.8	0.83±0.01	12.4±0.2	0.55±0.02
	2.9	0.74±0.00	11.5±0.2	0.54±0.04
	0.96	0.41±0.01	12.6±0.3	0.54±0.06
	0.06	0.23±0.00	12.8±0.7	0.58±0.01
$\mathrm{pH_T}$ 8.3				
	360	1.04±0.00	13.8±0.3	0.59±0.03
	8.9	0.98±0.00	11.7±0.1	0.60±0.03
	4.6	0.86±0.01	13.9±0.5	0.59±0.05
	2.0	0.70±0.01	12.6±0.1	0.61±0.04
	0.2	0.54±0.00	15.6±0.3	0.74±0.10

Figure 1: Example of O_2 (**a**) and CO_2 (**b**) evolution of *Emiliania huxleyi* measured during a consecutive dark/light cycle. The O_2 evolution at the end of the dark period ($\frac{dO_2}{dt}$D) depicts the respiration rate in the dark, $\frac{dO_2}{dt}$L the net fixation rate, and $[O_2]_{BL}$ and $[O_2]_{EL}$ the oxygen concentrations at the end of dark and light phase, respectively. When accounting for the chemical disequilibrium in the carbonate system, the CO_2 evolution at the end of the dark period ($\frac{dCO_2}{dt}$ D1) equally describes the respiration rate in the dark, as does the simultaneous oxygen evolution. $\frac{dCO_2}{dt}$L describes the net CO_2 uptake and $\frac{dCO_2}{dt}$D2 the CO_2 efflux rate. $[CO_2]_{BL}$ and $[CO_2]_{EL}$ depict the carbon dioxide concentrations at the end of the dark and light period, respectively.

Figure 2: Carbon fluxes as detectable with the approach desribed in the Methods section. ϵ_{Rub} illustrates carbon isotope fractionation of RubisCO associated with photosynthetic CO_2 fixation.

Figure 3: Cellular rates of net CO_2 fixation (NetFix), net CO_2 (CO_2up), net HCO_3^- (HCO_3^-up) and total inorganic carbon uptake (DICup), and CO_2 efflux. The grey shaded area denotes the respiration rate in the dark within statistical boundaries (one standard deviation). The upper panel shows rates at [Fe(III)'] replete, the middle at intermediate and the lower at deplete conditions. For corresponding growth rates see Tab. 1.

Figure 4: Intracellular carbon fluxes in a cell with two compartments, the cytosol and the chloroplast (shown in grey). F_{cyt} denote the fluxes of CO_2 and HCO_3^- from the external medium into the cytosol, and $F_{cyt}out$ the CO_2 flux out of the cytosol. Similarly, F_{chl} represents the fluxes from the cytosol into the chloroplast, and $F_{cyt}out$ the corresponding CO_2 flux out of the chloroplast. ϵ_{Rub} illustrates the fractionation of RubisCO associated with carbon fixation.

Figure 5: Calculated ϵ_p by the two compartment model shown in Fig. 4 and given by Eqs. 24 and 25. The fluxes from the external medium into the cytosol were chosen to match the

measured fluxes, i.e. CO_2 and HCO_3^- are contributing to total DIC uptake equally and the CO_2 flux out of the cell is about half the DIC influx. The '$\mathrm{DIC\,turnover\,factor_{chloroplast}}$' defines the DIC uptake into and the CO_2 flux out of the chloroplast in proportion to the DIC uptake from the external medium into the cytosol ($F_{cyt}CO_2$ and $F_{cyt}HCO_3^-$) and the CO_2 efflux out of the cell ($F_{cyt}out$), respectively. The solid line shows ϵ_p in relation to '$\mathrm{DIC\,turnover\,factor_{chloroplast}}$' when the HCO_3^- fraction of the total DIC uptake into the chloroplast is zero, i.e. carbon enters the chloroplast only in form of CO_2. The dashed and dotted lines show results for a HCO_3^- fraction of 0.5 and 1, respectively. The grey shaded horizontal bar illustrates the corresponding fractionation predicted by the one compartment model given in Eq. 19.

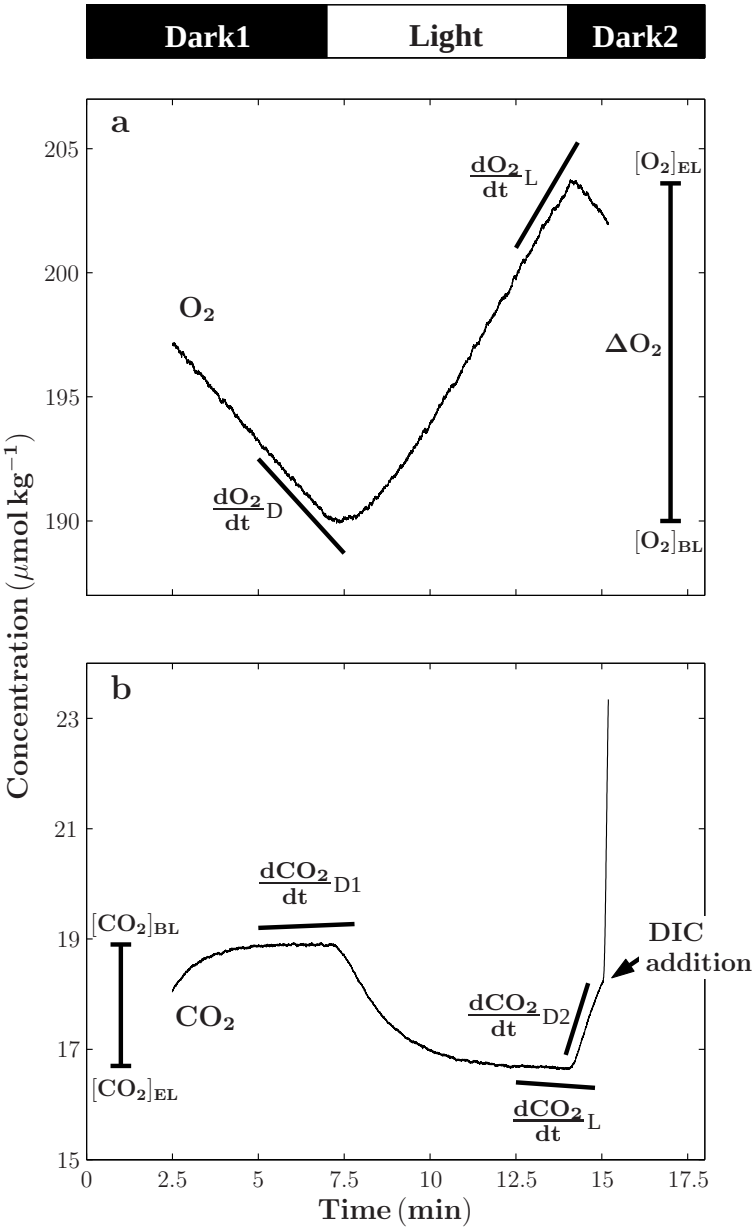
Dark1
Light
Dark2
a
b
O_2
$\frac{dO_2}{dt}_L$
$\frac{dO_2}{dt}_D$
$[O_2]_{EL}$
$[O_2]_{BL}$
ΔO_2
CO_2
$\frac{dCO_2}{dt}_{D1}$
$\frac{dCO_2}{dt}_{D2}$
$\frac{dCO_2}{dt}_L$
$[CO_2]_{BL}$
$[CO_2]_{EL}$
DIC addition
Concentration (μmol kg^{-1})
Time (min)

Figure 1

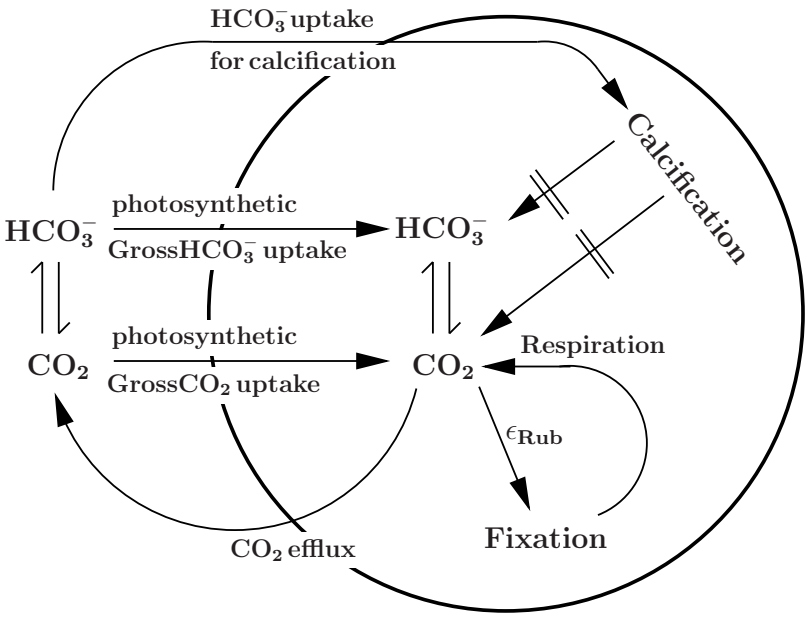
HCO_3^- uptake
for calcification
Calcification
HCO_3^-
photosynthetic
GrossHCO_3^- uptake
HCO_3^-
CO_2
photosynthetic
GrossCO_2 uptake
CO_2
Respiration
ϵ_{Rub}
Fixation
CO_2 efflux

Figure 2

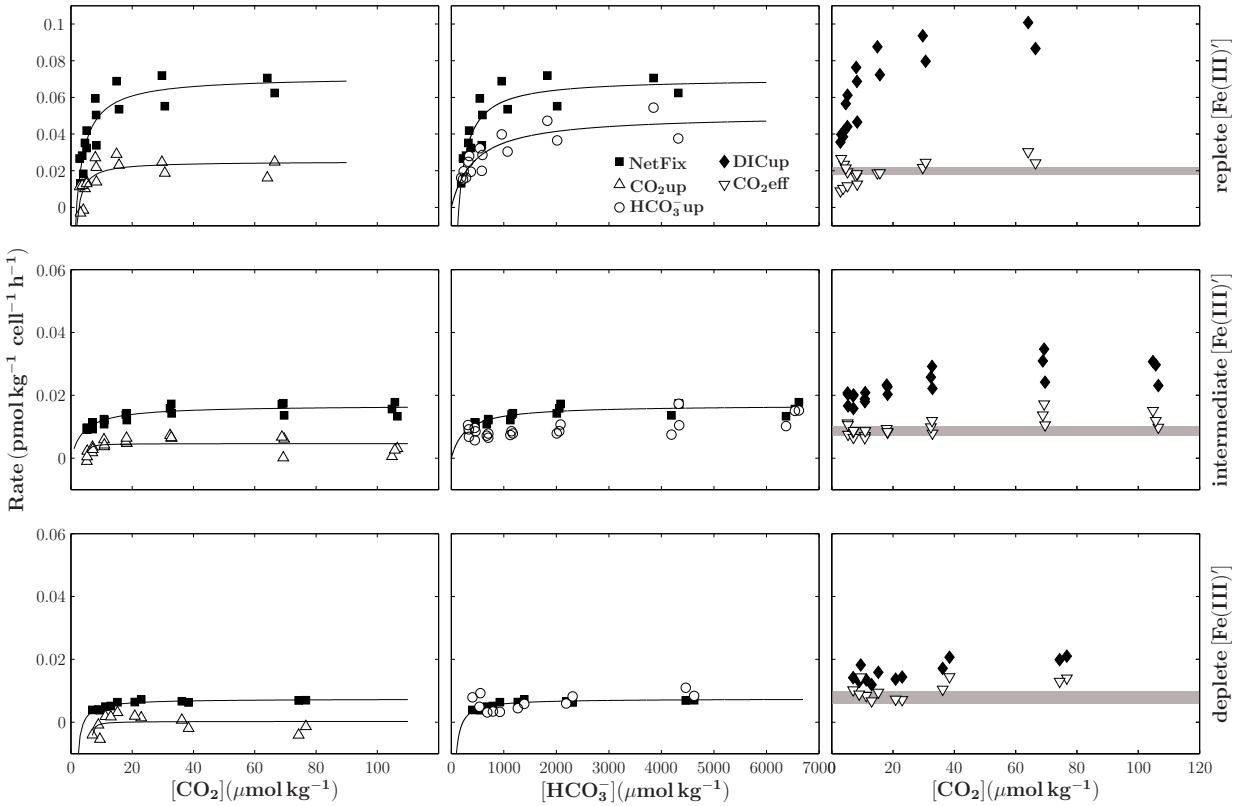
Rate (pmol kg^{-1} cell^{-1} h^{-1})
NetFix
DICup
CO$_2$up
CO$_2$eff
HCO$_3^-$up
replete [Fe(III)']
intermediate [Fe(III)']
deplete [Fe(III)']
[CO$_2$] (μmol kg^{-1})
[HCO$_3^-$] (μmol kg^{-1})
[CO$_2$] (μmol kg^{-1})

Figure 3

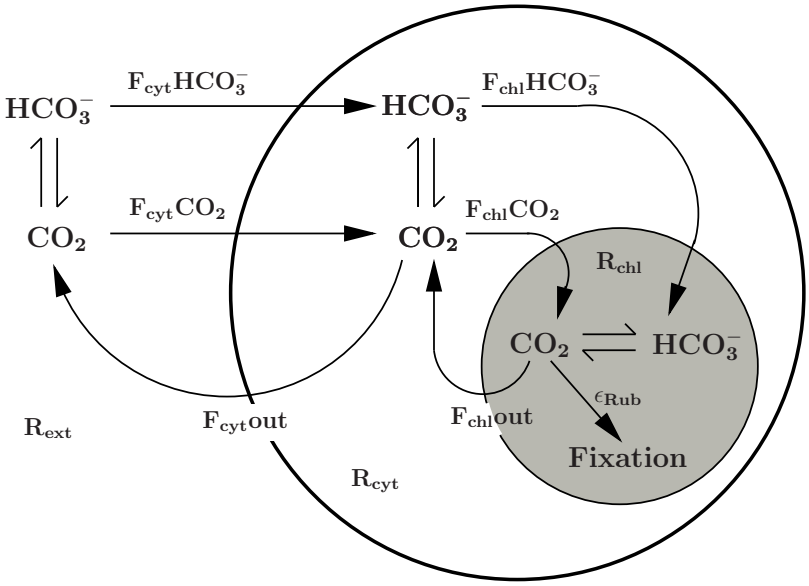
HCO_3^-
$F_{cyt}HCO_3^-$
HCO_3^-
$F_{chl}HCO_3^-$
$F_{cyt}CO_2$
CO_2
$F_{chl}CO_2$
CO_2
R_{chl}
CO_2 HCO_3^-
ϵ_{Rub}
Fixation
R_{ext}
$F_{cyt}out$
$F_{chl}out$
R_{cyt}

Figure 4

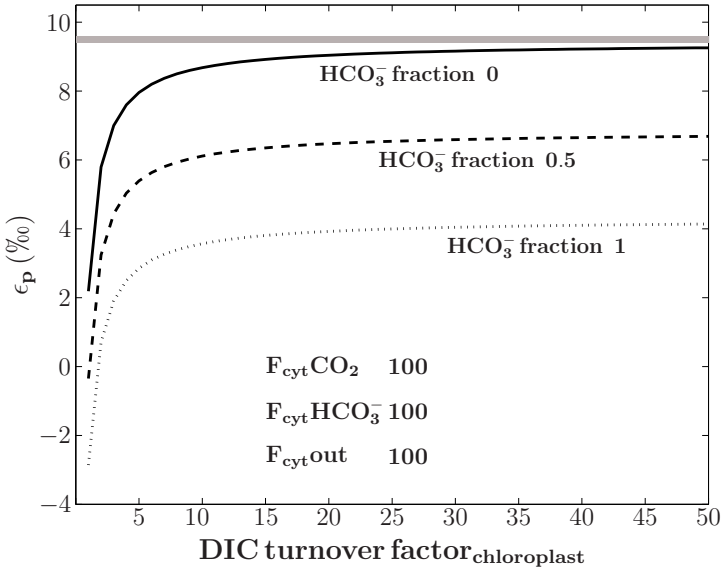
10
8
6
4
2
0
−2
−4
5
10
15
20
25
30
35
40
45
50
ϵ_p (‰)
DIC turnover factor$_{chloroplast}$
HCO_3^- fraction 0
HCO_3^- fraction 0.5
HCO_3^- fraction 1
$F_{cyt}CO_2$ 100
$F_{cyt}HCO_3^-$ 100
F_{cyt}out 100

Figure 5

Determination of the rate constants for the carbon dioxide to bicarbonate inter-conversion in pH-buffered seawater systems

K.G. Schulz[1*], U. Riebesell[1], B. Rost[2], S. Thoms[2], R.E. Zeebe[3]

[1]*Leibniz Institute for Marine Sciences, Düsternbrooker Weg 20, 24105 Kiel, Germany*

[2]*Alfred Wegener Institute for Polar and Marine Research, P.O. Box 12016, 27515 Bremerhaven, Germany*

[3]*University of Hawaii at Manoa SOEST Department of Oceanography 1000 Pope Road, MSB 504 Honolulu, HI 96822, USA*

E-mail: kschulz@ifm-geomar.de (K.G. Schulz)
uriebesell@ifm-geomar.de (U. Riebesell)
brost@awi-bremerhaven.de (B. Rost)
sthoms@awi-bremerhaven.de (S. Thoms)
zeebe@hawaii.edu (R.E. Zeebe)

*Corresponding author: kschulz@ifm-geomar.de (K.G. Schulz)
phone: 0049 (0)431 600 4510
fax: 0049 (0)431 600 1515

Accepted by *Marine Chemistry*

Abstract

Experimental setups to study modes of inorganic carbon acquisition and fixation rates by marine phytoplankton commonly make use of so-called disequilibrium techniques. The chemical or isotopic disequilibrium, either caused by phytoplankton cells taking up inorganic carbon or by a small disturbance of the isotopic equilibrium in the carbonate system, requires to account for the relatively slow chemical interconversion of carbon dioxide (CO_2) to bicarbonate (HCO_3^-) in seawater. Because in such experiments a constant pH is a prerequisite, pH buffers are generally used. However, a possible influence of such buffers on the kinetics of the carbonate system has hitherto not been investigated. Here, a model of the carbonate system in seawater is employed to show how pH buffers are operating. Furthermore, a new approach is presented to determine the rate constants, k_+ and k_-, for the conversion reaction of CO_2 to HCO_3^- and vice versa, by means of membrane inlet mass spectrometry (MIMS). For the two pH buffers tested (HEPES and BICINE) it is shown that measured rate constants are in good agreement with calculated values for k_+ and k_- in a pH range of 7 to 8.5 and at temperatures from 10 to $25°C$.

1 Introduction

In the last 200 years, starting with the industrial revolution, the ocean has taken up $\sim 50\%$ of the carbon dioxide (CO_2) emitted by mankind's consumption of fossil fuels. The projected doubling of current atmospheric CO_2 around the year 2100 (Houghton et al., 1995) and its continuing oceanic uptake will give rise to a 60% increase in hydrogen ion concentration in the surface ocean (Sabine et al., 2004). This ocean acidification also involves a redistribution in the dissolved inorganic carbon (DIC) pool, increasing CO_2 and bicarbonate (HCO_3^-) at the expense of carbonate ion (CO_3^{2-}) concentrations. It has been shown, both in experimental and in modelling studies, that mechanisms and efficiencies of inorganic carbon acquisition by marine phytoplankton, which is responsible for about half of

global net primary production (Field et al., 1998), are sensitive to the availability of CO_2 in seawater (Burkhardt et al., 2001; Rost et al., 2003; Thoms et al., 2001). Moreover, these can differ greatly between various groups of phytoplankton species (Rost et al., 2003, 2005). The consequences of future DIC redistribution for species composition and inorganic carbon fixation, however, are largely unknown. Assessment of these potential changes includes studies on mechanisms and efficiencies of inorganic carbon acquisition by different phytoplankton groups, making use of so-called disequilibrium techniques. While the mass spectrometric approach measures the disequilibrium caused by photosynthetic uptake of inorganic carbon (Badger et al., 1994), the ^{14}C disequilibrium technique monitors inorganic carbon fixation upon a small disturbance in the isotopic equilibrium of the carbonate system (Cooper et al., 1969; Espie and Colman, 1986). Both methods require exact knowledge of the response of the carbonate system to the disequilibrium employed, i.e. the kinetic rate constants for the chemical inter-conversion between CO_2 and HCO_3^-. Here we present a method for the exact determination of these rate constants by means of membrane inlet mass spectrometry (MIMS) and compare it with an approach described previously. Furthermore, adopting a model of the carbonate system in seawater, we explore the validity of the assumptions associated with these two approaches.

2 Methods

2.1 The experimental setup

All measurements were performed in artificial seawater following the recipe of Roy et al. (1993) without addition of DIC. The artificial seawater was divided into two batches to which BICINE or HEPES buffer were added yielding final concentrations of 50 $\mu mol\,kg^{-1}$. Subsamples were taken and their pH was adjusted at room temperature to values of approximately 7.0, 8.0 and 8.4 by addition of NaOH. Subsamples were then incubated at temperatures of 11, 17 and $26°C$. For a measurement 8 ml of a seawater sample was filled into a

thermostated cuvette (set to the desired temperature), attached to a sectorfield multicollector mass spectrometer (Isoprime; GV Instruments, England) via a gas permeable membrane (0.01mm PTFE) inlet system. The area for gas exchange via the inlet system was about $24\ \mathrm{mm}^2$ and was located at the bottom of the cuvette. The cuvette was closed without headspace to prevent significant gas exchange between atmosphere and water, and was equipped with a magnetic stirring rod to enhance mixing. Manipulations of the carbonate system in the cuvette were carried out via a tiny hole drilled into the stopper. Changes in concentrations of $^{12}CO_2$ and $^{13}CO_2$, the only species of dissolved inorganic carbon (DIC) which are measured directly by the membrane inlet mass spectrometer (MIMS), upon disturbance of the seawater carbonate system were monitored continuously with a resolution of 0.1 s (carbon species without ^{13}C or ^{12}C notation will refer to the sum of both). The MIMS was calibrated for [CO_2] by injections of known amounts of $NaH^{12}CO_3$ ($\sim 99\%\ ^{12}C$) and $NaH^{13}CO_3$ ($\sim\ 99\%\ ^{13}C$) solutions (10 $\mathrm{mmol\,kg^{-1}}$) into the cuvette filled with 8 ml of 0.2 M HCl. As in such acidic solution DIC is only present as CO_2 the measured CO_2 recording can be directly converted into concentration. The CO_2 baseline was determined by injection of 20 μl of 10 M NaOH. This increased seawater pH to values at which [CO_2] is practically zero. As a single measuremtent did not exceed 10 minutes CO_2 consumption by the mass spectrometer through the membrane inlet system was negligible.

Special care was taken in determining the pH in all buffered seawater solutions. Known amounts (40 μl) of a $NaHCO_3$ solution (100 $\mathrm{mmol\,kg^{-1}}$) were added to these and subsequent equilibration in the CO_2 signal was monitored. The [CO_2] calibration of the MIMS was used to determine the DIC to CO_2 ratio (R_C) in equilibrium. Together with the dissociation constants of carbonic acid of Roy et al. (1993), the pH was calculated on the total scale (for details see Zeebe and Wolf-Gladrow (2001). The pH of the seawater buffered with HEPES or BICINE remained rather constant (± 0.05 units) upon $NaHCO_3$ addition which was checked independently with a pH meter.

Previously, similar experimental setups were used for estimation of the rate constants for the CO_2 to HCO_3^- inter-conversion (e.g. Badger et al., 1994; Sültemeyer et al., 1995).

Basically, CO_2 evolution was measured after injection of known amounts of a K_2CO_3 solution (100 $mmol\,kg^{-1}$) into DIC free seawater medium. In the alkaline K_2CO_3 solution (pH ~ 11) DIC is only present as CO_3^{2-} and HCO_3^- while CO_2 is practically zero. Hence, injection of such solution will result in a net conversion of CO_3^{2-} to HCO_3^- and finally to CO_2 in any seawater sample buffered at a pH lower than that of the K_2CO_3 solution. From the initial slope of the CO_2 evolution signal, monitored with the MIMS, the rate constants were then estimated. However, three assumptions regarding this procedure remain to be tested. First, the pH buffer is able to keep the pH constant on timescales of seconds recorded by the MIMS. Second, on these timescales the CO_3^{2-} and HCO_3^- pools are always in chemical equilibrium. And third, the initial reaction is dominated by the HCO_3^- to CO_2 conversion, so that the back-reaction can safely be ignored. The first two assumptions are discussed in sections 3.1, 3.2 and 3.4. As the third clearly poses a limitation a new method was developed which uses not only the initial slope but rather the entire CO_2 evolution curve, allowing explicitly for the back-reaction to take place. Practically, this is achieved by nonlinearly fitting a suitable equation to the measured CO_2 evolution curve leading to determination of the rate constants. However, these can also be assessed by adding known amounts of a solution in which DIC is mainly present in the form of CO_2. Such a solution was prepared by bubbling the artificial seawater described above with CO_2 at the desired temperature. Injection of this solution with a pH ~ 3.8 in any seawater sample, buffered at a pH higher than that, will result in a net conversion of CO_2 to HCO_3^-. Therefore, the MIMS will monitor a decrease in the CO_2 signal, the opposite reaction compared to K_2CO_3 addition.

2.2 The chemical background and the development of the fitting equations for addition of K_2CO_3 and CO_2 solutions

Inorganic carbon in aqueous solutions is predominantly present in three forms, CO_2(aq), HCO_3^- and CO_3^{2-}. The forth compound, true carbonic acid (H_2CO_3), constitutes less than

$0.1‰$ of the total dissolved inorganic carbon (DIC) and is therefore generally added to the CO_2(aq) pool, defining CO_2 as the sum of CO_2(aq) and H_2CO_3. Then, this system is characterized by two reactions. The first can be described as the relation between the CO_2 and HCO_3^- pools in equilibrium

$$K_1^* = \frac{[H^+][HCO_3^-]}{[CO_2]} = \frac{k_+}{k_-} \tag{1}$$

with K_1^* being the stoichiometric equilibrium constant and k_+ and k_- referring to the rate constants for the overall reaction of CO_2 to HCO_3^- and vice versa, respectively. The kinetics between these pools can then be described as

$$H_2O + CO_2 \underset{k_-}{\overset{k_+}{\rightleftharpoons}} HCO_3^- + H^+ \tag{2}$$

This overall reaction comprises several reaction pathways for the CO_2 to HCO_3^- interconversion, given by Eqs. 17 and 18. Please note that in Eq. 17 the reaction pathway via H_2CO_3 is implicity included (see Appendix). Rate constants are dependent on temperature and salinity, but the actual rate at which equilibrium will be restored after a disturbance in one pool also depends on pH (note the $[H^+]$ in Eq. 1). The second reaction in the carbonate system, the one between HCO_3^- and CO_3^{2-}, is virtually instantaneous compared to the reaction in Eq. 2, as it involves just protonation and deprotonation steps (see section 3.4 for details).

The ratio of [DIC] to CO_2 in equilibrium ($[CO_2]_{eq}$) as measured with the MIMS is defined as

$$R_C = \frac{[DIC]}{[CO_2]_{eq}} \tag{3}$$

From Eq. 2 follows that changes in $[CO_2]$ can be described as:

$$\frac{d[CO_2]}{dt} = +k_-[H^+][HCO_3^-] - k_+[CO_2] \quad (4)$$

this is a safe assumption on a timescale of seconds, as the HCO_3^- and CO_3^{2-} pools will be in equilibrium by the comparatively rapid reactions between them (see section 3.4 for details). As $[CO_2]$ is the only parameter which can be monitored online by the MIMS, ([DIC]-$[CO_2]$-$[CO_3^{2-}]$) is substituted for $[HCO_3^-]$. Now, the only unknown in a redistribution of the carbonate species is $[CO_3^{2-}]$. Note that [DIC] is always conserved, even when the relative contribution of the three carbonate species changes. If the pH buffer (HEPES, or BICINE) is able to keep the pH constant (this assumption will be investigated with a model described in section 2.4), $[CO_3^{2-}]$ can be described as a constant fraction f of $[HCO_3^-]$, yielding $[CO_3^{2-}] = f[HCO_3^-]$ (see 3.4 for details). Combining the last two equations gives

$$[HCO_3^-] = \frac{[DIC] - [CO_2]}{(1 + f)} \quad (5)$$

By substituting $[HCO_3^-]$ from Eq. 5 into Eq. 4 it follows that

$$\frac{d[CO_2]}{dt} = +k_-[H^+]\frac{[DIC] - [CO_2]}{(1 + f)} - k_+[CO_2] \quad (6)$$

Rearrangement with $\alpha = 1/(1 + f)$ yields

$$\frac{d[CO_2]}{dt} = -(\alpha k_-[H^+] + k_+)[CO_2] + \alpha k_-[H^+][DIC] \quad (7)$$

From here on, the paths for describing the CO_2 evolution curve upon addition of a K_2CO_3 or CO_2 solution split up. First, K_2CO_3 addition is considered. As right after the injection of a K_2CO_3 solution the reaction involving k_- will be the dominant one, k_+ is expressed in terms of k_- as described by equilibrium conditions in Eq. 1. Additionally, for convenience, the rate constant k_- is combined with $[H^+]$ giving $k_-^* = k_-[H^+]$ (Note that this is justified by the assumption that the pH is constant).

$$\frac{k_+}{k_-^*} = \frac{[HCO_3^-]_{eq}}{[CO_2]_{eq}} = \frac{\alpha([DIC] - [CO_2]_{eq})}{[CO_2]_{eq}} = \alpha(R_C - 1) \quad (8)$$

Substituting now k_+ in Eq. 7 it follows that

$$\frac{\mathrm{d}[\mathrm{CO_2}]}{\mathrm{d}t} = -\alpha \mathrm{R_C} k_-^* [\mathrm{CO_2}] + \alpha k_-^* [\mathrm{DIC}] \tag{9}$$

The general solution of the homogeneous version of Eq. 9 (i.e. [DIC]=0) is

$$[\mathrm{CO_2}](t) = \mathrm{A} \exp(-\alpha \mathrm{R_C}\, k_-^*\, t) \tag{10}$$

where A is a constant to be determined from the initial conditions. One arbitrary solution of the non-homogeneous equation is (this can usually be found by assuming $[\mathrm{CO_2}]$(t) = constant):

$$[\mathrm{CO_2}](t) = \frac{1}{\mathrm{R_C}} [\mathrm{DIC}] \tag{11}$$

Hence, the general solution of the non-homogeneous equation is:

$$[\mathrm{CO_2}](t) = \mathrm{A} \exp(-\alpha \mathrm{R_C}\, k_-^*\, t) + \frac{1}{\mathrm{R_C}} [\mathrm{DIC}] \tag{12}$$

Now A has to be determined from the initial condition $[\mathrm{CO_2}]$(t=0) = $[\mathrm{CO_2}]_0 = \mathrm{A} + \alpha[\mathrm{DIC}]/\alpha \mathrm{R_C}$. And thus

$$\mathrm{A} = [\mathrm{CO_2}]_0 - \frac{1}{\mathrm{R_C}} [\mathrm{DIC}] \tag{13}$$

which leads to

$$[\mathrm{CO_2}](t) = \left\{ [\mathrm{CO_2}]_0 - \frac{1}{\mathrm{R_C}} [\mathrm{DIC}] \right\} \exp(-\alpha \mathrm{R_C} k_-^* t) + \frac{1}{\mathrm{R_C}} [\mathrm{DIC}] \tag{14}$$

with $[\mathrm{CO_2}]_0$ being the initial $[\mathrm{CO_2}]$ prior to addition of a $\mathrm{K_2CO_3}$ solution. The constant $\mathrm{R_C}$ is determined with the MIMS as described above, and f can be calculated using the second dissociation constants of carbonic acid given by Roy et al. (1993). Then, Eq. 14 is fitted for k_-^* in a least square procedure to the observed $\mathrm{CO_2}$ evolution data upon $\mathrm{K_2CO_3}$ addition. From equilibrium conditions described in Eq. 1, k_+ can then be calculated as

$$k_+ = \frac{\mathrm{K_1^*} k_-^*}{[\mathrm{H^+}]} \tag{15}$$

with $k_- = k_-^*/[\mathrm{H}^+]$.

In principle, Eq. 14 is equally suitable for CO_2 addition. However, the first dominant reaction will be the conversion of CO_2 to HCO_3^-. Hence, k_+ is substituted for k_- in Eq. 7. Further rearrangement and solving of the resulting differential equation gives

$$[\mathrm{CO}_2](t) = \left\{[\mathrm{CO}_2]_0 - \frac{1}{\mathrm{R_C}}[\mathrm{DIC}]\right\}\exp(-\gamma k_+ t) + \frac{1}{\mathrm{R_C}}[\mathrm{DIC}] \tag{16}$$

with $\gamma = \mathrm{R_C}/(\mathrm{R_C} - 1)$.

2.3 The fitting procedure

Fitting of Eq. 14 and 16 to the observed CO_2 evolution curve ($^{12}\mathrm{CO}_2 + {}^{13}\mathrm{CO}_2$) upon addition of a $\mathrm{K}_2\mathrm{CO}_3$ or CO_2 solution is achieved by a least square minimization using the Levenberg-Marquardt method (Moré, 1977), yielding k_- or k_+, respectively. There are, however, always two processes influencing the CO_2 evolution curve in the first couple of seconds following a disturbance in the carbonate system, i.e. changes in the gas flow through the membrane and mixing of the DIC addition in the cuvette. This is accounted for by discarding the first couple of seconds and starting the fitting procedure from the inflection point (see Fig.1).

As stated earlier, a crucial prerequisite for the fitting equations is that the pH of the seawater is kept constant by the pH buffer throughout the measurement. Therefore, in the next section a model of the carbonate system in seawater is described to test this assumption.

2.4 The model of the carbonate system in seawater

A model similar to that of Zeebe and Wolf-Gladrow (2001) was developed, including all important reactions of the carbonate system in seawater. Additionally, a parameterization for the kinetics of different pH-buffers was added. Boron species, important constituents in natural seawater, are excluded because they are not contained in the artificial seawater used.The following reactions are considered (A denotes a proton acceptor, i.e. a pH buffer).

$$\mathrm{CO_2 + H_2O} \underset{k_{-1}}{\overset{k_{+1}}{\rightleftharpoons}} \mathrm{HCO_3^- + H^+} \tag{17}$$

$$\mathrm{CO_2 + OH^-} \underset{k_{-4}}{\overset{k_{+4}}{\rightleftharpoons}} \mathrm{HCO_3^-} \tag{18}$$

$$\mathrm{CO_3^{2-} + H^+} \underset{k_{-5}^{H^+}}{\overset{k_{+5}^{H^+}}{\rightleftharpoons}} \mathrm{HCO_3^-} \tag{19}$$

$$\mathrm{HCO_3^- + OH^-} \underset{k_{-5}^{OH^-}}{\overset{k_{+5}^{OH^-}}{\rightleftharpoons}} \mathrm{CO_3^{2-} + H_2O} \tag{20}$$

$$\mathrm{H_2O} \underset{k_{-6}}{\overset{k_{+6}}{\rightleftharpoons}} \mathrm{H^+ + OH^-} \tag{21}$$

$$\mathrm{AH} \underset{k_{-a}}{\overset{k_{+a}}{\rightleftharpoons}} \mathrm{A^- + H^+} \tag{22}$$

It is noted that, what is referred to as k_+ or k_- in Eq. 2 must not be confused with k_{+1} or k_{-1} in Eq. 17. The former are the rate constants for the overall reactions between the $\mathrm{CO_2}$ and $\mathrm{HCO_3^-}$ pools in this coupled chemical system. The values for the different reaction rate constants are given in Tab.1. The set of differential equations therefore reads

$$\begin{aligned}
\frac{\mathrm{d}[\mathrm{CO_2}]}{\mathrm{d}t} &= +(k_{-1}[\mathrm{H^+}] + k_{-4})[\mathrm{HCO_3^-}] \\
&\quad -(k_{+1} + k_{+4}[\mathrm{OH^-}])[\mathrm{CO_2}] \qquad (23) \\
\frac{\mathrm{d}[\mathrm{HCO_3^-}]}{\mathrm{d}t} &= +(k_{+1} + k_{+4}[\mathrm{OH^-}])[\mathrm{CO_2}] \\
&\quad -(k_{-1}[\mathrm{H^+}] + k_{-4})[\mathrm{HCO_3^-}] \\
&\quad +(k_{+5}^{\mathrm{H^+}}[\mathrm{H^+}] + k_{-5}^{\mathrm{OH^-}})[\mathrm{CO_3^{2-}}] \\
&\quad -(k_{-5}^{\mathrm{H^+}} + k_{+5}^{\mathrm{OH^-}}[\mathrm{OH^-}])[\mathrm{HCO_3^-}] \qquad (24) \\
\frac{\mathrm{d}[\mathrm{CO_3^{2-}}]}{\mathrm{d}t} &= +(k_{-5}^{\mathrm{H^+}} + k_{+5}^{\mathrm{OH^-}}[\mathrm{OH^-}])[\mathrm{HCO_3^-}]
\end{aligned}$$

$$
\begin{aligned}
& -(k_{+5}^{\mathrm{H}^+}[\mathrm{H}^+] + k_{-5}^{\mathrm{OH}^-})[\mathrm{CO}_3^{2-}] && (25)\\
\frac{\mathrm{d}[\mathrm{H}^+]}{\mathrm{d}t} &= +k_{+1}[\mathrm{CO}_2] - k_{-1}[\mathrm{H}^+][\mathrm{HCO}_3^-] \\
& \quad +k_{-5}^{\mathrm{H}^+}[\mathrm{HCO}_3^-] - k_{+5}^{\mathrm{H}^+}[\mathrm{H}^+][\mathrm{CO}_3^{2-}] \\
& \quad +k_{+6} + k_{-6}[\mathrm{H}^+][\mathrm{OH}^-] \\
& \quad +k_{+\mathrm{a}}[\mathrm{AH}] - k_{-\mathrm{a}}[\mathrm{H}^+][\mathrm{A}^-] && (26)\\
\frac{\mathrm{d}[\mathrm{OH}^-]}{\mathrm{d}t} &= +k_{-4}[\mathrm{HCO}_3^-] - k_{+4}[\mathrm{OH}^-][\mathrm{CO}_2] \\
& \quad -k_{+5}^{\mathrm{OH}^-}[\mathrm{OH}^-][\mathrm{HCO}_3^-] + k_{-5}^{\mathrm{OH}^-}[\mathrm{CO}_3^{2-}] \\
& \quad +k_{+6} + k_{-6}[\mathrm{H}^+][\mathrm{OH}^-] && (27)\\
\frac{\mathrm{d}[\mathrm{AH}]}{\mathrm{d}t} &= +k_{-\mathrm{a}}[\mathrm{H}^+][\mathrm{A}^-] - k_{+\mathrm{a}}[\mathrm{AH}] && (28)\\
\frac{\mathrm{d}[\mathrm{A}^-]}{\mathrm{d}t} &= +k_{+\mathrm{a}}[\mathrm{AH}] - k_{-\mathrm{a}}[\mathrm{H}^+][\mathrm{A}^-] && (29)
\end{aligned}
$$

This set of coupled differential equations was integrated numerically with the matlab 'ode15s' solver for 'stiff' problems (Shampine and Reichelt, 1997). These equations are called 'stiff' because the coupled system exhibits extremely different relaxation times (Zeebe et al., 1999).

3 pH-buffered seawater systems

Relaxation times of the carbonate system in pH-buffered seawater upon disturbance depends on the type and amplitude of the disturbance and most importantly on the kinetics of the pH buffer. However, rate constants for the protonation and deprotonation of widely used pH buffers are not available, and a general assumption is that the two reactions are almost instantaneous or at least sufficiently fast compared to other reactions that they can be ignored. In the following considerations, the rate constants for the pH buffer (i.e. its speed) were chosen to be about 100 times slower than the comparatively rapid CO_3^{2-} to HCO_3^- inter-conversion.

3.1 K_2CO_3 versus CO_2 addition

In Fig.2 the response of the carbonate system upon addition of a K_2CO_3 solution to low-DIC (5 μmol kg^{-1}), pH- buffered seawater is shown (see caption of Fig.2 for details). The amount of solution added was chosen to result in a 500 μmol kg^{-1} increase in DIC in the seawater sample. This setup resembles those previously used to determine k_- from the initial slope of CO_2 evolution (e.g. Badger et al., 1994; Sültemeyer et al., 1995). The re-equilibration in the carbonate system following the addition of a K_2CO_3 solution includes three characteristic timescales.

Timescale 10^{-10} to 10^{-5} seconds

Injection of a highly alkaline K_2CO_3 solution (pH $\sim$ 11) into seawater of pH 8 significantly increases the OH^- concentration as illustrated by the drop in pOH, i.e. the negative common logarithm of $[OH^-]$ in analogy to pH (Fig. 2 E). This decrease in pOH leads to an immediate increase in pH (Fig. 2F) as the OH^- added consumes the H^+ present. Also shortly after injection of the K_2CO_3 solution, the conversion of the added CO_3^{2-} to HCO_3^- begins (Fig. 2B,C). In this reaction CO_3^{2-} combines with water giving HCO_3^- and OH^- (compare Eq. 20) leading to a concomitant decrease in pOH (Fig. 2 E). Why this reaction is dominating rather than the competing one, in which CO_3^{2-} combines with H^+ (Eq. 19), can easily be understood by comparing the relevant terms, $k_{-5}^{OH^-}$ and $k_{+5}^{H^+}[H^+]$, in Eq. 25. As $k_{-5}^{OH^-}$ is about seven orders of magnitude larger than $k_{+5}^{H^+}[H^+]$, HCO_3^- is formed almost entirely by the combination of CO_3^{2-} with water. The decrease in pOH is not a mirror image of the increase in pH, indicating that the ion product of water (Eq. 21) is not constant on this timescale. The reason is that the conversion of CO_3^{2-} to HCO_3^- is slightly faster than the combination reaction of H^+ and OH^-. Hence, the increase in pH lags behind the decrease in pOH. Furthermore, the protonated form of the pH buffer is already starting to release protons to compensate for the loss of H^+, dampening the increase in pH. This initial pH-buffering, however, is not visible in $[AH]$ (Fig. 2D) as the amount of H^+ released by the protonated form of the buffer is about six orders of magnitude lower than the buffer's con-

centration (note that $[H^+]$ is in the nanomolar and [AH] in millimolar range). A temporary pH plateau of about 8.35 is reached after about 10^{-6} seconds. The height of this plateau depends on the rate constants of the pH buffer chosen. Increasing the rate constants increases the speed of the buffer and the temporary plateau will be closer to the final equilibrium value of about pH 8.0.

Timescale 10^{-5} to 10^{-1} seconds

The comparatively massive proton release by the protonated form of the buffer (Fig. 2D) yields to both, an increase of pOH (due to protonation of OH^-) and a decrease of pH (Fig. 2E,F). Hence, a second phase of CO_3^{2-} to HCO_3^- conversion is initiated (Fig. 2B,C). A temporary quasi steady-state between all these pools is established after about 10^{-2} seconds (Fig.2B-F).

Timescale larger than 10^{-1} seconds

It is by now that the HCO_3^- and CO_2 pools start to re-equilibrate (Fig.2A,B), owing to the slow inter-conversion rate. Again, the protonated form of the pH-buffer re-delivers the protons consumed by the conversion of HCO_3^- to CO_2 (Fig.2D). However, as the pH-buffer was assumed orders of magnitude faster than the HCO_3^- to CO_2 conversion and the amount of protons released is small compared to those released due to the conversion of CO_3^{2-} to HCO_3^-, the pH and the pOH stay constant during this last phase of re-equilibration.

In this configuration (see caption of Fig.2 for details), the pH-buffer was able to keep the pH constant on a timescale of seconds (Fig.2L), which is a prerequisite for the fitting procedure. However, it is obvious that this depends on the actual rate constants assumed for the protonation/deprotonation reactions of the buffer (i.e. its speed). When adding a K_2CO_3 solution to a seawater system as described above, the pH buffer has to release far more protons consumed in the rapid conversion of CO_3^{2-} to HCO_3^- than from the slow reaction of HCO_3^- to CO_2.

This is opposite to addition of a CO_2 solution (Fig.3), where the pH buffer has to accept more protons from the slow reaction. Again, there are three characteristic timescales for the re-equilibration.

Timescale 10^{-10} to 10^{-5} seconds

Injection of a CO_2 solution, yielding a final DIC concentration of 500 $\mu mol\,kg^{-1}$, in the buffered seawater (the preparation of such solution is described in section 2.1), causes an initial drop in pH (Fig.3F) as such a solution is highly acidic (pH ~ 3.8). Almost instantly the unprotonated form of the buffer starts to accept the H^+ added, leading to an increase in pH and [AH], the protonated form of the buffer (Fig. 3D). Please note that the total increase in pH from about 5.5 to 8.0 corresponds to a decrease in $[H^+]$ of about 3 $\mu mol\,kg^{-1}$. This is difficult to detect in the simultaneous increase in [AH] as, again, the buffer concentration is about four orders of magnitude higher than the amount of protons accepted. pH reaches a temporary plateau of about 8.0 already before 10^{-5} seconds. The time required to achieve this pH which is close to equilibrium conditions crucially depends on the rate constants of the buffer, i.e. its speed. Already shortly after the initial increase in pH there is an increase in pOH. This is partly caused by the combination of HCO_3^- with OH^- yielding CO_3^{2-} (Eq. 20) because the injected CO_2 solution contains a small amount of HCO_3^-(~ 2.5 $\mu mol\,kg^{-1}$). Hence, part of the HCO_3^- (~ 0.2 $\mu mol\,kg^{-1}$) added convert to CO_3^{2-} resulting in the increase in pOH. Also responsible for the increase in pOH is the combination of the H^+ added with the OH^- present. However, the increase in pOH is not as pronounced as the increase in pH, indicating that the ion product of water on this timescale is not constant. This can be easily understood when comparing the equations competing for the H^+ added which are the formation of water with OH^- (Eq. 21) and the combination with the unprotonated form of the buffer A^- (Eq. 22). The relevant terms for these reactions given in Eq. 26 are $k_{-6}[OH^-]$ and $k_{-a}[A^-]$, respectively (note that $[H^+]$ is the same for both of them) . As $k_{-a}[A^-]$, is about 200 times larger than $k_{-6}[OH^-]$ the increase in pH is dominated by the protonation of the buffer and not by OH^- consumption. Hence, the increase in pH is hardly reflected in pOH.

Timescale 10^{-5} to 10^{-1} seconds

The imbalance between the OH^- and H^+ pools start to re-equilibrate and the pOH drops to its initial value whereas the pH is kept constant by the buffer. Again, a temporary quasi

steady-state between all these pools is established after about 10^{-2} seconds (Fig. 3B-F).

Timescale larger than 10^{-1} seconds

The slow conversion reaction of CO_2 to HCO_3^- is then initiated at about 10^{-1} seconds leading to a slight drop in pH and a concomitant increase in pOH compared to conditions prior to injection. And again, in this configuration (see caption of Fig.3 for details) the buffer has been able to keep the pH very close to equilibrium values (Fig.3L). Basically, if the protonation reaction of the buffer is faster than the conversion of CO_2 to HCO_3^- it can keep up with the release of protons by this process.

3.2 Influence of the pH buffer kinetics on changes in pH

As outlined above, a prerequisite for fitting of the CO_2 evolution curve upon addition of a K_2CO_3 or CO_2 solution (Fig.2G and 3G, respectively) is that the pH can be considered constant. The rate constants for the protonation and deprotonation of certain pH buffers, however, are not known. Therefore, their influence on pH, following the addition of a K_2CO_3 or CO_2 solution, was investigated by varying the rate constants of the pH buffer in the seawater carbonate system model. More specifically, the time was determined after which the pH reached a constant value. For that, a critical threshold was introduced of 0.05 pH units which was the maximum pH drift from steady state conditions after injection of a K_2CO_3 or CO_2 solution, observed in all measurements. Calculated times to reach that threshold depend to a small degree on whether K_2CO_3 or CO_2 is added (Fig.4A/B), but mostly on the pH of the seawater. The differences in pK values between HEPES and BICINE are negligible for the following considerations. The time to reach constant pH values is faster the lower the pH is regardless whether K_2CO_3 (Fig. 4A) or CO_2 (Fig. 4B) is added. When adding K_2CO_3 the protonated form of the pH buffer (AH) releases protons to compensate for the loss of H^+ consumed by the conversion of CO_3^{2-} to HCO_3^-. Hence, at low pH the initial concentration of AH is higher compared to high pH and the re-equilibration is faster. On the other hand, when adding CO_2 the unprotonated form of

the buffer accepts the protons generated by the conversion of CO_2 to HCO_3^-. Hence at low pH, this protonation is enhanced by the increased [H^+].

It seems that neither K_2CO_3 nor CO_2 addition bears any advantages for measuring the carbon dioxide to bicarbonate inter-conversion rates. However, the time to reach constant pH values is not only bound to buffer kinetics but also to the amplitude of the disturbance. Basically, the lower the amount of K_2CO_3 or CO_2 addition, the lower is the disequilibrium in $[H^+]$ the buffer has to cope with. Injecting a small amount of CO_2 and measuring its disappearance into the HCO_3^- and CO_3^{2-} pools is possible, while the same amount injected as K_2CO_3 will result in almost no detectable change in [CO_2] (note that in seawater, with a pH ranging from 7-9, the dominant DIC form is HCO_3^- while the MIMS is only able to detect CO_2 and the two other DIC species have to be deduced). This is illustrated in Fig.3A and 2A, where the change in [CO_2] due to a 500 $\mu mol\,kg^{-1}$ addition of CO_2 is about 500 $\mu mol\,kg^{-1}$, while the addition of 500 $\mu mol\,kg^{-1}$ of K_2CO_3 results in a change in [CO_2] of only about 4 $\mu mol\,kg^{-1}$. Therefore, it is feasible to work with much lower additions of CO_2 compared to K_2CO_3, and the influence of the buffer kinetics on the time to reach constant pH values is becoming less critical (when adding 15 $\mu mol\,kg^{-1}$of CO_2 instead of 500 $\mu mol\,kg^{-1}$ (compare Fig.4A) the pH is constant from the first second, regardless of seawater pH and buffer kinetics). Hence, the experiments were carried out with small amounts of CO_2 injected into seawater buffered at different pH values at certain temperatures, and the resulting decrease in [CO_2] was monitored and fitted with Eq. 16 (Fig.1).

3.3 The rate constants for CO_2 to HCO_3^- inter-conversion at different temperatures and pH

The k_+ values resulting from fitting the CO_2 evolution upon adding small amounts of CO_2 (yielding a final concentration of about 15 $\mu mol\,kg^{-1}$) to seawater buffered at pH values ranging from 7 to 9 and temperatures of 11, 16 and $26°C$ are shown in Fig.5. Also shown

are calculated k_+ values from the second part of Eq. 23 with $k_+ = k_{+1} + k_{+4}[\mathrm{OH^-}]$, the combination of reactions 17 and 18 (see Appendix for details). Because application of k_{+4} values, determined previously (Zeebe and Wolf-Gladrow, 2001) by fitting the original data from Johnson (1982), did not match the measurements (especially at $26°\mathrm{C}$), k_{+4} has been refitted in this study (see Tab. 1 for details). Measured and calculated k_+ values are in good agreement in the pH range from 7 to 8.5, regardless whether HEPES or BICINE was used as pH buffer. This clearly indicates that both buffers are able to keep the pH constant under the experimental conditions tested. Above a pH of 8.5, however, correlation between measured and calculated values becomes less clear. One reason is that the error in pH determination with the MIMS increases with rising pH, because the contribution of $\mathrm{CO_2}$ to DIC decreases. Hence, after additions of known amounts of $\mathrm{NaHCO_3}$ to determine the $\mathrm{CO_2}$/DIC ratio, the change in $[\mathrm{CO_2}]$ will get close to the noise in the $\mathrm{CO_2}$ signal detected by the MIMS. Under these circumstances the pH cannot be calculated reliably anymore.

Furthermore, k_+ increases with rising temperature and pH (Fig.5). High pH values correspond to increased $[\mathrm{OH^-}]$ and therefore the reaction of $\mathrm{CO_2} + \mathrm{OH^-} \rightarrow \mathrm{HCO_3^-}$ is faster compared to low pH and k_+ is larger. Strictly speaking, the $\mathrm{CO_2}$ evolution is characterized not by k_+ alone, but by $\gamma\, k_+$ (see Eq. 16). But at pH values above 7, $\gamma = R/(R-1)$ is almost equal to one and can be neglected (also compare solid line in Fig.5 with Fig.6A) From equilibrium conditions described in Eq. 1, it follows that $k_- = k_+/\mathrm{K_1^*}$.

From Fig.1 it becomes evident that interpretation of initial $\mathrm{CO_2}$ slopes recorded by the MIMS is difficult. This is due to the fact that in the first couple of seconds, following a disturbance, homogeneous mixing in the cuvette and changing gas fluxes through the membrane mask the kinetics in the carbonate system. Thus, the initial slope of the $\mathrm{CO_2}$ evolution curve (defined as the maximum slope) is always shallower than the slope that would be observed in an ideal setup. This can only be accounted for by fitting the $\mathrm{CO_2}$ signal from the inflection point to a suitable equation, which explicitly incorporates the forward and backward reactions between the $\mathrm{CO_2}$ and $\mathrm{HCO_3^-}$ pools. Hence, determination of k_- from the initial slope as proposed previously underestimates k_- (and therefore k_+).

We estimate this error to be up to 50% depending on temperature, pH and MIMS setup.

3.4 Theoretical remarks on $\mathbf{k_+ = k_{+1} + k_{+4}[OH^-]}$

It can be shown that the conversion of CO_2 to HCO_3^- on time scales monitored by the MIMS (i.e. seconds) is given by the slowest process, which is characterized by the relaxation time τ:

$$\tau = -\frac{1}{\lambda} \tag{30}$$

$$\lambda = -\frac{1}{2}\left(k_- + k_+ + \overline{k}_- + \overline{k}_+\right) + \frac{1}{2}\sqrt{\left(k_- + k_+ - \overline{k}_- - \overline{k}_+\right)^2 + 4k_-\overline{k}_-} \quad , \tag{31}$$

with $k_- = k_{-1}[H^+] + k_{-4}$, $k_+ = k_{+1} + k_{+4}[OH^-]$, $\overline{k}_- = k_{-5}^{H^+} + k_{+5}^{OH^-}[OH]$, and $\overline{k}_+ = k_{+5}^{H^+}[H^+] + k_{-5}^{OH^-}$. Because of the rapid interconversion of HCO_3^- and CO_3^{2-}, the exact solution for $[CO_2](t)$ at constant pH can excellently be approximated by Eq. (16), with

$$\tau \approx \frac{1}{\gamma k_+} \quad . \tag{32}$$

as shown in Fig.6B.

In summary, if the pH buffer is able to keep the pH constant upon disturbance in the carbonate system, the rate constants for the CO_2 to HCO_3^- inter-conversion, k_+ and k_-, can be calculated as $k_+ = k_{+1} + k_{+4}[OH^-]$ and $k_- = k_+ K_1^*$ (see Tab.1 for details on the rate constants).

4 Summary and conclusions

Mass spectrometric and ^{14}C disequilibrium techniques are widely used to assess modes and efficiencies of inorganic carbon acquisition in marine phytoplankton (Badger et al., 1994; Espie and Colman, 1986). These methods rely on the exact knowledge of the rate constants

for the CO_2 to HCO_3^- interconversion reaction, which depend on pH, temperature and salinity. In this study, a method is presented for measuring these rate constants, known as k_+ and k_-, by means of membrane inlet mass spectrometry (MIMS). For the two pH buffers tested (HEPES and BICINE) it was shown that measured rate constants are in good agreement with calculated values for k_+ and k_- in a pH range of 7 to 8.5 and at temperatures from 10 to $25°C$. Moreover, it was shown that the method proposed previously to determine the CO_2 to HCO_3^- interconversion rate constants tends to significantly underestimate them. Therefore, it is recommended that in future applications k_+ and k_- are measured or calculated as described above.

5 Acknowledgements

We thank K.-U. Richter for technical assistance and A. Körtzinger for vital discussions regarding the carbonate system. This work was funded by the Deutsche Forschungsgemeinschaft (DFG) project #TH 744/2-1.

References

Badger, M. R., Palmqvist, K., Yu, J.-W., 1994. Measurement of CO_2 and HCO_3^- fluxes in cyanobacteria and microalgae during steady-state photosynthesis. Physiol. Plantarum 90, 529–536.

Beynon, R. J., Easterby, J. S., 1996. Buffer Solutions: The Basics. Oxford University Press.

Burkhardt, S., Amoroso, G., Riebesell, U., Sültemeyer, D., 2001. CO_2 and HCO_3^- uptake in marine diatoms acclimated to different CO_2 concentrations. Limnol. Oceanogr. 46, 1378–1391.

Cooper, T. G., Filmer, D., Wishnick, M., Lane, M. D., 1969. The Active Species of "CO_2"Utilized by Riboluse Diphosphate Carboxylase. J. Biol. Chem. 244, 1081–1083.

Davies, C. W., 1962. Ion Association. Butterworths.

DOE, 1994. Handbook of Methods for the Analysis of the Various Parameters of the Carbon Dioxide System in Seawater, version 2. A. G. Dickson and C. Goyet, eds., ORNL/CDIAC-74.

Eigen, M., 1964. Proton transfer, acid-base catalysis, and enzymatic hydrolysis. Angew. Chem. Int. Ed. Eng. 3, 1–19.

Eigen, M., Kustin, K., Maass, G., 1961. Die Geschwindigkeit der Hydratation von SO_2 in wässriger Lösung. Z. Phys. Chem. NF 30, 130–136.

Espie, G. S., Colman, B., 1986. Inorganic carbon uptake during photosynthesis. I. A theoretical analysis using the isotope disequilibrium technique. Plant. Physiol. 80, 863–869.

Field, C. B., Behrenfeld, M. J., Randerson, J. T., Falkowski, P., 1998. Primary Production of the Biosphere: Integrating Terrestrial and Oceanic Components. Science 281, 237–240.

Good, N. E., Winter, W., Conolly, T. N., Izawa, S., Singh, R., 1966. Hydrogen ion buffers for biological research. Biochem. 5, 467–477.

Houghton, J. T., Meira Fiho, L. G., Bruce, J., Lee, H., Callander, B. A., Haites, E., Harris, N., Maskell, K. (Eds.), 1995. Climate Change 1994. Cambridge Univ. Press, Cambridge, Ch. Radiative Forcing of Climate Change and an Evaluation of the IPCC IS92 Emission Scenairo.

Johnson, K. S., 1982. Carbon dioxide hydration and dehydration kinetics in seawater. Limnol. Oceanogr. 27, 849–855.

Moré, J. J., 1977. The Levenberg-Marquardt Algorithm: Implementation and Theory. In: Watson, G. A. (Ed.), Numerical Analysis, Lecture Notes in Mathematics 630. Springer. pp. 105-116.

Rost, B., Richter, K.-U., Riebesell, U., Hansen, P. J., 2005. Inorganic carbon acquisition in red-tide dinoflagellates. Plant Cell Environ., in press.

Rost, B., Riebesell, U., Burkhardt, S., Sültemeyer, D., 2003. Carbon acquisition of bloom-forming marine phytoplankton. Limnol. and Oceanogr., 55–67.

Roy, R. N., Roy, L. N., Lawson, M., Vogel, K. M., Porter-Moore, C., Pearson, T., Good, C. E., Millero, F. J., Cambel, D. J., 1993. Determination of the ionization constants of carbonic acid in seawater in salinities 5 to 45 and temperatures 0 to $45^{\circ}\mathrm{C}$. Mar. Chem. 44, 249–267.

Sabine, C. L., Feely, R. A., Gruber, N., Key, R. M., Lee, K., Bullister, J. L., Wanninkhof, R., Wong, C. S., Wallace, D. W. E., Tilbrook, B., Millero, F. J., Peng, T.-H., Kozyr, A., Ono, T., Rios, A. F., 2004. The Oceanic Sink for Anthropogenic CO_2. Science 305, 367–371.

Shampine, L. F., Reichelt, M. W., 1997. The matlab ODE suite. SIAM J. Sci. Comput. 18, 1–22.

Sültemeyer, D., Price, G. D., Yu, J.-W., Badger, M. R., 1995. Characterization of carbon dioxide and bicarbonate transport during steady-state photosynthesis in the marine cyanobacterium Synechococcus strain PCC7002. Planta 197, 597–607.

Thoms, S., Pahlow, M., Wolf-Gladrow, D., 2001. Concentrating Mechanisms in Chloroplasts of Eukaryotic Algae. J. theor. Biol. 208, 295–313.

Thoms, S., Wolf-Gladrow, D. A., 2005. Relaxation time constants of the carbonate system at steady states. in prep.

Zeebe, R. E., Wolf-Gladrow, D., 2001. CO_2 in seawater: equilibrium, kinetics, isotopes. Vol. 65 of Elsevier Oceanography Series. Elsevier.

Zeebe, R. E., Wolf-Gladrow, D. A., Jansen, H., 1999. On the time required to establish chemical and isotopic equilibrium in the carbon dioxide system in seawater. Mar. Chem. 65, 135–153.

Appendix

The reaction scheme for the hydration of carbon dioxide can be formulated as (cf. Eigen et al. (1961))

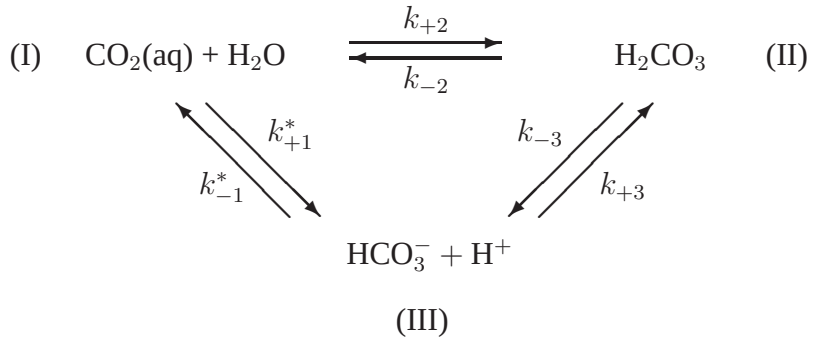

in which aqueous carbon dioxide (CO_2(aq)) is either hydrated in the transition of (I) to (III) or via H_2CO_3 in the transition of (I) to (II) to (III). The overall hydration and dehydration reaction as measured by Johnson (1982) is then given as

$$CO_2 + H_2O \underset{k_{-1}}{\overset{k_{+1}}{\rightleftharpoons}} H^+ + HCO_3^- \tag{A-1}$$

with CO_2 denoting the sum of CO_2(aq) and H_2CO_3, and k_{+1} and k_{-1} being the effective rate constants. As the reaction between carbonic acid and bicarbonate (II) $\rightleftharpoons$ (III) is diffusion-controlled, it is practically instantaneous and equilibrium can be assumed as

$$[H^+][HCO_3^-] = K^*_{H_2CO_3}[H_2CO_3] \tag{A-2}$$

with $K^*_{H_2CO_3}$ being the acidity constant of true carbonic acid. Hence, k_{+1} and k_{-1} of the overall hydration/dehydration reaction are given by

$$\mathrm{k}_{+1} := \mathrm{k}^{*}_{+1} + \mathrm{k}_{+2} \tag{A-3}$$

and

$$\mathrm{k}_{-1} := \mathrm{k}^{*}_{-1} + \frac{\mathrm{k}_{-2}}{\mathrm{K}^{*}_{\mathrm{H_2CO_3}}} \tag{A-4}$$

While the hydration/dehydration reaction is dominat at low pH, at high pH the reaction via hydroxylation is favored as

$$\mathrm{CO_2} + \mathrm{OH^-} \underset{k_{-4}}{\overset{k_{+4}}{\rightleftharpoons}} \mathrm{HCO_3^-} \tag{A-5}$$

The combination of the hydration/dehydration and the hydroxylation reaction gives the overall inter-conversion reaction of $\mathrm{CO_2}$ to $\mathrm{HCO_3^-}$ and vice versa as

$$\mathrm{H_2O} + \mathrm{CO_2} \underset{k_{-}}{\overset{k_{+}}{\rightleftharpoons}} \mathrm{HCO_3^-} + \mathrm{H^+} \tag{A-6}$$

with

$$k_{+} := k_{+1} + k_{+4}[\mathrm{OH^-}] \tag{A-7}$$

and

$$k_{-} := k_{-1}[\mathrm{H^+}] + \mathrm{k}_{-4} \tag{A-8}$$

Note that the overall reaction (Eq. A-6) must not be confused with that given Eq. A-1 as it incorporates also the hydroxylation pathway.

Table 4: Rate constants and their respecitve check values used in this study[a]

Rate constant	Check Value T=298.15K, S=35	Dependence on T and S	Reference
k_{+1}	$3.71 \times 10^{-2}\,\mathrm{s}^{-1}$	$\exp(1246.98 - 6.19 \times 10^4/\mathrm{T} - 183.0\ln(\mathrm{T}))$	1
k_{-1}	$2.67 \times 10^4\,\mathrm{kg\,mol}^{-1}\,\mathrm{s}^{-1}$	k_{+1}/K_1^*	calculated
k_{+4}	$2.23 \times 10^3\,\mathrm{kg\,mol}^{-1}\,\mathrm{s}^{-1}$	$\mathrm{A}_4\exp(-90166.83/(\mathrm{RT}))/\mathrm{K}_\mathrm{W}^*$	refitted from 1
k_{-4}	$9.71 \times 10^{-5}\,\mathrm{s}^{-1}$	$k_{+4} \times \mathrm{K}_\mathrm{W}^*/\mathrm{K}_1^*$	calculated
$k_{+5}^{\mathrm{H}^+}$	$5.0 \times 10^{10}\,\mathrm{kg\,mol}^{-1}\,\mathrm{s}^{-1}$	none	2
$k_{-5}^{\mathrm{H}^+}$	$59.44\,\mathrm{s}^{-1}$	$k_{+5}^{\mathrm{H}^+} \times \mathrm{K}_2^*$	calculated
$k_{+5}^{\mathrm{OH}^-}$	$6.0 \times 10^9\,\mathrm{kg\,mol}^{-1}\,\mathrm{s}^{-1}$	6×10^9	2
$k_{-5}^{\mathrm{OH}^-}$	$3.06 \times 10^5\,\mathrm{s}^{-1}$	$k_{+5}^{\mathrm{OH}^-} \times \mathrm{K}_\mathrm{W}^*/\mathrm{K}_2^*$	calculated
k_{+6}	$1.40 \times 10^{-3}\,\mathrm{mol\,kg}^{-1}\,\mathrm{s}^{-1}$	none	2
k_{-6}	$2.31 \times 10^{10}\,\mathrm{kg\,mol}^{-1}\,\mathrm{s}^{-1}$	$k_{+6}/\mathrm{K}_\mathrm{W}^*$	calculated
$k_{+\mathrm{a}}$	s^{-1}	$k_{-\mathrm{a}} \times 10^{-\mathrm{pK_A}}$	calculated
$k_{-\mathrm{a}}$	$\mathrm{kg\,mol}^{-1}\,\mathrm{s}^{-1}$	$k_{+5}^{\mathrm{H}^+}/\mathrm{f_a}$	varied

[a] Ref. 1 refers to the work of Johnson (1982), while Ref. 2 refers to the work of Eigen (1964) (see Zeebe and Wolf-Gladrow (2001), p. 105 for a detailed discussion). k_{+4} has been refitted in this study, with $\mathrm{A}_4 = 499002.24 \times \exp(4.2986 \times 10^{-4}\,\mathrm{S}^2 + 5.75499 \times 10^{-5}\,\mathrm{S})$, with S representing salinity because otherwise measured and calculated values for k_+ did not match well, especially at high temperature. $p\mathrm{K_A}$ denotes the $p\mathrm{K_A}$ value of the pH buffer used, i.e. HEPES: $\mathrm{pK} = 7.94 - 0.014 \times (\mathrm{T} - 273.15)$ and BICINE: $\mathrm{pK} = 8.82 - 0.018 \times (\mathrm{T} - 273.15)$ after Good et al. (1966), with T representing temperature in Kelvin. These are values extrapolated to zero ionic strength (see Beynon and Easterby (1996) for details). In the calculations, however, they have been adjusted to the correct ionic strength with the Davies approximation (Davies, 1962). Rate constants for the pH buffer were varied by applying a factor $\mathrm{f_a}$ to $k_{-\mathrm{a}}$. R denotes the universal gas constant of 8.31451 J/mol, K_W^* the equilibrium constant for the ion product of water calculated after DOE (1994), and K_1^* and K_2^* the first and second dissociation constants of carbonic acid calculated according to Roy et al. (1993). The corresponding reactions for the different rate constants are listed in Eqs. 17-22.

Figure 1 Example for the measurement of the CO_2 ($^{12}CO_2 + {}^{13}CO_2$) evolution curve as monitored with the MIMS upon an addition of $\sim 14\ \mu mol\,kg^{-1}$ CO_2, and the curve fitting procedure. The solid line depicts the change in $[CO_2]$ as measured by the MIMS and the dashed line the CO_2 evolution curve as predicted by Eq. 16 after the fitting procedure described in section 2.3. The dot marks the inflection point at which the fitting of the solid line is started. The dashed line increasing constantly prior to that point is the theoretical decline in $[CO_2]$ (Eq. 16) which would be observed in an ideal situation, i.e. right at time zero, the injected CO_2 is mixed homogeneously in the cuvette and detected instantly by the MIMS. To illustrate these processes the theoretical CO_2 evolution curve has been modified by multiplication with two exponential terms representing mixing and changing gas flow through the membrane (dashed line starting at the initial $[CO_2]$ at time zero). This theoretical CO_2 evolution curve resembles the measured very well and demonstrates that the fitting procedure after the inflection point is not biased by mixing and changing gas flow through the membrane. The two solid triangles next to the CO_2 evolution curves illustrate the respective slopes at time zero and after the inflection point, at which the back-reaction from HCO_3^- to CO_2 is much higher and $[CO_2]$ is much lower, resulting in a shallower slope. In the case shown, the temperature was $17°C$, the seawater pH was ~ 8 and the pH buffer used was HEPES.

Figure 2 Reaction kinetics in pH-buffered seawater upon addition of a K_2CO_3 solution (at t equals zero), leading to an increase in DIC of 500 $\mu mol\,kg^{-1}$ in the seawater sample, as calculated by the numerical model described in section 2.4. The pH buffer was set to 50 mM of HEPES, temperature to $15°C$, Salinity to 35, pH to 8.0, initial DIC to 5 $\mu mol\,kg^{-1}$ and k_{-a} to $k_{+5}^{H^+}/100$. AH denotes the protonated form of the buffer. Illustrated in **A-F** are the changes of $[CO_2]$, $[HCO_3^-]$, $[CO_3^{2-}]$, [AH], pOH and pH (on the total scale) against time on a logarithmic scale, while in **G-L** the same reactions against time are shown on a linear scale. Grey shaded areas depict different timescales ranging from 10^{-10} to 10^{-5}, 10^{-5} to 10^{-1} and 10^{-1} to 400 seconds (light, intermediate and dark grey, respectively). The

arrows denote changes from equilibrium due to the disturbance by the addition of a K_2CO_3 solution.

Figure 3 Reaction kinetics in pH-buffered seawater upon addition of a CO_2 solution (at t equals zero), leading to an increase in DIC of 500 $\mu mol\,kg^{-1}$ in the seawater sample, as calculated by the numerical model described in section 2.4. For details see Fig. caption 2.

Figure 4 Influence of the pH buffer kinetics on the pH re-equilibration time as predicted by the numerical model described in section 2.4. The pH buffer was set to 50 mM of HEPES, temperature to $15°C$, salinity to 35, initial DIC to 5 $\mu mol\,kg^{-1}$ and k_{-a} was varied. Solid lines are the results for a seawater pH of 8.5, dashed lines for a pH of 8.0 and circles for a pH of 7.0. Illustrated in **A** are the results upon an addition of 500 $\mu mol\,kg^{-1}$ K_2CO_3 and in **B** the results upon an addition of 500 $\mu mol\,kg^{-1}$ CO_2.

Figure 5 Graphical illustration of the k_+ values determined with the fitting procedure shown in Fig.1 and described in section 2.3, measured by additions of ~ 15 $\mu mol\,kg^{-1}$ CO_2 at different temperatures and seawater pH (total scale). Squares denote seawater buffered with 50 mM HEPES and circles seawater with 50 mM BICINE. The lines depict calculated k_+ with $k_+ = k_{+1} + k_{+4}[OH^-]$ (see Tab. 1 for details regarding the rate constants) at temperatures of 11 (dotted), 17 (dashed) and $26°C$ (solid line).

Figure 6 Comparison of γk_+ (dots), with k_+ calculated as for Fig.5, and the eigenvalues λ of the carbonate system (solid line) described in section 3.4 at $25°C$ at a salinity of 35 between pH 7 and 9. **A** compares γk_+ with λ while **B** illustrates the inverse of these values, which are the relaxation times τ of the carbonate system upon disturbance.

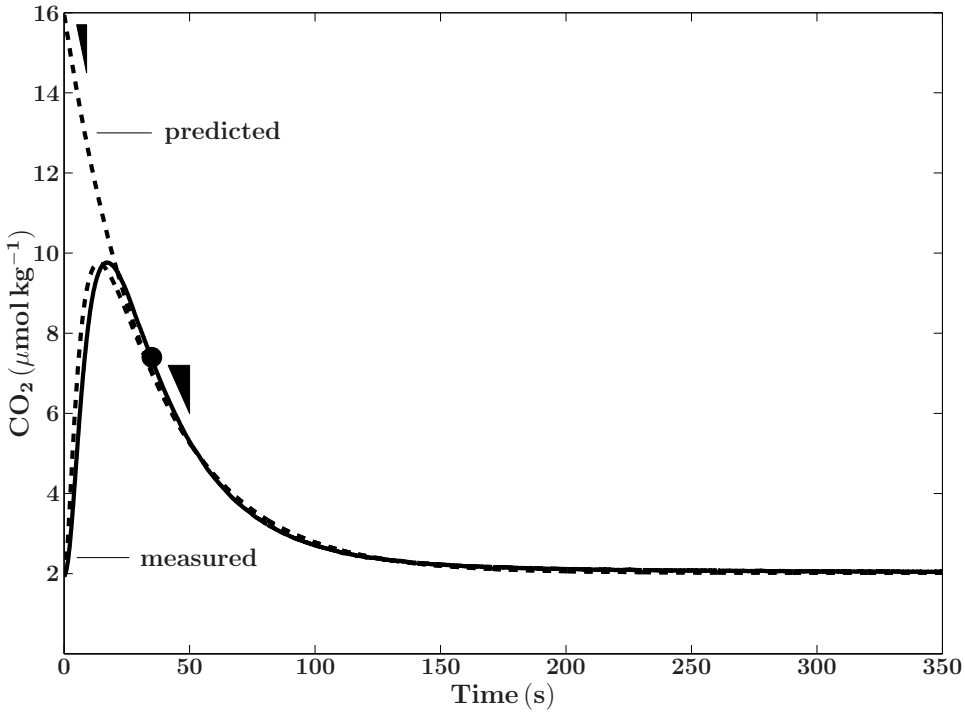
16
14
12
10
8
6
4
2
predicted
measured
CO_2 (μmol kg^{-1})
0
50
100
150
200
250
300
350
Time (s)

Figure 1

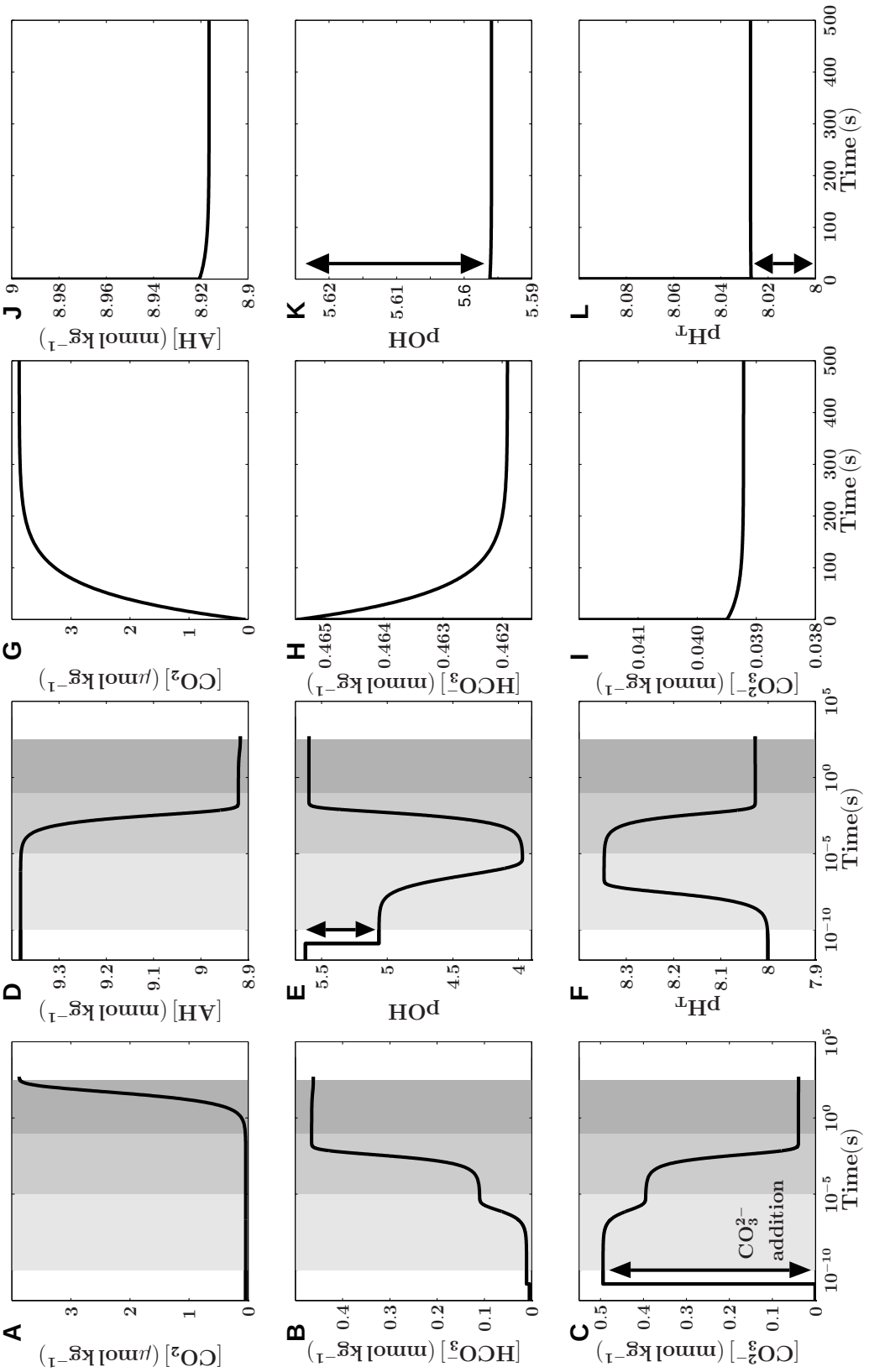
A
B
C
D
E
F
G
H
I
J
K
L
$[CO_2]$ (μmol kg^{-1})
$[HCO_3^-]$ (mmol kg^{-1})
$[CO_3^{2-}]$ (mmol kg^{-1})
[AH] (mmol kg^{-1})
pOH
pH_T
$[CO_2]$ (μmol kg^{-1})
$[HCO_3^-]$ (mmol kg^{-1})
$[CO_3^{2-}]$ (mmol kg^{-1})
[AH] (mmol kg^{-1})
pOH
pH_T
CO_3^{2-} addition
Time(s)
Time (s)

Figure 2

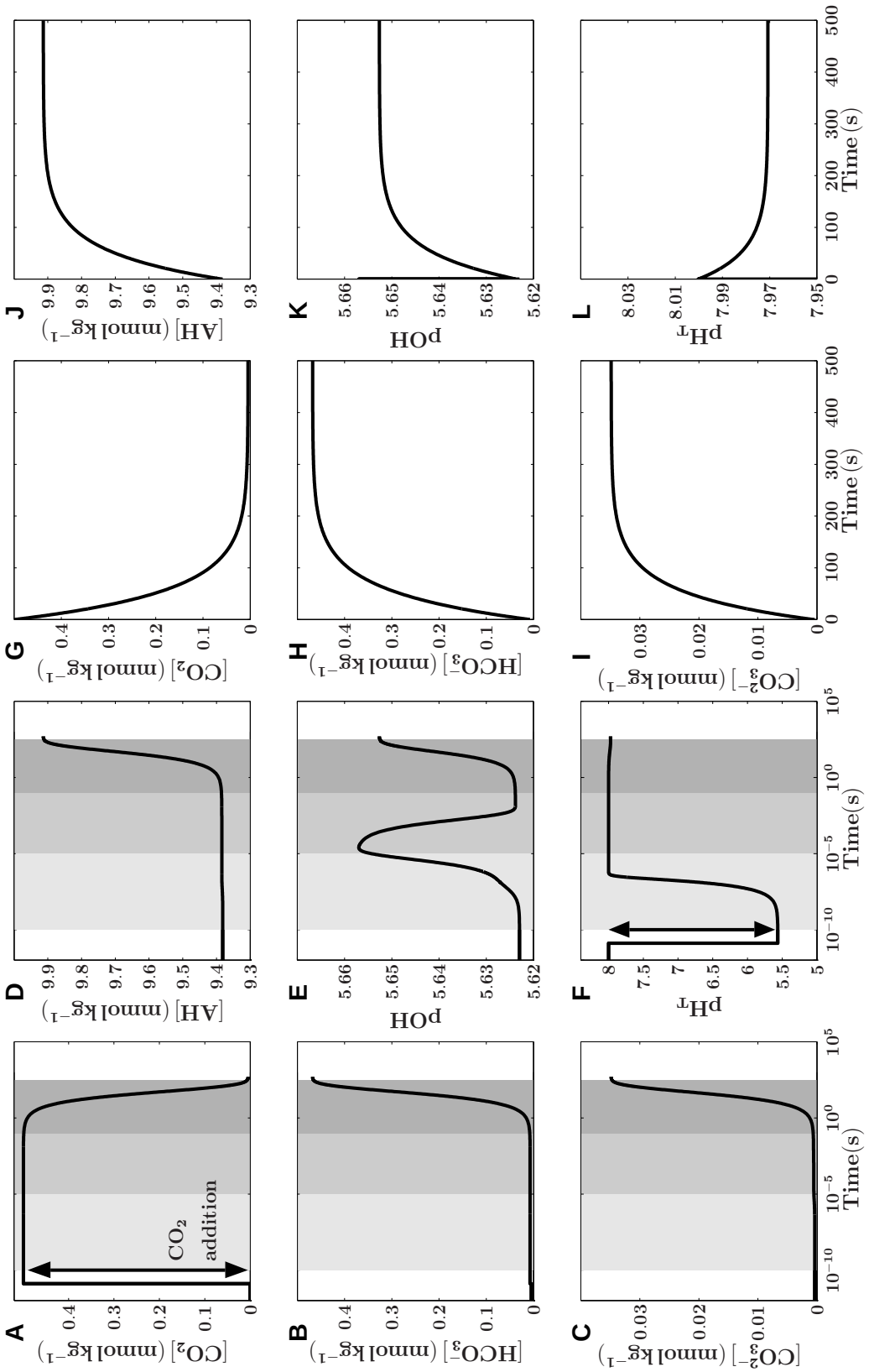
A
B
C
D
E
F
G
H
I
J
K
L
$[CO_2]$ (mmol kg^{-1})
$[HCO_3^-]$ (mmol kg^{-1})
$[CO_3^{2-}]$ (mmol kg^{-1})
[AH] (mmol kg^{-1})
pOH
pH_T
CO_2 addition
Time(s)
Time (s)

Figure 3

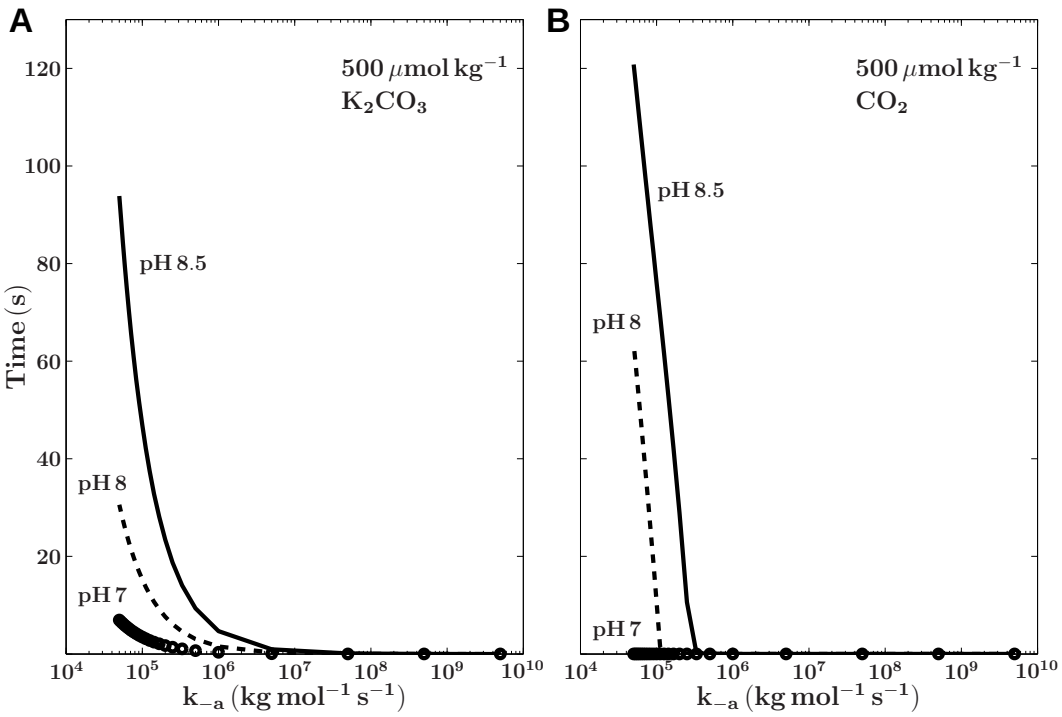
A
B
500 μmol kg−1
K2CO3
500 μmol kg−1
CO2
pH 8.5
pH 8
pH 7
Time (s)
120
100
80
60
40
20
10^4
10^5
10^6
10^7
10^8
10^9
10^10
k−a (kg mol−1 s−1)

Figure 4

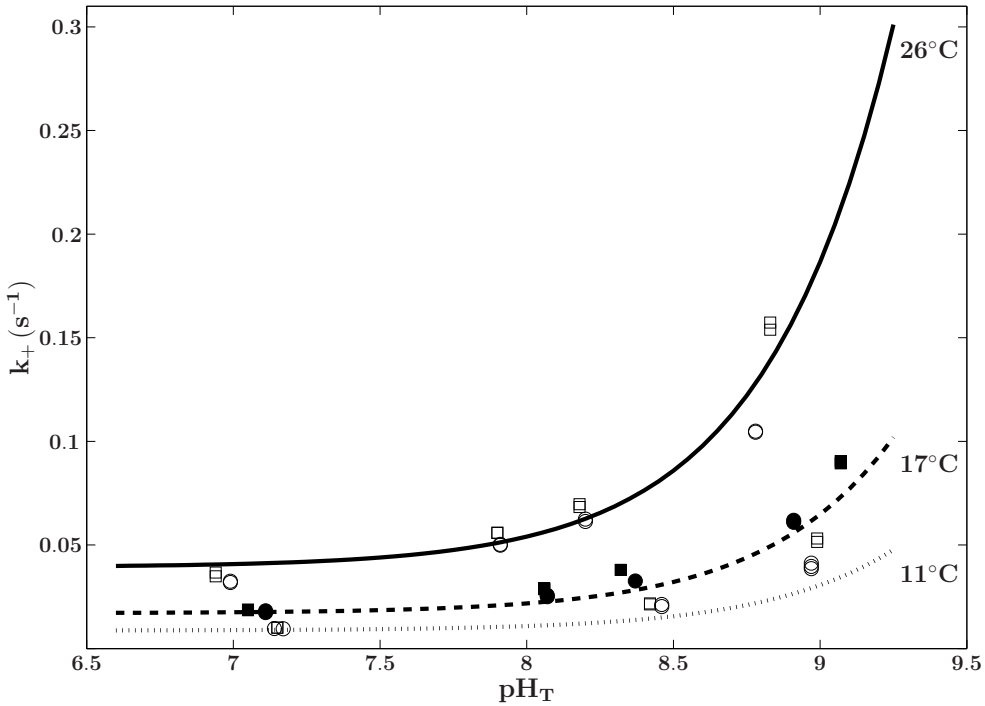

Figure 5

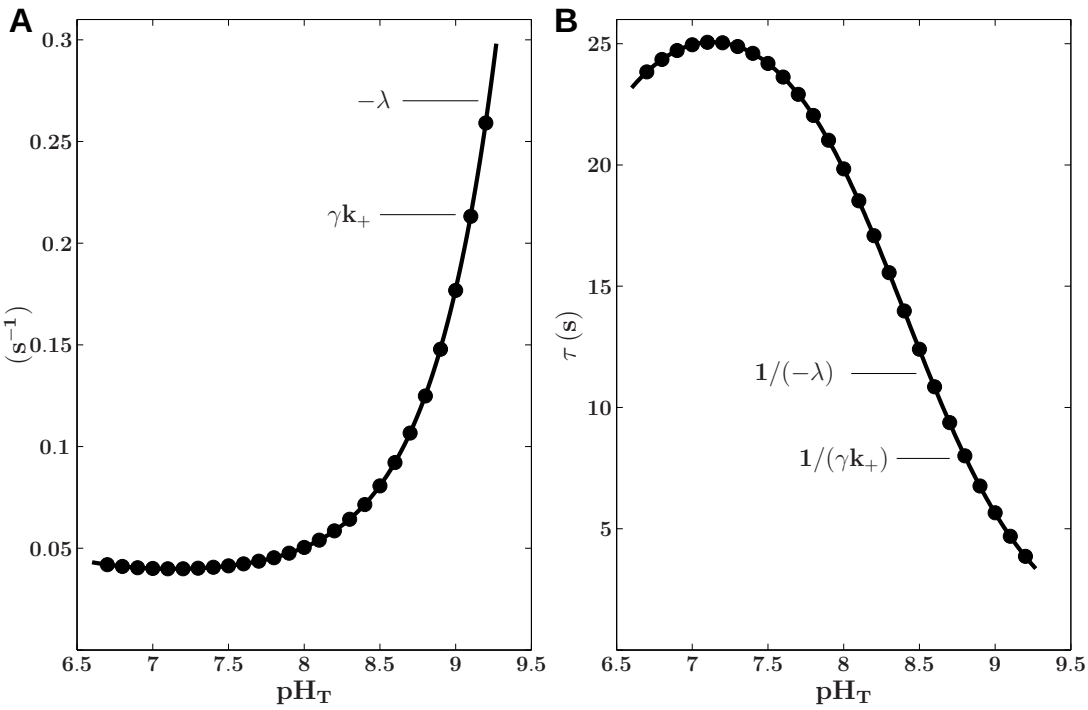

Figure 6

3 SYNTHESIS

The publications presented in this thesis all describe aspects relevant for marine carbon cycling. As the processes investigated cover a wide range of time scales the publications shall be discussed individually.

3.1 The marine carbon cycle and orbitally forced climate change

It is widely accepted that the quasi-periodic oscillation in the seasonal distribution of solar energy, arising from changes in Earth's orbital parameters of precession, obliquity and eccentricity, are closely connected to climate variability of the last couple of million years. The quasi-periodic variations of precession, obliquity and eccentricity have dominant frequencies centred around 19/23, 41, and 100 kyr, respectively. Numerous studies have shown that paleoproxy records have cyclicities close to that of these parameters (Imbrie et al., 1993a). However, the nature of this connection is not clear as several paradoxes emerge, known as the 'three classical problems of Pleistocene research' (Paillard, 2001).

The 100 kyr problem: Paleoproxy records of the last million of years are dominated by a quasi-100 kyr cyclicity, the glacial/interglacial cycles (Imbrie et al., 1984). However, variations in eccentricity are partly out of phase with these cycles. Furthermore, the contribution of eccentricity to changes in insolation is small compared to those of precession and obliquity.

The Late Pleistocene transition problem: The 100 kyr glacial/interglacial cycles are absent from climate records between 1 and 2 million years BP, which in turn exhibit a 41 kyr cyclicity (Imbrie et al., 1993b). This switch, known as the Mid-Pleistocene-Revolution (MPR) miraculously occurred between 800,000 and 1 million years BP.

The stage 11 problem: the most prominent termination (i.e. termination V at $\sim$420,000 years BP.) occurs at times of relatively low variation in insolation.

Furthermore, recent findings challenge the dogma of a sole Northern Hemisphere (NH)

insolation forcing leading to terminations, first proposed by Milutin Milankovitch (1941). They suggest a pivotal role of the Southern Hemisphere (SH) in glacial terminations (Knorr and Lohmann, 2003; Peeters et al., 2004). But so far, no single trigger could be identified, accounting for all the paradoxes, and setting the proposed mechanisms in motion. In publication I a mathematical analysis of changes in midsummer insolation in both hemispheres is presented. It is shown that prior to each termination insolation increases simultaneously in both hemispheres with a temporal SH lead. Introduction of a time and an energy threshold to these overlaps yield the so-called 'insolation canon' which predicts glacial terminations in perfect agreement with the geologic record. Moreover, this trigger is absent during the Early Pleistocene, lacking the prominent glacial terminations. It is demonstrated that the concept of the 'insolation canon' can resolve the 100 kyr mystery, and implications for the 'Late Pleistocene transition' and the 'stage 11' problems are discussed.

There are many theories regarding the mechanisms operating during abrupt climate changes, with glacial/interglacial being the most prominent ones. This includes variations in deep water formation in the Arctic or Antarctic Ocean, in freshwater discharge to these key regions, in the extension of sea-ice cover around the Arctic or Antarctic (for examples see Stephens and Keeling (2000); Morales Maqueda and Rahmstorf (2002); Knutti et al. (2004); Peeters et al. (2004)), in the stability and dynamics of ice masses on land (Imbrie and Imbrie, 1980; Paillard, 1998), or in nutrient utilisation of phytoplankton, for example the iron-hypothesis (Martin, 1990). The two constraints, fundamental to the trigger proposed in publication I, are energy and time. First, the need for a certain amount of energy supplied to the Antarctic and Arctic in the summer season to start a deglaciation indicates that sea/land-ice melting are pivotal in the subsequent feedback mechanisms. And second, the necessity for at least 1000 years (the typical time scale for ocean overturning) of synchronous midsummer insolation increase points to the involvement of global thermohaline circulation, thereby connecting both hemispheres. Several studies have demonstrated the strong influence of freshwater pulses (from melting ice) on the climate system, changing thermohaline circulation via impacts on deep water formation (for examples see Rahmstorf

(2002); Knutti et al. (2004); Pahnke and Zahn (2005)). This ocean wide overturning itself is capable to strongly influence climate on a global scale. Although the relative contribution of melting Antarctic and NH ice sheets to sea level rises following deglaciations have yet to be established, glacial terminations are a global phenomenon (Clark et al., 2002; Waver et al., 2003; Rohling et al., 2004). In this respect, it makes sense that also the trigger, proposed in publication I, encompasses and connects both hemispheres.

In summary, the 'insolation canon' can resolve the paradoxes normally associated with orbitally forced climate change. Via its constraints this trigger suggests feedback mechanisms involved which have been shown to operate during abrupt climate change, capable to redistribute carbon between the ocean/atmosphere system. Furthermore, its origin is in the Southern Hemisphere, corroborated by studies which highlight the pivotal role of the Southern Hemisphere for glacial terminations.

3.2 The marine carbon cycle, trace metals and the biological carbon pump

Variations in atmospheric dust deposition to certain oceanic regions are closely correlated with glacial/interglacial cycles (Petit et al., 1999). At the last glacial maximum (LGM) dust input to the Southern Ocean was probably about 20 times higher than today (Mahowald et al., 1999). Trace metals contained in dust, such as iron and zink, are essential plant nutrients which can limit phytoplankton growth in parts of todays ocean (see section 1.4 in the General Introduction for details).

It has been hypothesised that variations in the supply of dust, and hence iron and zinc, to the surface ocean may influence primary production and that enhanced dust input in glacial times could have strengthened phytoplankton production during these periods. A concomitant increase in the intensity of the organic carbon pump could have contributed to lower atmospheric CO_2 in glacial times (Martin, 1990; Morel et al., 1994). On the other hand, possible effects of enhanced trace metal input on the strength of the inorganic carbon

($CaCO_3$) pump have so far been neglected. In publication II and III the effect of iron and zinc availability on $CaCO_3$ production in the coccolithophore *Emiliania huxleyi* is described. It is shown that at low iron concentrations calcification and growth are equally reduced. At low zinc concentrations, however, these two processes are de-coupled leading to highly calcified cells. The observed differences in calcification between iron and zinc limited cells could be related to the specific role of the two micronutrients in cellular processes. While zinc is an essential co-factor in many enzymes and probably directly involved in growth via carbonic anhydrase and the zinc-finger motive of various transcription factors, iron is a key element in photosynthetic electron transport (for a review see Falkowski and Raven (1997)) and hence closely linked to the cell's energy budget.

For instance, it is shown in publication IV that uptake of inorganic carbon for photosynthesis and probably calcification is significantly reduced under iron limitation. Moreover, the internal cycling of inorganic carbon within the cell is most likely even more affected, indicating a severe energy limitation. Hence, since biogenic calcification is a light (energy) dependent process (for examples see Paasche (1964); Linschooten et al. (1991)), iron limitation not only reduces growth rates in *Emiliania huxleyi* but also the rate of $CaCO_3$ production. In contrast, zinc deficiency does not significantly affect the rate of calcification, although slowing down cellular growth. This indicates that the energy allocated for $CaCO_3$ precipitation remains unaffected under zinc limitation. Furthermore, reduced growth rates but unaltered rates of calcification lead to an increase in the $CaCO_3$ to PON (particulate organic nitrogen) ratio at low zinc concentrations.

The observed responses of $CaCO_3$ production in *Emiliania huxleyi* to changes in iron and zinc availability are probably of different biogeochemical relevance. Alleviation of iron limitation in glacial times due to enhanced dust input is not likely to have altered coccolithophorid $CaCO_3$ production on the global scale, because biogenic calcification in today's HNLC areas is negligible. However, alleviation of zinc limitation in glacial times could have altered global $CaCO_3$ production by two mechanisms. The first evidence comes from a study by Crawford et al. (2003) who showed that stimulation of primary production by

additions of zinc to the surface ocean in the North Pacific lead to changes in phytoplankton community structure in favour of coccolithophores. The second evidence comes from the results shown in publication II which indicate that the amount of $\mathrm{CaCO_3}$ precipitated in conjunction with a given amount of coccolithophorid biomass (the $\mathrm{CaCO_3}$ to PON ratio) is expected to decrease with increasing zinc concentrations. Although it is impossible to quantify the contribution of these two counteracting processes (i.e. more coccolithophores but with less $\mathrm{CaCO_3}$ per cell), it becomes evident that the availability of the trace metal zinc has the potential to impact $\mathrm{CaCO_3}$ production in the ocean. Any changes in the intensity of the $\mathrm{CaCO_3}$ pump will alter the partitioning of carbon within the ocean/atmosphere system which may need to be considered in the context of glacial/interglacial climate change.

3.3 Inorganic carbon acquisition and carbon isotope fractionation in marine phytoplankton

In seawater dissolved inorganic carbon (DIC) is present in three forms ($\mathrm{CO_2}$, $\mathrm{HCO_3^-}$ and $\mathrm{CO_3^{2-}}$), summing up to concentrations of about 2200 $\mu\mathrm{mol\,kg^{-1}}$. At typical seawater pH around 8, most DIC is present as $\mathrm{HCO_3^-}$ and $\mathrm{CO_3^{2-}}$, whereas $\mathrm{CO_2}$ contributes less than 1%. $\mathrm{CO_2}$ concentrations range therefore generally between 8 and 20 $\mu\mathrm{mol\,kg^{-1}}$. Moreover, $[\mathrm{CO_2}]$ are further depleted in the close vicinity of phytoplankton cells, the diffusive boundary layer (Wolf-Gladrow and Riebesell, 1997). The main carboxylating enzyme in marine phytoplankton, however, (RubisCO) uses $\mathrm{CO_2}$ as sole substrate (Cooper et al., 1969). Depending on the type of RubisCO, carbon fixation rates are half-saturated at $[\mathrm{CO_2}]$ between 20 to 70 $\mu\mathrm{mol\,kg^{-1}}$ (Badger et al., 1998). Hence, to overcome potential rate limitations for inorganic carbon uptake most phytoplankton species operate so-called carbon concentrating mechanisms (CCMs), investing relatively large amounts of energy (Raven and Lucas, 1985; Badger et al., 1998). CCMs transport considerable amounts of inorganic carbon over the plasmalemma and the chloroplast membrane, counteracting the diffusive loss of $\mathrm{CO_2}$ into the external medium.

As RubisCO fractionates against $^{13}CO_2$ with about $29‰$ (Roeske and O'Leary, 1984), the internal DIC pool becomes enriched in ^{13}C in comparison to the external medium. High DIC uptake and CO_2 efflux in comparison to the fixation flux diminishes this internal ^{13}C enrichment. Hence, the ratio of the diffusive CO_2 efflux to the DIC uptake rate into the cell was proposed to determine carbon isotope fractionation (Farquhar et al., 1982; Sharkey and Berry, 1985; Burkhardt et al., 1999).

In publication IV these fluxes are investigated in the coccolithophore *Emiliania huxleyi* under varying degrees of iron limitation with respect to carbon isotope fractionation (ϵ_p). It is shown that uptake rates of inorganic carbon decrease with increasing iron limitation and concomitant leakage (the ratio of CO_2 efflux out of the cell to DIC uptake) rises, indicating reduced CCM efficiency. Based on these results, the one compartment cell model by Burkhardt et al. (1999), in which fractionation is positive linearly correlated with the leakage, predicts an increase of ϵ_p by more than $10‰$. Direct measurements of ϵ_p in *Emiliania huxleyi*, however, revealed that carbon isotope fractionation is independent from the degree of iron limitation and remains rather constant. This puzzling contradiction can be explained with a two compartment cell model (Wolf-Gladrow et al., 1999) comprising the cytosol and a chloroplast, presented in publication IV. This model considers not only the fluxes from the external medium into the cytosol and those out of the cell but also those into and out of the chloroplast. It shows that ϵ_p is extremely sensitive to the fluxes in and out the chloroplast and can be constant although leakage is changing. This is easily understood by considering the following example in which DIC is taken up into the cytosol and chloroplast only as CO_2. In the one compartment model a leakage of 0.5 leads to half the maximum fractionation of RubisCO giving an apparent fractionation of about 14.5‰ (see section 1.6 in the General Introduction for details). In the two compartment model fractionation reaches that value only if the DIC flux into and out of the chloroplast is about an order of magnitude higher than the DIC uptake from the external medium and necessarily approaches zero when all the CO_2 taken up into the chloroplast is being fixed (no 'leakage' from the chloroplast!). Constant fractionation with increasing leakage under varying degrees of iron limitation can

therefore be explained by reduced cycling of DIC in and out the chloroplast.

In that respect, changes in the internal fluxes could explain why ϵ_{p} depends on the growth limiting resource as proposed by Riebesell et al. (2000). For instance, varying degrees of light limitation appear to have only a minor effect on ϵ_{p} (Johnston, 1996; Riebesell et al., 2000; Rost et al., 2002), while nitrogen limitation causes a significant increase in the carbon isotope fractionation pattern (Laws et al., 1995, 1997). In this sense, iron and light seem to have similar effects on inorganic carbon acquisition, probably by determining the cell's energy budget, contrasting the effects of nitrogen limitation.

3.4 Kinetics in the carbonate system

Regarding the three dissolved carbon species in seawater, the carbonate system in equilibrium is described by two equilibria, between $\mathrm{CO_2}$ (the sum $\mathrm{CO_2}$(aq) and $\mathrm{H_2CO_3}$) and $\mathrm{HCO_3^-}$, and between $\mathrm{HCO_3^-}$ and $\mathrm{CO_3^{2-}}$ (see section 1.5 in the General Discussion for details). Considering the reactions between these pools, however, involve multiple elementary reaction pathways. For simplicity, in the following considerations the reactions involving boric acid are excluded (for details see Zeebe et al. (1999), pp.106-108). Then, there are two elementary reactions between $\mathrm{HCO_3^-}$ and $\mathrm{CO_3^{2-}}$, and two between $\mathrm{CO_2}$(aq) and $\mathrm{HCO_3^-}$ (see the Appendix of publication V for details). Chemical equilibrium between $\mathrm{HCO_3^-}$ and $\mathrm{CO_3^{2-}}$ is established by protolysis ($\mathrm{CO_3^{2-} + H^+ \rightleftharpoons HCO_3^-}$) and by hydrolysis ($\mathrm{HCO_3^- + OH^- \rightleftharpoons CO_3^{2-} + H_2O}$). Between $\mathrm{CO_2}$(aq) and $\mathrm{HCO_3^-}$ chemical equilibrium is established by two hydration reactions ($\mathrm{CO_2(aq) + H_2O \rightleftharpoons HCO_3^- + H^+}$ and via true carbonic acid as $\mathrm{CO_2(aq) + H_2O \rightleftharpoons H_2CO_3 \rightleftharpoons HCO_3^- + H^+}$). Until recently, it was impossible to quantify the contribution of these two latter pathways to the overall hydration reaction (Soli and Byrne, 2002). Hence, an overall hydration, including both hydration pathways, is generally used (Johnson, 1982). It is defined as $\mathrm{CO_2 + H_2O \rightleftharpoons HCO_3^- + H^+}$. Note again that $\mathrm{CO_2}$ denotes the sum of $\mathrm{CO_2}$ and $\mathrm{H_2CO_3}$. Finally, $\mathrm{CO_2}$ can also combine with $\mathrm{OH^-}$ in a hydroxylation reaction ($\mathrm{CO_2 + OH^- \rightleftharpoons HCO_3^-}$). Rate constants for the forward

and backward reaction characterise each reaction mentioned above. The time required to establish chemical equilibrium after a disturbance in the carbonate system depends on the rate constants and on the concentrations of the reactants. Calculation of such relaxation times upon disturbance requires to solve each of the equation mentioned above in a coupled system (including the water reaction, $H_2O \rightleftharpoons H^+ + OH^-$). For many purposes, however, this is a cumbersome task. For example, so-called disequilibrium methods (i.e. the mass spectrometric approach (Badger et al., 1994) and the ^{14}C disequilibrium method (Cooper et al., 1969; Espie and Colman, 1986)) rely on the exact knowledge of the kinetic rate constants for the overall CO_2 to HCO_3^- interconversion which are given by the rate constants of the hydration and hydroxylation reactions.

In publication V a new method is described to accurately measure these rate constants, termed k_+ and k_-, in pH-buffered seawater systems by means of membrane inlet mass spectrometry (MIMS). k_+ and k_- are determined by monitoring the CO_2 evolution curve with the MIMS upon additions of known amounts of CO_2 into a reaction chamber. This curve is recording a subsequent decrease in $[CO_2]$ as CO_2 is converted to HCO_3^- and is fitted to a suitable equation, derived in publication V, yielding k_+ and k_-. Utilisation of k_+ and k_- in both disequilibrium methods and the fitting procedure require the pH to be constant on time scales of seconds. However, a possible influence of the pH buffers, generally utilised, on the kinetics in the carbonate system has hitherto not been investigated. A full fledged numerical model of the carbonate system in seawater is therefore employed to demonstrate how pH buffers are operating. It is shown that measured rate constants are in reasonable agreement with calculated values in a pH range of 7 to 8.5 and at temperatures from 10 to 25°C. This indicates that the two buffers tested (HEPES and BICINE) are able to keep the pH constant on time scales of seconds, as required by the fitting procedure. Hence, a way is presented to directly calculate k_+ and k_- for further applications. Moreover, it is noted that the method previously proposed to determine the rate constants for the CO_2 to HCO_3^- interconversion (Badger et al., 1994) tends to significantly underestimate these constants.

In summary, publication V places the determination of k_+ and k_-, needed when experimentally assessing inorganic carbon fluxes in marine phytoplankton, within a theoretical framework and extends and improves a method proposed previously.

3.5 Perspectives for future research

Several directions for future research emerge from this doctoral thesis. In publication I a mathematical analysis of midsummer insolation changes in both hemispheres reveals a possible trigger for glacial terminations, the 'insolation canon'. Still, the question remains how warm interglacial turns into cold glacial climate, in other words what causes glacial inceptions. It is shown in publication I that the simultaneous insolation changes in both hemispheres also produce a 'negative insolation canon' which is the synchronous insolation decrease in both hemispheres with a temporal Southern Hemisphere lead. This 'negative' forcing exhibits a similar energy and distribution pattern as the 'positive' one. The interplay between these two opposing insolation forcings could be responsible for the prominent 100 kyr saw tooth shaped climate history in the Late Pleistocene. To test this hypothesis, a first step would be the development of simple conceptual models to understand the interactions of the insolation forcings with possible feedback mechanisms within the ocean/atmosphere system. Furthermore, the ultimate goal would be the incorporation of the 'insolation canon' into general circulation models (GCMs) to test if climate is sensitive to the triggers proposed.

Publication II and III report laboratory experiments in which calcification of *Emiliania huxleyi* is sensitive to the availability of zinc. Following up on this finding would be to test if this is a general phenomenon in coccolithophores, especially in those which do not form blooms, as these probably contribute significantly to the overall amount of $\mathrm{CaCO_3}$ produced by this group of organisms. Additionally, on-deck ship incubations with natural phytoplankton assemblages could be employed to investigate the findings, shown in publication II and III, in the field. Based on the presented results, enhanced zinc availability

would correspond with lower $CaCO_3$ production, opposing the observation that coccolithophorid biomass increased upon additions of zinc (Crawford et al., 2003). Hence, on-deck incubations may help to resolve the question whether enhanced zinc input in glacial times could have decreased the ocean's carbonate pump which would have contributed to lower atmospheric CO_2 during these times.

In publication IV inorganic carbon flux measurements in *Emiliania huxleyi* under varying degrees of iron limitation are presented, together with measurements of stable carbon isotope fractionation. It is shown that measured fractionation patterns are contradicting those calculated from measured fluxes when considering the cell as one compartment. However, it is demonstrated that a two compartment cell model with an additional chloroplast is able to resolve this seeming contradiction. Hence, application of flux measurements in combination with carbon isotope fractionation data under different growth limiting conditions (such as light, nitrogen or phosphorus limitation) could enhance our understanding of inorganic carbon acquisition and concomitant apparent fractionation. Moreover, these investigations under zinc limitation could provide information on the importance of internal carbonic anhydrase for the functioning of a CCM. This mechanistic understanding of carbon isotope fractionation is required for the interpretation of isotopic data from the sedimentary record. Furthermore, the two compartment cell model, presented in publication IV, could be extend by an additional compartment for calcification, representative for coccolithophores. Then, determinations of the inorganic carbon fluxes and measurements of stable carbon isotope fractionation in both, the organic matter produced and the $CaCO_3$ precipitated, may give clues about how the process of calcification is realized within this group of phytoplankton. Despite decades of intensive research, the question how and why coccolithophores calcify is still controversially discussed.

3.6 References

Badger, M. R., Andrews, T., Whitney, S. M., Ludgwig, M., Yellowlees, D. C., Leggat, W., Price, G. D., 1998. The diversity and coevolution of Rubisco, plastids, pyrenoids, and chloroplast-based CO_2-concentrating mechanisms in algae. Can. J. Bot. 76, 1052–1071.

Badger, M. R., Palmqvist, K., Yu, J.-W., 1994. Measurement of CO_2 and HCO_3^- fluxes in cyanobacteria and microalgae during steady-state photosynthesis. Physiol. Plantarum 90, 529–536.

Burkhardt, S., Riebesell, U., Zondervan, I., 1999. Effects of growth rate, CO_2 concentration, and cell size on the stable carbon isotope fractionation in marine phytoplankton. Geochim. Cosmocim. Acta 63, 3729–3741.

Clark, P. U., Mitrovica, J. X., Milne, G. A., Tamisiea, M. E., 2002. Sea-Level Fingerprinting as a Direct Test for the Source of Global Meltwater Pulse IA. Science 295, 2438–2441.

Cooper, T. G., Filmer, D., Wishnick, M., Lane, M. D., 1969. The Active Species of "CO_2"Utilized by Riboluse Diphosphate Carboxylase. J. Biol. Chem. 244, 1081–1083.

Crawford, D. W., Lipsen, M. S., Purdie, D. A., Lohan, M. C., Statham, P. J., Whitney, F. A., Putland, J. N., Johnson, W. K., Sutherland, N., Peterson, T. D., Harrison, P. J., Wong, C. S., 2003. Influence of zinc and iron enrichments on phytoplankton growth in the northeastern subarctic Pacific. Limnol. Oceanogr. 48, 1583–1600.

Espie, G. S., Colman, B., 1986. Inorganic carbon uptake during photosynthesis. I. A theoretical analysis using the isotope disequilibrium technique. Plant. Physiol. 80, 863–869.

Falkowski, P. G., Raven, J., 1997. Aquatic photosynthesis. Blackwell Science.

Farquhar, G. D., O'Leary, M. H., Berry, J. A., 1982. On the relationship between carbon isotope discrimination and the intercellular carbon dioxide concentration in leaves. Aust. J. Plant Physiol. 9, 121–137.

Imbrie, J., Berger, A., Boyle, E. A., Clemens, S. C., Duffy, A., Howard, W., Kukla, G., Kutzbach, J., Martinson, D. G., McIntyre, A., Mix, A. C., Molfino, B., Morley, J. J., Peterson, L. C., Pisias, N. G., Prell, W. L., Raymo, M. E., Shackelton, N. J., Toggweiler, J. R., 1993a. On the structure and origin of major glaciation cycles 2. The 100.000-year cycle. Paleoceanogr. 8, 699–735.

Imbrie, J., Berger, A., Shackelton, N. J., 1993b. Role of orbital forcing: A two-million-year perspective. *In*: Global Changes in the Perspective of the Past. Eddy, J. A. and Oeschger, H. (eds.). John Wiley, New York.

Imbrie, J., Hays, J. D., Martinson, D., McIntyre, A., Mix, A. C., Morley, J. J., Pisias, N. G., Prell, W. L., Shackleton, N. J., 1984. The orbital theory of Pleistocence climate: Support from a revised chronology of the marine $\delta^{18}\mathrm{O}$ record. In: Berger, A. L., Imbrie, J., Hays, J., Kukla, G., Salzman, B. (Eds.), Milankovitch and Climate, Part 1. D. Reidel Publishing Group, pp. 269–305.

Imbrie, J., Imbrie, J. Z., 1980. Modelling the climatic response to orbital variations. Science 207, 943–953.

Johnson, K. S., 1982. Carbon dioxide hydration and dehydration kinetics in seawater. Limnol. Oceanogr. 27, 849–855.

Johnston, A. M., 1996. The effect of environmental variables on $^{13}\mathrm{C}$ discrimination by two marine phytoplankton. Mar. Ecol. Prog. Ser. 132, 257–263.

Knorr, G., Lohmann, G., 2003. Southern Ocean origin for the resumption of Atlantic thermohaline circulation during deglaciation. Nature 424, 532–536.

Knutti, R., Flückiger, J., Timmermann, A., 2004. Strong hemispheric coupling of glacial climate through freshwater discharge and ocean circulation. Nature 430, 851–856.

Laws, E. A., Bidigare, R. R., Popp, B. N., 1997. Effect of growth rate and CO_2 concentration on carbon isotopic fractionation by the marine diatom *Phaeodactylum tricornutum*. Limnol. Oceanogr. 42, 1552–1560.

Laws, E. A., Popp, B. N., Bidigare, R. R., Kennicutt, M. C., Macko, S. A., 1995. Dependence of phytoplankton carbon isotopic composition on growth rate and $[co_2]_{aq}$: Theoretical considerations and experimental results. Geochim. Cosmochim. Acta 59, 1131–1138.

Linschooten, C., van Bleijswijk, J., van Emburg, P., de Vrind, J., Kempers, E., Westbroek, P., de Vrind-de Jong, E., 1991. Role of light-dark cycle and medium composition on the production of coccoliths by *Emiliania huxleyi* (Hyptophyceae). Journal of Phycology 27, 82–86.

Mahowald, N., Kohfeld, K., Hansson, M., Balkanski, Y., Harrison, S. P., Prentice, I. C., Schulz, M., Rodhe, H., 1999. Dust sources and deposition during the last glacial maximum and current climate: A comparision of model results with paleodata from ice cores and marine sediments. J. Geophys. Res. 104, 15895–15916.

Martin, J. H., 1990. Glacial-interglacial CO_2 change: the iron hypothesis. Paleocenogr. 5, 1–13.

Milankovitch, M., 1941. Kanon der Erdbestrahlung und seine Anwendung auf das Eiszeitproblem. Vol. **Spec. Publ. 132** .

Morales Maqueda, M. A., Rahmstorf, S., 2002. Did Antarctic sea-ice expansion cause glacial CO_2 decline? Geophys, Res. Lett. 29, 1011, doi:10.1029/2001GL013240.

Morel, F. M. M., Reinfelder, J. R., Roberts, S. B., Chamberlain, C. P., Lee, J. G., Yee, D., 1994. Zinc and carbon co-limitation of marine phytoplankton. Nature 369, 740–742.

Paasche, E., 1964. A tracer study of the inorganic carbon uptake during coccolithformation and photosynthesis in the coccolithophorid *Coccolithus huxleyi*. Physiologia Plantarum Supplementum III, 1–82.

Pahnke, K., Zahn, R., 2005. Southern Hemisphere Water Mass Conversion Linked with North Atlantic Climate Variability. Science 307, 1741–1746.

Paillard, D., 1998. The timing of Pleistocene glaciations from a simple multiple-state model. Nature 391, 378–381.

Paillard, D., 2001. Glacial cylces: towards a new paradigm. Rev. Geophys. 39, 325–346.

Peeters, F. J. C., Acheson, R., Bummer, G. J. A., de Ruijter, W. P. M., Schneider, R. R., Ganssen, G. M. Ufkes, E., Kroon, D., 2004. Vigorous exchange between the Indian and Atlantic oceans at the end of the past five glacial periods. Nature 430, 661–665.

Petit, J. R., Jouzel, J., Raynaud, D., Barkov, N. I., Barnola, J. M., Basile, I., Benders, M., Chappellaz, J., Davis, M., Delaygue, G., Delmotte, M., Kotlyakov, V. M., Legrand, M., Lipenkov, V. Y., Lorius, C., Pépin, L., Ritz, C., Saltzman, E., Stievenard, M., 1999. Climate and atmospheric history of the past 420, 000 years from the Vostok ice core, Antarctica. Nature 399, 429–236.

Rahmstorf, S., 2002. Ocean circulation and climate during the past 120,000 years. Nature 419 (207-214).

Raven, J. A., Lucas, W. J., 1985. Energy costs of carbon acquisition, p. 305-324 *In* Lucas, W. J. and Berry, J. A. [eds.], Inorganic carbon Uptake by Aquatic Photosynthetic Organisms. American Society of Plant Physiologists.

Riebesell, U., Burkhardt, S., Dauelsberg, A., Kroon, B., 2000. Carbon isotope fractionation by a marine diatom: dependence on the growth-rate-limiting resource. Mar. Ecol. Progr. Ser. 193, 295–303.

Roeske, C., O'Leary, M., 1984. Carbon isotope effects on the enzyme-catalyzed carboxilation of ribulose bisphosphate. Biochem. 23, 6275–6285.

Rohling, E. J., Marsh, R., Erlls, N. C., Sidall, M., Edwards, N. R., 2004. Similar meltwater contributions to glacial sea level changes from Antarctic and northern ice sheets. Nature 430, 1016–1021.

Rost, B., Zondervan, I., Riebesell, U., 2002. Light-dependent carbon isotope fractionation in the coccolithophore *Emiliania huxleyi*. Limnol. Oceanogr. 47, 120–128.

Sharkey, T. D., Berry, J. A., 1985. Carbon isotope fractionation of algae as influenced by an inducible CO_2 concentrating mechanism *In* Lucas, W. J. and Berry, J. A. [eds.], Inorganic carbon Uptake by Aquatic Photosynthetic Organisms. American Society of Plant Physiologists.

Soli, A. L., Byrne, R. H., 2002. CO_2 system hydration and dehydration kinetics and the equilibrium CO_2/H_2CO_3 ratio in aqueous NaCL solution. Mar. Chem. 78, 65–73.

Stephens, B. B., Keeling, R. F., 2000. The influence of Antarctic sea ice on glacial-interglacial CO_2 vatiations. Nature 404, 171–174.

Waver, A. J., Saenko, O. A., Clark, P. U., Mitrovica, J. X., 2003. Meltwater Pulse 1A from Antarctica as a Trigger of the Bølling-Allerød Warm Interval. Science 299, 1709–1713.

Wolf-Gladrow, D., Burkhardt, S. A., Riebesell, U., 1999. Carbon isotopic fractionation in microalgae: the effect of intracellular compartments. ASLO, Santa Fé, http://aslo.org/meetings/santafe99/abstracts/SS32MO0245E.html.

Wolf-Gladrow, D., Riebesell, U., 1997. Diffusion and reactions in the vicinity of plankton: A refined model for inorganic carbon transport. Mar. Chem. 59, 17–34.

Zeebe, R. E., Wolf-Gladrow, D. A., Jansen, H., 1999. On the time required to establish chemical and isotopic equilibrium in the carbon dioxide system in seawater. Mar. Chem. 65, 135–153.

4 Summary

This doctoral thesis investigates processes relevant for marine carbon cycling. Among those, emphasis is put on inorganic carbon acquisition for both photosynthetic carbon fixation and calcification in the coccolithophore *Emiliania huxleyi*. To improve measurements of inorganic carbon fluxes on the cellular level, the kinetics in the seawater carbonate system are investigated. Experiments assessing the effect of trace metal availability on calcification in the coccolithophore *Emiliania huxleyi* indicate that $\mathrm{CaCO_3}$ production by this group of organisms may have contributed to changes in $\mathrm{CO_2}$ partitioning between atmosphere and ocean on glacial/intergalcial time scales. Furthermore, a potential trigger for the end of glacial periods, the glacial terminations, is proposed.

Earth's climate history of the last million of years is known to have oscillated between warm interglacial and cold glacial conditions. These shifts are associated with changes in the partitioning of carbon between the ocean/atmosphere system. They are believed to be somehow linked to variations in solar insolation received in high latitudes, resulting from variations in Earth's orbital parameters. In publication I, a possible trigger for the prominent terminations of glacial climate is proposed, termed the 'insolation canon', which is the synchronous increase in midsummer insolation at 65° latitude in both hemispheres, with a temporal Southern Hemisphere lead. This trigger explains the paradoxes normally associated with the theory of orbitally forced climate change, and is in full agreement with various modelling and observational data regarding the timing and origin of terminations. Moreover, via its energy and time constraints, the 'insolation canon' suggests the involvement of feedback mechanisms which have been demonstrated to operate during abrupt climate change such as sea/land ice melting and their impact on global thermohaline circulation.

Also the marine biosphere was suggested to constitute a feedback mechanisms for the re-partitioning of carbon between ocean and atmosphere on glacial/interglacial time scales. For instance, it was proposed that in glacial times enhanced dust and hence trace metal input into parts of the ocean, in which phytoplankton growth is presently limited by the

availability of iron, could have stimulated oceanic primary production. This in turn would have contributed to lower atmospheric CO_2 concentrations during glacial periods compared to today. But also biogenic $CaCO_3$ production impacts marine carbon cycling and atmospheric CO_2. In publication II and III, laboratory experiments with *Emiliania huxleyi* are reported under varying degrees of iron and zinc limitation. It is shown that under iron limitation growth and calcification are equally reduced, whereas zinc limitations leads to an un-coupling of these two cellular processes, resulting in highly calcified cells. Furthermore, the ratio of $CaCO_3$ to particulate organic nitrogen (PON) decreased with increasing zinc concentrations. As there are indications that coccolithophorid growth in parts of the present ocean is zinc limited, enhanced input of zinc in glacial times could have altered global $CaCO_3$ production. Variations in atmospheric zinc deposition on glacial/interglacial time scales may therefore need to be considered regarding CO_2 partitioning between atmosphere and ocean.

Phytoplankton is known to invest considerable amounts of energy for dissolved inorganic carbon (DIC) acquisition, required to achieve maximum rates of photosynthesis and growth. In publication IV, the operation of the so-called carbon concentrating mechanism (CCM) is investigated in *Emiliania huxleyi* under varying degrees of iron limitation. It is shown that under iron deplete conditions rates of DIC uptake are significantly reduced. The leakage (the ratio of diffusive CO_2 efflux to DIC uptake), however, increases with the degree of iron limitation, indicating reduced CCM efficiency. Changes in leakage are thought to be reflected in changes in the carbon isotope fractionation (ϵ_p) of phytoplankton. However, measured values of ϵ_p remained rather constant, independent of the availability of iron. This seeming contradiction is resolved by employing a two compartment cell model, comprising the cytosol and the chloroplast. It predicts that the rate of DIC uptake into the chloroplast is significantly reduced in comparison to DIC uptake into the cytosol under iron limiting compared to iron replete conditions. Moreover, the internal DIC fluxes through the chloroplast membrane is generally an order of magnitude larger than those through the plasmalemma. Thus, assessment of this internal DIC cycling is required to understand carbon

isotope fractionation patterns in marine phytoplankton.

Approaches to investigate inorganic carbon fluxes in marine phytoplankton are based on disequilibrium techniques which rely on exact knowledge of the rate constants for the CO_2 to HCO_3^- inter-conversion rate constants, k_+ and k_-. In publication V, a new method for k_+ and k_- determination in pH bufferd seawater is presented by means of membrane inlet mass spectrometry (MIMS). It is shown that measured and calculated values are in good agreement for a temperature range between 10 and 25° C and pH values between 7.0 to 8.5. This indicates that the two buffers tested (HEPES and BICINE) were able to keep the pH constant on time scales of seconds, as required by this new approach. It is concluded that the experimental procedure applied previously tends to significantly underestimate k_+ and k_-.

Pelagic $CaCO_3$ production by marine organisms is of great importance for CO_2 partitioning between atmosphere and ocean. This doctoral thesis proposes that coccolithophores such as *Emiliania huxleyi* may be relevant for the marine carbon cycle on glacial/interglacial time scales. Marine $CaCO_3$ production could thereby be part of a feedback mechanism system involved in climate change of the last million years which is triggered by variations in Earth's orbit around the sun.

5 Zusammenfassung

Gegenstand dieser Arbeit sind Prozesse, welche für den marinen Kohlenstoffkreislauf von Relevanz sind. Unter diesen liegt das Hauptaugenmerk auf der Aufnahme von anorganischem Kohlenstoff, sowohl zur Photosynthese als auch zur Kalzifizierung, in der Coccolithophoride *Emiliania huxleyi*. Um die Messungen von anorganischen Kohlenstoffflüssen auf zellulärer Ebene zu verbessern, wurden Experimente zur Kinetik des Karbonatsystems im Meerwasser durchgeführt. Desweiteren wurde die Abhängigkeit der Kalzifizierung von der Verfügbarkeit von Spurenmetallen in *Emiliania huxleyi* untersucht. Die vorliegenden Ergebnisse deuten darauf hin, daß Änderungen in der $\mathrm{CaCO_3}$ Produktion von Coccolithophoriden zu den beobachteten Änderungen in der $\mathrm{CO_2}$ Verteilung zwischen dem System Atmosphäre/Ozean während der Glazial- Interglazialzyklen beigetragen haben könnte. Zusätzlich wird ein möglicher Auslösemechanismus für das Ende glazialer Klimaperioden vorgestellt.

In den letzten Millionen Jahren wechselten regelmäßig warme interglaziale mit kalten glazialen Klimaperioden. Mit diesen Änderungen eng verknüpft sind Variationen in der $\mathrm{CO_2}$ Verteilung im System Atmosphäre/Ozean. Von diesen wird angenommen, daß sie durch Änderungen der solaren Einstrahlung in hohen Breiten, welche auf Änderungen der Erdorbitalparameter zurückzuführen sind, hervorgerufen werden. In Publikation I wird ein möglicher Auslösemechanismus für das Ende glazialer Klimaperioden vorgestellt, der sogenannte 'Insolations Kanon'. Dieser ist durch den zeitgleichen Anstieg der solaren Einstrahlung in beiden Hemisphären bei 65° Breite im Hochsommer charakterisiert, wobei der Anstieg im Süden dem im Norden vorausgeht. Was den Zeitpunkt und den Ausgangspunkt des Endes glazialer Klimaperioden betrifft, so ist dieser Auslösemechanismus in perfekter Übereinstimmung mit Erkenntnissen aus Beobachtungen und Modellen. Desweiteren ist er in der Lage, auf die zahlreichen Probleme, welche die Orbitaltheorie der Klimaveränderung aufwirft, Antworten zu geben. Außerdem legt der 'Insolations Kanon' durch seine zwei Randbedingungen für Energie und Zeit die Beteiligung von Rückkopplungsmechanismen

im Klimasystem nahe, welche zum Ende glazialer Perioden schon identifiziert wurden, wie das Schmelzen von Eismassen im Ozean und solchen auf dem Land sowie deren Einfluß auf die globale Zirkulation von Meeresströmungen.

Auch die marine Biosphäre wurde schon als ein möglicher Rückkopplungsmechanismus im Klimasystem der Erde erkannt. So wurde die Vermutung aufgestellt, daß der verstärkte Eintrag von Staub und damit Spurenmetallen in Ozeanregionen, in welchen das Wachstum von Phytoplankton in heutiger Zeit durch die Verfügbarkeit von Eisen eingeschränkt ist, in glazialen Klimaperioden die Primärproduktion stimuliert haben könnte. Das könnte im Gegenzug zu der vergleichsweise niedrigen CO_2 Konzentration in der Atmosphäre während glazialer Klimaperioden beigetragen haben. Auch die Kalzifizierung ist ein Teil des marinen Kohlenstoffkreislaufes und wirkt sich somit auf atmosphärische CO_2 Konzentrationen aus. Die Publikationen II und III präsentieren Ergebnisse aus Laborexperimenten mit *Emiliania huxleyi*, in welchen der Einfluß von Eisen und Zink auf die Kalzifizierung untersucht wurde. So wird gezeigt, daß Eisenlimitation zu einer gleichmäßigen Reduktion von Wachstum und Kalzifizierung führt. Zinklimitation hingegen bewirkt eine Entkopplung dieser beiden zellulären Prozesse, was zu extrem stark kalzifizierten Zellen führt. Desweiteren wird gezeigt, daß mit steigender Zinklimitation das Verhältnis von $CaCO_3$ zu partikulärem organischen Stickstoff zunimmt. Da es Anzeichen gibt, daß das Wachstum von Coccolithophoriden in Teilen des heutigen Ozeans durch die Verfügbarkeit von Zink limitiert ist, könnte also ein verstärkter Eintrag von Zink in glazialen Klimaperioden zu Veränderungen in der globalen $CaCO_3$ Produktion geführt haben. Somit müssen möglicherweise auch Änderungen im Eintrag von Zink, wie sie für glaziales und interglaziales Klima charakteristisch sind, bei der Erklärung für die Verteilung von CO_2 im Atmosphäre/Ozean System berücksichtigt werden.

Phytoplankton ist dafür bekannt, einen beträchtlichen Teil der ihnen zur Verfügung stehenden Energie in die Aufnahme von gelöstem anorganischen Kohlenstoff zu investieren, was maximale Photosynthese- und Wachstumsraten gewährleistet. In Publikation IV werden Laborexperimente mit *Emiliania huxleyi* präsentiert, in welchen der Einfluß der Eisen-

verfügbarkeit auf die Aktivität des sogenannten Kohlenstoffkonzentrierungsmechanismus untersucht wurde. Es wird gezeigt, daß die Aufnahme von gelöstem anorganischen Kohlenstoff unter Eisenlimitation stark zurückgeht. Außerdem steigt das Verhältnis von CO_2 Efflux aus der Zelle zur Gesamtkohlenstoffaufnahme (Leakage) an. Dies ist ein Indikator für verminderte zelluläre Effizienz. Bisher wurde angenommen, daß Änderungen in der Leakage sich in Änderungen der stabilen Kohlenstoffisotopenfraktionierung (ϵ_p) niederschlagen. Mit massenspektrometrischen Methoden gemessene Werte für ϵ_p waren jedoch nicht von der Verfügbarkeit von Eisen und damit der Leakage beeinflußt. Diese sich widersprechenden Ergebnisse werden in Publikation IV gelöst, indem ein Zellmodell konstruiert wird, welches aus zwei Kompartimenten besteht (Cytosol plus Chloroplast). Die Ergebnisse dieses Modelles zeigen, daß unter Eisenlimitation die Aufnahme von gelöstem anorganischen Kohlenstoff in die Chloroplasten erheblich reduziert ist im Vergleich zur Aufahme ins Cytosol, im Gegensatz zu Zellen, die nicht unter Eisenlimitation wuchsen. Darüber hinaus bedeutet dies, daß der Fluß von gelöstem anorganischen Kohlenstoff über die interne Chloroplastenmembran normalerweise um eine Größenordnung stärker ist als der über die Plasmalemmamembran. Abschätzungen interner Kohlenstoffflüsse sind somit nötig, um stabile Kohlenstoffisotopenfraktionierung in marinem Phytoplankton zu verstehen.

Versuchsansätze, in denen anorganische Kohlenstoffflüsse in marinem Phytoplankton untersucht werden können, basieren auf sogenannten Disequilibrium-Techniken. Eine Voraussetzung für diese ist die exakte Kenntnis der Ratenkonstanten für die CO_2 zu HCO_3^- Inter-Konversion (k_+ und k_-). In Publikation V wird eine neue experimentelle Methode in pH gepuffertem Seewasser, unter zu Hilfenahme der Membran-Inlet-Massenspektrometrie, vorgestellt, mit der k_+ und k_- exakt bestimmt werden können. Es wird gezeigt, daß gemessene und errechnete Werte über einen Temperaturgradienten von 10° bis 25° C und pH Werten von 7.0 bis 8.5 in guter Übereinstimmung sind. Dies bedeutet, daß die zwei getesteten pH Puffer (HEPES und BICINE) in der Lage sind, den pH auf Zeitskalen von Sekunden konstant zu halten. Ein Vergleich mit der bisher angewandten experimentellen Methode zeigt, daß diese dazu tendiert, k_+ und k_- beträchtlich zu unterschätzen.

Das von marinen Organismen im offenen Ozean produzierte $CaCO_3$ ist von großer Bedeutung für die Verteilung von CO_2 im Atmosphäre/Ozean System. Die Ergebnisse dieser Doktorarbeit legen nahe, daß Coccolithophoriden wie *Emiliania huxleyi* für den marinen Kohlenstoffkreislauf auf der Zeitskala von glazialen und interglazialen Klimaperioden von Bedeutung sind. Die Produktion von $CaCO_3$ könnte somit Teil eines Systems von Rückkopplungsmechanismen im Klimasystem sein, welches durch Variationen des Erdorbits um die Sonne gesteuert wird.

6 Danksagung

Mein Dank gilt insbesondere Ulf Riebesell, der mir diese Arbeit ermöglichte. Danke für Deine stets offene Tür, die anregenden Diskussionen und für Dein in mich gesetztes Vertrauen. Recht herzlich bedanke ich mich bei Dieter Wolf-Gladrow für die Begutachtung dieser Arbeit.

Ganz herzlich bedanke ich mich bei allen aus der Bremerhavener Kohlenstoffgruppe, die mir die Augen für die diversen Aspekte des Kohlenstoffkreislaufes geöffnet haben. In diesem Zusammenhang gilt mein besonderer Dank Richard Zeebe und seiner Fähigkeit sich begeistern zu lassen. Björn Rost danke ich für die Einführung in die Welt der CCMs und die daraus resultierenden Diskussionen. Anja Terbrüggen und Klaus-Uwe Richter danke ich für ihre tatkräftige Unterstützung bei Messungen und der Bewältigung technischer Probleme. Bei Klaas Timmermans, Loes Gerringa und Marcel Veldhuis vom NIOZ bedanke ich mich für die freundliche Aufnahme und Unterstützung auf Texel.

Für die zahlreichen Diskussionen während der Mittagspausen im Kieler Landtag gilt mein Dank Hermann Bange, Arne Körtzinger, Toste Tanuha und Birgitt Quack. Auch bedanke ich mich bei Christian, Joana, Lisa, Marius, Momo und Scarlett – für Eure verständnisvolle Freundschaft. Schließlich danke ich meinem Bruder und meinen Eltern, für Alles.